A Thesis Submitted for the Degree of PhD at the University of Warwick

Permanent WRAP URL:

http://wrap.warwick.ac.uk/90834

Copyright and reuse:

This thesis is made available online and is protected by original copyright.

Please scroll down to view the document itself.

Please refer to the repository record for this item for information to help you to cite it.

Our policy information is available from the repository home page.

For more information, please contact the WRAP Team at: wrap@warwick.ac.uk
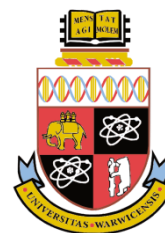
Development of a continuous process for direct amide synthesis over titania based magnetic catalysts under RF heating

by

Yawen Liu

Submitted towards the degree of

DOCTOR OF PHILOSOPHY

March, 2017

School of Engineering

University of Warwick

Table of Contents

I

III

List of Tables

List of Figures

VII

VIII

Acknowledgement

Firstly I would like to thank my supervisor professor Evgeny Rebrov for offering me the opportunity to obtain the PhD degree. He guided me professionally during the whole research and shaped me into a good researcher in the chemical engineering field. Many thanks to my co-supervisor Dr Kirill Tchabanenkof from Queen's University Belfast who offered me needed assistance at the initial and final stages of my research. I also want to thank Dr Pengzhao Gao from Hunan University, China for his efficient collaboration work, and also his great patience on answering my questions and doubts. I also like to express my gratitude to Professor Andre van Veen who gave me the professional and valuable tips during my panel meetings.

I am grateful for all the previous and current fellows in Evgeny's group. Thanks to Thomas and Sourav from Queen's University Belfast for offering me valuable experience and guidance on how to be a good researcher in my first year. I also want to thank Javier, Guannan, John and Jonathan for giving me necessary help on my daily work. Many thanks must go to Nikolay Cherkasov, for inspiring me by his intelligence and enthusiasm on academia, giving me invaluable help and suggestions on my project. I would like to thank the financial support from School of Engineering, University of Warwick, and European Research Council.

Finally, I want to take the opportunity to thank my family members. Many thanks go to my father and mother for the unselfish support on my decision of studying abroad. Especially, I would like to give my great gratitude to my husband Xiaohan Liu. He gave me countless encouragement, comfort, and very helpful ideas when difficulties arose on both academic career and personal life.

Declaration

This thesis is submitted to the University of Warwick in support of my application for the degree of Doctor of Philosophy. It has been composed by myself and has not been submitted in any previous application for any degree.

The work presented (including data generated and data analysis) was carried out by the author except in the cases outlined below:

The synthesis of the uncalcined core-shell and core-shell-shell magnetic catalysts carried out by the collaboration work with the Dr Pengzhao Gao' group in University of Hunan, China. The experimental plan and design of these catalysts were discussed and decided by both sides.

Parts of this thesis have been published by the author:

[1] Yawen Liu, Pengzhao Gao, Nikolay Cherkasov, Evgeny V. Rebrov, Direct amide synthesis over core-shell $TiO_2@NiFe_2O_4$ catalysts in a continuous flow radiofrequency-heated reactor, RSC Advances, 2016, 6(103), 100997-101007

[2] Yawen Liu, Nikolay Cherkasov, Valentin Doluda, Evgeny V. Rebrov, Transition from batch to continuous processing in direct amide synthesis over a sulfated titania/nickel ferrite composite catalyst (submitted)

[3] Yawen Liu, Pengzhao Gao, Nikolay Cherkasov, Evgeny V. Rebrov, Synthesis of core-double shell $NiFe_2O_4@SiO_2@TiO_2$ and sulfated core-shell composite magnetic catalyst for radiofrequency heated direct amide synthesis (submitted)

Abstract

In this work, TiO_2 as the catalyst to catalyse the direct amide synthesis was firstly optimized by sulfation. The type and amount of sulfate sources were varied to modify the acid sites on the titania surface, resulting in different catalytic activities. Composite magnetic catalysts (CMCs) having magnetic and catalytic parts with three different structures have been synthesized. In the first method, a series of CMCs containing 33-50 wt.% of sulfated TiO_2 onto $NiFe_2O_4$ were synthesized by ball milling. Mechanochemical synthesis was found to be a facile route to provide a strong contact between magnetic and catalytic nanoparticles. In the second method, $TiO_2/NiFe_2O_4$ core-shell CMCs with a titania loading of 9-32 wt.% were synthesized by sol-gel method. The effects of calcination temperature and titania loading on their catalytic activity and stability were studied. The structure of $TiO_2/NiFe_2O_4$ core-shell CMCs was further improved by synthesizing a middle layer of SiO_2 between the core and TiO_2 shell in the third method. The obtained CMCs were further sulfated by two methods to promote the activity.

The CMCs were characterized by XRD, SEM, TEM, XPS, TGA, VSM, FT-IR of adsorbed pyridine, N_2 adsorption/desorption isotherms and measurement of specific absorption rate. The catalytic activity was measured in the reaction between 4-phenylbutyric acid and aniline in the 140-200 ^{o}C range at a pressure of 6 bar in both batch and continuous modes. The reaction rate over the optimal sulfated TiO_2 was four-fold of that over the initial TiO_2. The effect of reaction temperature on deactivation was studied. For CMCs, the reaction rate over titania in an optimised $NiFe_2O_4@SiO_2@TiO_2$ CMC was 1.5 times higher than that over titania in ball milled CMC. The catalytic activity of this CMC could be totally recovered by a regeneration protocol in the RF-heated flow reactor at mild conditions. However, the catalyst deactivation kinetics was substantially reduced after each cycle. Finally, a near-isothermal RF-heated continuous reactor was designed to scale-up the amide synthesis to a larger production scale. The throughput of 4, N-diphenylbutyramide was 0.27 g/h, which was five-fold of that shown in the literature [1].

Abbreviations

RF - radiofrequency

CMC - composite magnetic catalyst

XRD - X-ray diffraction

SEM - scanning electron microscopy

EDS - energy dispersive X-ray spectroscopy

VSM - vibrating sample magnetometer

TEM - transmission electron microscope

TPO - temperature programmed oxidation

XPS - X-ray photoelectron spectroscopy

SAR - specific absorption rate

TG-DTA - thermogravimetric and differential thermal analysis

FT-IR - fourier transform infrared spectrometer

RF-CR - radiofrequency heated continuous reactor

CH-CR – conventionally heated continuous reactor

WHSV – weight hourly space velocity

FO – fibre optics

PID – proportional-integral-derivative (controller)

P – heat produced due to the hysteresis loss

μ_0 – vacuum permeability

f – frequency of the magnetic field

H – Intensity of the magnetic field

M – magnetisation

C_p – heat capacity

m – mass of the component

T – temperature

t – time

r – reaction rate

k – rate constant

C_A – concentration of reactant A

C_p – concentration of the product

D_c – crystalline size

λ – wavelength

β – broadening at half the maximum intensity

θ – bragg angle

E_a – activation energy

R – idea gas constant

S_i – surface area of the component i

L_i – Length of the structural zone (s) or catalytic bed (c)

$r_{1,2}$ – inner (1) or outer (2) radius

d_i – thickness of the insulation

ε_p – porosity

κ – permeability

U – overall heat transfer coefficient

v – superficial velocity

ρ_i – density of the component i

λ_i – thermal conductivity of the component i

μ_f – dynamic viscosity

β_F – Forchheimer drag option

I – stress invariant

h – convection heat transfer coefficient

Q_h – volumetric heating rate

F – volumetric flow rate

τ – residence time

Chapter 1

Introduction

1.1 Background and motivation

Amide synthesis is regarded as one of the most fundamental but important chemical transformation in pharmaceutical, medical, biological as well as polymer industries [2]. In the pharmaceutical industry, one quarter of the drugs in the production line and nearly 67 wt.% of drug candidates contain amide bond [3]. However, the current production route in the industry always consumes large amount of coupling agents to activate the reactants [4], resulting in low atom-economy. Thus a suitable route to accelerate the amidation from acids and amines directly is necessary to be explored. To realize the continuous production of amides, reactor is also a main concern for the chemical engineers. Even though batch reactor is widely used in the industry, continuous reactor is more favoured in the academia, for its less processing time and more efficient heat and mass transfer [5]. As amide synthesis undergoes at relative high temperature, for reacting temperature above ambient temperature in the industry, the heating of the units is normally realized by heat conduction through the heating jacket where steam or hot air continuously passes by. The heat is transferred through the wall of the unit and the whole substrates inside can be heated. Nevertheless, there exist several shortages of this method. Firstly, as heat transferred from the wall, the large temperature gradient on the cross section will occur if stirring is not sufficient. This will lead to the bulk temperature lower than designed. Secondly, the heat loss to the surrounding is significant, resulting in high carbon footprint of the production line. With this in mind, a novel, efficient and applicable to large scale production heating method should be explored and studied. RF heating, which generates the heat by applying alternating

magnetic field at high frequency to magnetic material, is a good option to replace the conventional heating. As the flow stream is heated from inside, it has less heat loss during the heat transfer and can provide a much smaller temperature gradient on the cross section [6].

With these concerns, the aim of this project was to develop an RF-heated continuous reactor for direct amide synthesis over a supported heterogeneous magnetic catalyst. The first goal was to optimize a titania-based heterogeneous catalyst. After a good catalytic performance was achieved, the synthesis routes to composite magnetic catalysts (CMCs) were studied and compared. The catalyst composition, morphology, and magnetic properties for selected CMCs were analysed. The catalytic activity and stability of magnetic catalysts having different structures were obtained in an RF-heated flow reactor. Also, relevant studies on deactivation mechanism and regeneration methods were explored. In order to facilitate the scale up, the catalytic bed was structured in specific geometrical arrangements inside the reactor and various operation methods were studied to achieve the near-isothermal continuous reactor.

1.2   Direct amide synthesis from acid and amine

Acids and amines are the most common reactants chosen to form the amide bond. The most traditional way to form the amide bond is using activated carboxylic acid derivatives as the partner of the amine [7]. Different kinds of coupling agents such as carbondiimides, 1*H*-benzotriazole and acid halides [4] were exploited to transform the hydroxyl in carboxylic group of an acid into a better leaving group, in order for them to react with the amine. Although a certain progress has been achieved within this method, a series of environmental concerns were raised as well due to its low atom economy. In 2005, the research area of amide bond formation avoiding poor economy reagents was voted as the first industrial concern in ACS GCI Pharmaceutical Roundtable, which encouraged researchers to explore more novel and green methods [3]. Under this situation, direct amide synthesis from non-activated carboxylic acids and amine has been widely explored.

1.2.1 Reaction mechanism study

The mechanism study of the amide reaction is the key to understand the reaction kinetics, the way of accelerating the reaction and possible formation of by-products. As early as 1989, the kinetics and mechanisms of iprodione formation from hydantoic acid in an acidic media were explored [8]. This was further elaborated by Dr Andrew Whiting and his group in Durham University [9-11], who studied the mechanism details of direct amide synthesis and confirmed by both experiments and quantum mechanics simulation.

Two routes for reaction of a carboxylic acid and an amine, which form the ammonium carboxylate salts and amide, respectively, were proposed. The salt, which has low solubility in the non-polar solution, is formed as the precipitate and therefore the yield varies with the reactants (Table 1.1). As for the amide synthesis, it contains several intermediates proceeding the final step. Firstly, the carbonyl groups between molecules of acids are inter-bonded, producing the dimer of the carboxylic acids. Then a nucleophilic amine attacks the carbon atom in one of the carbonyl groups of the dimer, and the spare proton is donated to another carbonyl group, reforming the initial acid molecule. After the break of the unstable intermediates, an amide is formed with the by-product of water (Figure 1.1).
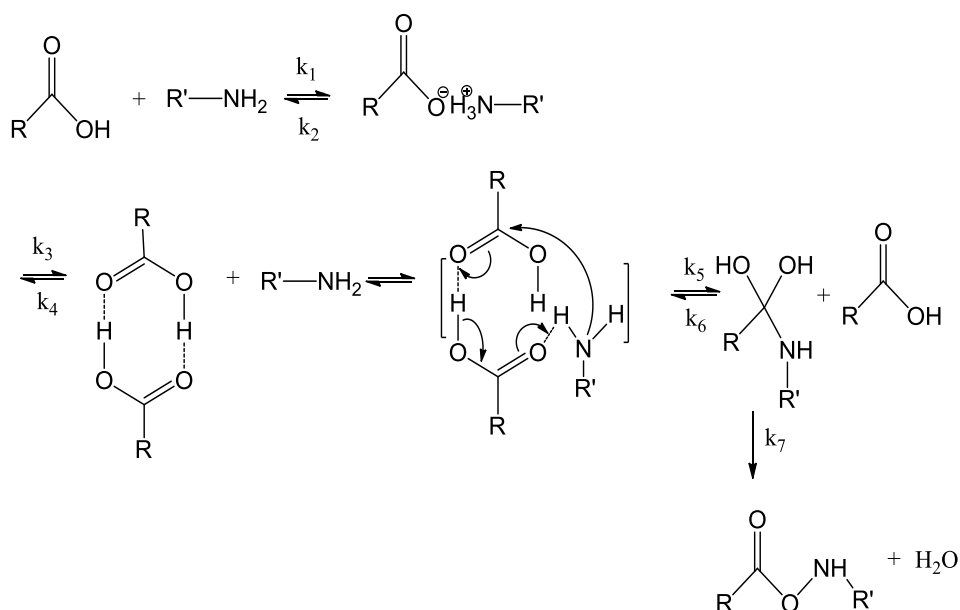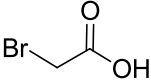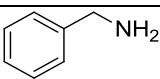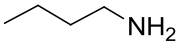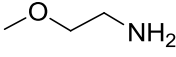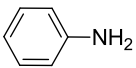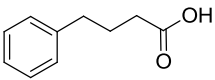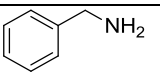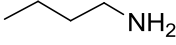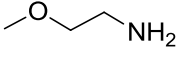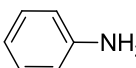
Figure 1.1 Mechanism of the amide formation between carboxylic acids and amines [11]

3
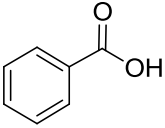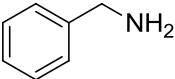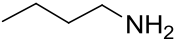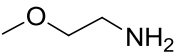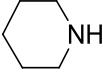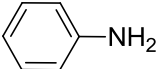
According to the mechanism, the pK_a value of the carboxylic acid, and basicity of the amine have a major influence on reaction rate and selectivity for the amide formation. In general, the carboxylic acid with lower pK_a and more basic amines are more reactive while they are also likely to form more stable ammonium carboxylate salts, which could significantly affect the rate of amide formation [9, 11].

1.2.2 Stoichiometric reactions of acids and amines to form amides

Depending on the reactivity of the reactants, the activation energy is different, leading to the fact that some reactants can react without a catalyst while the others need catalysts for activation. Normally the electron-withdrawing functional group beside the carbonyl make the acid molecule more reactive while for the amine it has the opposite effect. The interactions become weaker with the increase of distance between functional groups. The stoichiometric amide yields of some groups of reactants are listed in Table 1.1.

Table 1.1 Salt precipitate and amide yields of the reactions between carboxylic acids and amines [11]

Carboxylic acid	Amine	Salt precipitate yield [a] (%)	Uncatalysed amide yield [b] (%)
		50	0
		48	0
		0	0
		13	0
		46	0
		0	64
		100	<1
		0	54
		0	24
		0	4

4

Carboxylic acid	Amine	Salt precipitate yield [a] (%)	Uncatalysed amide yield [b] (%)
	benzylamine (—NH$_2$)	64	14
	butylamine (—NH$_2$)	100	0
benzoic acid	2-methoxyethylamine (O—NH$_2$)	72	5
	piperidine (NH)	0	10
	aniline (—NH$_2$)	0	0

a Reactants were mixed at ambient temperature and products were analysed by NMR and CHN;
b In toluene at 120 °C with Dean–Stark water removal over 48 h

The stoichiometric synthesis of amides is quite limited by the type of the reactants. Usually, high temperature, removal of water and long reaction time up to 24 h are needed in the process [11-13]. The energy delivery method in the synthesis could be promoted by replacing the conventional heating by inductive heating or microwave heating. Perreux et al. [14] reported the amides were successfully synthesized from certain types of amines like benzylamine, aniline and carboxylic acids at 150 °C in 30 min by microwave heating. The reaction under RF heating was also studied. The reaction time by using RF heating was reduced to less than 20 min for several amides with the product yield achieving 90% [15].

1.2.3 Development of heterogeneous catalysts for direct amide synthesis

In consideration of limitations of conventional stoichiometric amide synthesis, catalytic synthesis became the major priority to the researchers. Initially, homogeneous catalysts were studied. The good distribution in the solvent, efficient mass transfer to the active sites and various design of the structure make homogeneous catalysts highly active and selective. Metal salts like ZrCl$_4$ [16], TiCl$_4$ [17] and boron based catalysts [18] were widely tested to catalyse the direct amide synthesis. Even though the reaction rate was increased in the presence of a homogeneous catalyst, the separation and recycling of the catalysts hindered further process development due to large

energy input required in the subsequent distillation step. Also, because most homogeneous catalysts are temperature-sensitive, the high temperature needed for distillation may decompose the catalysts, leading to the low atom-economy and high cost. Other separation methods like extraction or filtration result in an inevitable catalysts loss as well [19]. With the impact on green chemistry, heterogeneous catalysts which are easy to separate and reuse have been widely explored in the recent years.

Metal oxides and weak solid acids are conventional heterogeneous catalysts for direct amide synthesis. Sometimes, metal oxides are also regarded as solid acids due to the existence of weak acid sites on their surface. The acid sites accepting the long pair of electrons is named as Lewis acid sites and another type of acid sites which donate the proton is called Brønsted acid sites. Among metal oxides, CeO_2, CaO, MgO, ZnO, Y_2O_3, TiO_2, ZrO_2, Nb_2O_5, Al_2O_3, SiO_2, sulfated tungstate were shown to have catalytic activity in amide formation [20-22]. Solids acids like Amberlyst-15, HBEA, Niobic acid, Mont-K10, Nafion-SiO_2 [20], IBA [23] were also applied. The catalytic activity depends on the reactants used. In particular, the performance of heterogeneous catalysts and respective reaction conditions are listed in Table 1.2 for the synthesis of 4,N-diphenylbutyramide, N-phenylpropionamide and N-phenylacetamide.

Table 1.2 Amide yields of 4,N-diphenylbutyramide, N-phenylpropionamide and N-phenylacetamide over different heterogeneous catalysts

Amide product	Catalyst	Reaction condition	Amide yield (%)	Ref.
4,N-diphenylbutyramide	EPZG[b]	a	27	[24]
	EPZ10[b]	a	19	[24]
	FeCl₃/K60 silica	a	50	[24]
	ZnCl₂/K60 silica	a	41	[24]
	K60 silica	a	55	[24]
	Zeolite B25	a	19	[24]
	Zeolite B150	a	33	[24]
	IBA	c	46	[23]

Amide product	Catalyst	Reaction condition	Amide yield (%)	Ref.
N-phenylpropionamide	γ-Al_2O_3	d	24	[21]
	TiO_2_Merck	d	4	[21]
	TiO_2_P25	d	47	[21]
	CeO_2	d	27	[21]
	ZrO_2	d	9	[21]
N-phenylacetamide	Nb_2O_5	e	80	[25]

a 10 wt.% of the catalyst, 12 mmol/L toluene solution of 4-phenylbutyric acid and aniline, 100 °C, 24 h.

b These catalysts referred to the "enviro" catalysts provided by Contract Catalysis (Knowsley) Ltd.

c 1 mol% catalyst, 100 mmol/L toluene solution of 4-phenylbutyric acid and aniline, 85 °C, 22 h.

d C_{cat} = 18 g/L, 550 mmol/L toluene solution of propanoic acid and aniline, 110 °C, 24 h.

e 50 mg catalyst, 500 mmol/L toluene solution of acetic acid and aniline, azeotropic reflux for 30 h.

1.3 TiO_2 based catalysts for direct amide synthesis

1.3.1 Reaction mechanism

The development of TiO_2-based catalysts for organic reactions is often considered as a promising way to move forward. These catalysts have high activity, good selectivity and facile methods for separation from the reaction mixture [26]. On the surface of TiO_2, the titanium atoms are surrounded by the fewer oxygen atoms compared to the bulk titanium atoms, making an imbalanced electronic state on the surface [27]. The titanium atoms on the surface exist in the form of Ti^{4+}, which act as Lewis acid sites. The Ti^{4+} cations can also induce the polarization of H_2O molecules adsorbed from the media and form Brønsted acid sites on the surface. For pure TiO_2 mainly Lewis acid sites are observed while strong Brønsted acid sites appeared after sulfation [28]. In the amide synthesis reaction, because of the existence of Ti^{4+} sites on the surface, the carboxylate oxygen atoms interact with the surface of the catalysts, leading to the decrease of the electron density on the carbon atom. As the carbon becomes more electrophilic, it becomes much easier to be attacked by the nitrogen atom of the amine which is quite

nucleophilic (Figure 1.2), forming the amide bond. It can be concluded from the mechanism that Lewis acid sites play the main role in the catalysis of amidation while Brønsted acid sites do not contribute in the same extent.
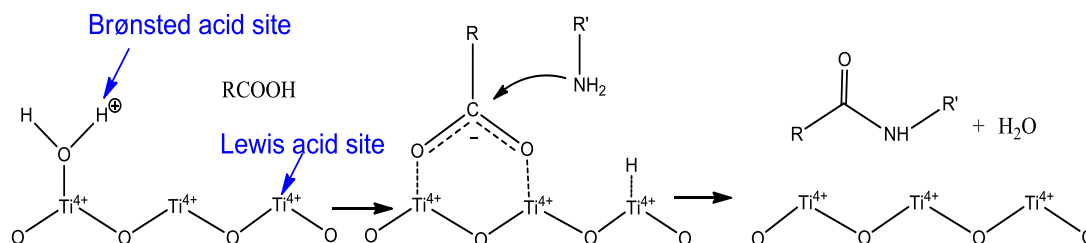
Figure 1.2 Scheme of mechanism of direct amide synthesis from carboxylic acids and amines over titania catalysts [29]

To enhance the catalytic activity, the acidity of the active sites should be further promoted. The functionalization of TiO_2 catalysts with SO_4^{2-} groups was found to be an effective option. The sulfation of TiO_2 is widely explored to reach a better performance in organic transformations, such as esterification of the fatty acids [30], N-formylation [31, 32] or dye degradation [33]. The distribution of electron density in sulfated TiO_2 catalyst improving catalytic activity is shown in Figure 1.3. The double bond between the sulfur and oxygen atoms in the sulfate group bonding to the surface further reduces the electron density on the titanium atoms, making the Lewis acid sites stronger. Thus the carbon in the carboxylate of an acid becomes more reactive electrophile, resulting in an easier bonding with the amide. Acidity of Brønsted acid sites was also increased after the sulfation. This mechanism was also supported by Wang et al. [34].
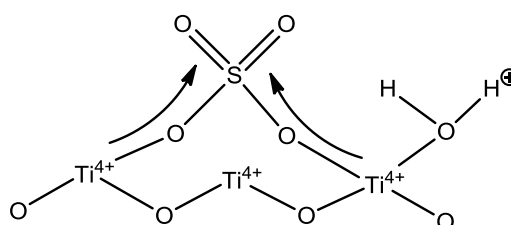
Figure 1.3 Mechanism of sulfate effect on titania [35]. The arrows indicate the inducing of the electrons

1.3.2 Synthesis of sulfated TiO$_2$

Sol-gel method

Sol-gel method is widely adopted to produce the sulfated titania catalysts. The method can be classified into two routes. In the first route, different titanium alkoxides like titanium isopropoxide [36, 37], titanium isobutoxide [38] , or tetraisopropyl orthotitanate [33] were used as the precursors to form the solid TiO$_2$ particles. Then these solid particles were dispersed in a sulfuric acid solution. After drying and calcination, the sulfated TiO$_2$ was obtained [31]. The second route is to use the thermal hydrolysis of commercial titanium oxysulfate to form the sulfated TiO$_2$ [39-41]. Besides the sol-gel method, commercial P25 titania (Evonik) was also treated in a sulfuric acid solution to provide a fast way to synthesize sulfated titania [42].

Sulfate precursors

Except for using an industrial titanyl sulfate solution directly, the type of sulfate precursors has a great impact on catalyst activity. Sulfuric acid and ammonium sulfate were two alternatives which were ever studied as sulfate precursors [43]. It was found out that the catalysts sulfated by ammonia sulfate had a larger distribution of acid strength, similar acid quantities but different acid sites when compared to the catalysts sulfated by sulfuric acid. For type of acid sites, pyridine adsorption studied by FTIR showed that in the catalyst made from ammonium sulfate, both Lewis acid and Brønsted acid sites were detected while for the catalyst made from sulfuric acid, only Lewis acid sites were observed.

Sulfate loading

It has been proven that the amount of added sulfate ions is quite an important factor which affects catalytic performance of titania [43], for it changed the quantity and strength of acid sites. The way of coordination between sulfate and Ti^{4+} changes with sulfate concentration. By using lower amount of sulfate ions, the sulfate complex is in bidentate bridging structure while it becomes bidentate chelate with increasing the sulfate loading on the

surface (Figure 1.4) [28]. At higher concentrations, the structure of sulfate matrix interaction was proven to have a very low thermal stability [37].
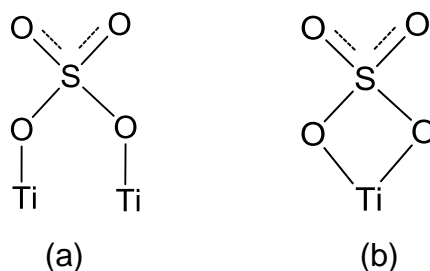
Figure 1.4 Structure of sulfate complex on the surface of TiO_2 (a) bidentate bridging structure (b) bidentate chelate structure [28]

As the concentration of sulfate ions on the surface is increasing, both the strength and quantities of Lewis acid sites and Brønsted acid sites increase [41]. Chesalov et al. studied the TiO_2 with 0.12 and 6.9 wt.% SO_4^{2-} and found that the strong Brønsted acid sites were only observed in the TiO_2 samples with higher sulfate content [28]. In a wider range of TiO_2/H_2SO_4 molar ratio from 5 to 20%, Lewis acid sites form faster than Brønsted acid sites [37]. The concentration of weak Lewis acid sites was also found out to rise more rapidly than the strong ones [44]. Krishnakumar et al. employed various sulfated titania catalysts with the loading of sulfate ions ranging from 1 to 7 wt.% to a series of reactions like synthesis of quinoxaline and dipyrido-phenazine derivatives [42], formation of chalcones [45], degradation of Reactive Orange 4 [33] and N-formylation of amines [32]. They came to the same conclusion that a 5 wt.% sulfated titania catalyst resulted in the highest product yield after the same reaction time. For the formation of surface complexes of β-picoline, pyridine-3-carbaldehyde and nicotinic acid, a 6.9 wt.% sulfated titania catalyst was found out to be superior to a 0.2 wt.% one [41]. In transesterification reaction of vegetable oils, a 5 wt.% sulfated titania catalyst showed the best activity as compared to either 10 or 20 wt.% samples [37]. Based on literature available, it can be concluded that the catalyst performs better with an increase of the sulfate loading until around 6 wt.% and then the activity drops if more sulfate ions are added.

1.3.3 Organic reactions catalysed by sulfated TiO$_2$

Sulfated TiO$_2$ has good catalytic performance on various types of organic reactions. In direct amide synthesis, besides the reaction mentioned in section 1.2.3, it could also catalyse the reactions between various amines and stearic acid, and various carboxylic acids and aniline, resulting in most isolated yields over 90% at 115 °C in 3 h according to Mona Hosseini-Sarvari's research [38]. For most aromatic acids and amines, the amide yield gets to over 70% when catalysed by TiO$_2$ or sulfated TiO$_2$ at around 110 °C for 30 min [26, 32, 46]. Mona and colleagues also applied sulfated TiO$_2$ to other reactions and got the positive results as well. N-formylation reaction was one type of reaction which had substantial reaction rate under the catalysis of sulfated TiO$_2$. N-formylation of simple amines could achieve over 90% under solvent free conditions at room temperature in 1 h, and for more complex amines at least 60% was converted in around 3 h [31]. Synthesis of pyrroles from different amines and 2,5-dimethoxytetrahydrofuran was also catalysed by a sulfated TiO$_2$ catalyst and the yield of various products exceeded 90% in 2 h [47]. Esterification of various fatty or aromatic acids with various alcohols and phenols as well as reactions between different diols and polyol with stearic acid were also found out could be catalysed by sulfated titania with the product yield exceeding 90% in 2 h at 80 °C [30]. Similarly, esterification of fatty acids with alcohols catalysed by sulfated TiO$_2$ was found out to be effective by the work presented in other papers [43, 48, 49] . Krishnakumar et al. [50] reported high catalytic activity of sulfated P25 TiO$_2$ in the synthesis of quinoxaline and dipyridophenazine derivatives. A series of derivatives were synthesized successfully at room temperature with a product yield over 60% in 2 h. They also use it to catalyse the synthesis of chalcones from acetophenone and different benzaldehydes under microwave irradiation. The conversions for all the reactions were rather high, which could be over 60% in 180 s [45]. Ahmed et al. applied sulfated TiO$_2$ to the dehydration of sorbitol to isosorbide and the yield could reach to near 75% in 4 h [36]. De Almeida et al. [51] studied its catalytic activity on the transesterification of vegetable oils and the best yield was 40% at 120 °C for 1 hr. A sulfated TiO$_2$ catalyst also showed the best catalytic property in the

synthesis of dicoumarol by condensation from 4-hydroxycoumarin and various aldehydes compared to other heterogeneous catalysts. The yield of different products over 80% were reached over a 10 wt.% loading sulfated TiO_2 catalyst in less than 20 min at 80 °C [52].

1.4   Magnetic nanoparticles for RF heating

1.4.1   Physical properties related to RF heating

Since the magnetism of the material has a large utility in different areas like medicine and physics, properties of the magnetic nanoparticles and the key factors affecting their magnetism have been widely explored. To apply magnetic particles to induction heating in chemistry, their properties should be optimized, namely saturation magnetisation, coercivity, Curie temperature, thermal stability and corrosion resistance. Some of these properties will be discussed in this section. The heating rates of a material under RF field can be estimated from its magnetization M-H curves. The magnetization curves of ferromagnetic and paramagnetic material are quite different. For the ferromagnetic particles, when an external magnetic field is applied, the magnetism of the particles will rise until getting to the saturation magnetisation (M_s). However, with the fading of the external field, part of the magnetism will retain in the particles (M_r) and another magnetic field on the opposite direction called coercivity (H_c) is needed to pull the magnetism back to zero. The M-H curves describing the relationship between magnetism of the material and external field strength is also called hysteresis loop (Figure 1.5 (a)). However, for paramagnetic material, the magnetism is induced by the external magnetic field, having no hysteresis phenomenon (Figure 1.5 (b)). For soft magnetic material which has a low coercivity field around several hundred A/m, the heat generated was found out to be proportional to the area of hysteresis loop [53, 54]. The ferromagnetic material obviously shows much better heating property than paramagnetic material.

(a)   (b)
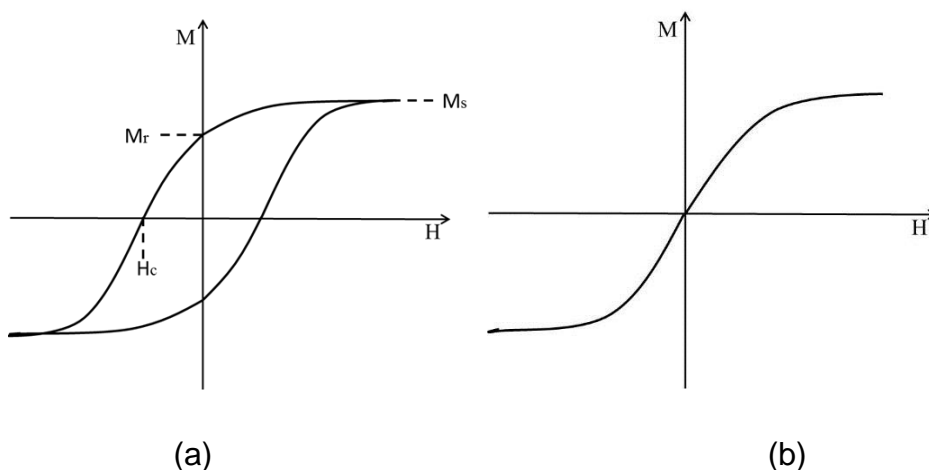
Figure 1.5 Schematic view of magnetization curves of (a) ferromagnetic material (b) paramagnetic material

The Curie temperature is the point where particles transit from ferromagnetism to paramagnetism. Magnetic particles loss the heating ability under RF heating once Curie temperature is reached [55]. In this way, the existence of Curie point limits the highest possible temperature the reactions can be performed under RF heating. Another aspect needed to be considered is the corrosion resistance of the magnetic material. Since the magnetic material is immerged in the reactant mixture, its composition or crystal type may change during the reaction process when oxygen, high temperature, strong acid or basic reactants are used, leading to the loss of the heating property. Thus necessary stability of the material in the chemical environment is required. The physical characteristics mentioned above vary with the composition of the magnetic particles.

1.4.2 Type of the magnetic material

The components of magnetic nanoparticles are mainly metal, metal oxide or alloy of the iron-group elements.

Metals and their alloys

Pure Fe, Co and Ni and their alloys demonstrate ferromagnetism. For the pure metals, their Curie temperatures rose with the increasing size of the particles in the nanometre range. The values of the Curie temperature for Fe, Co, Ni at 3 nm are 680, 1040 and 320 $^{\circ}C$, respectively [56]. Without a

13

protective coating, they are very easy to get oxidized in air or by oxidants [57], resulting in the mechanical and magnetic change. Iron powder was found out could be heated to a certain extent in an RF field below 25 kHz, which was attributed to the instability of the iron itself [58]. Co and Ni nanoparticles showed better resistance and under the same AC magnetic field, the Ni particles showed higher specific absorption rate (SAR) than that of Co particles [59].

Iron oxides

The γ-Fe_2O_3 and Fe_3O_4 are the common magnetic materials to be chosen for induction heating. The Curie temperature of 25 nm Fe_3O_4 nanoparticles is 849 °C [60]. Nevertheless, the mixed iron oxides, Fe_3O_4 can be oxidized into iron (III) oxide, γ-Fe_2O_3 if heated over 150-170 °C [61-63]. On the other side, the ferromagnetic γ-Fe_2O_3 transforms to the paramagnetic α-Fe_2O_3 above 500 °C [64], limiting the maximum allowed temperature in a catalytic process. Compared to pure Fe nanoparticles, the SARs of iron oxides were found to be higher, and the SAR of γ-Fe_2O_3 was higher than that of Fe_3O_4. Also, the strength of magnetism varied with the particle size as the SAR of 25 nm Fe_2O_3 nanoparticles is much higher than that of 9 nm (Figure 1.6) [65].
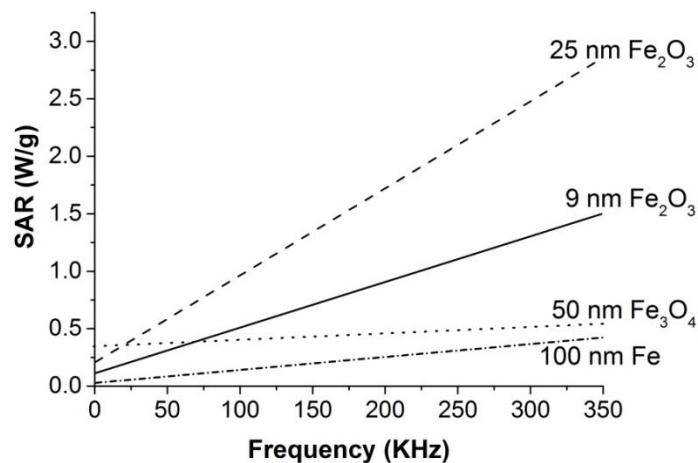
Figure 1.6 The SAR of different magnetic nanoparticles as a function of frequency of magnetic field [65].

Metal ferrites

Ferrites are mixed metal oxides of Mn, Ni, Zn, Cu and Co. They are often obtained to regulate magnetic properties of ferromagnetic materials. Different from simple iron oxides, their Curie temperatures and relative magnetic

14

properties can be easily tuned by the control of their chemical composition, phase structure and crystal size [66-68]. For instance, an addition of Zn to nickel ferrite which forms $Ni_{0.5}Zn_{0.5}Fe_2O_4$ increases the specific surface area while decreases both the Curie temperature and SARs [54, 55]. Even though the properties of metal ferrites are varied, the Curie temperature of common metal ferrites like $MnFe_2O_4$, $NiFe_2O_4$, $CoFe_2O_4$ are located above 550 ⁰C [60, 69, 70]. The SAR of metal ferrite is normally lower than that of Fe_3O_4 [71], but they showed an improved magnetic stability at high temperatures and in high frequency RF field [72]. In particular the magnetism of nickel ferrite has a good thermal stability which can tolerate temperature up to 600 ⁰C [73, 74]. Also, the heating rate shows only a slight decrease even at high frequency [72].

1.5   Synthesis of magnetic catalysts

Even though heterogeneous catalyst is quite easy to separate in most cases, it still faces the recycling problem when very fine microparticles are used in viscous solvents. Also, still large amount of energy is consumed in the separating operation by filtration or centrifugation in industry. Therefore, the magnetic microparticles have attracted much attention as their separation can be easily realized by an external magnet. The separation problem of homogeneous catalysts could also be solved by immobilizing homogeneous catalysts onto a magnetic core. Due to this reason, different methods have been studied to make both homogeneous [75-78] and heterogeneous catalysts [79, 80] attached to magnetic cores. Another novel utility of magnetism is to be used in induction heating, providing a fast and highly efficient heat generation. The efficiency of RF heating could reach 85% which cannot be reached by other heating methods [81]. In the past, the heating properties of composite magnetic nanoparticles have been widely applied to cancer treatment on the aspect of hyperthermia [82, 83] and drug delivery [84, 85]. These areas were developed first, as the costs are typically not the limiting factor there. However, only a few studies were reported describing the application of composite magnetic catalysts in fine chemical synthesis [58, 86, 87].

A magnetic catalyst which has both the RF heating and catalytic function is called composite magnetic catalyst (CMC). Different ways to synthesize the magnetic catalyst result in different structures of CMCs. Also the way of combination between magnetic and catalytic components affects both the magnetic and catalytic properties.

1.5.1 Synthesis of magnetic catalysts with a core-shell structure

The most suitable magnetic catalyst is the one with a core-shell structure. As magnetic nanoparticles are either metal, metal oxide or alloy of the iron-group elements, they are easily corroded by oxygen or chemicals, resulting in the loss of the magnetism. A shell of the catalyst can form a protective layer to avoid the change of magnetic property in the course of reaction. Also, the shell can act as a changeable platform to introduce necessary functional groups, which is extremely important for immobilizing homogeneous catalysts. Directly attaching homogeneous catalysts on the surface of magnetic material is inefficient and type of the homogeneous catalysts which can successfully form the bonding with the surface of magnetic material is limited [78].

For magnetic nanoparticles, aggregation is another problem which sharply decreases specific surface area and reduces unique properties associated with the nano material. The aggregation process can be avoided by core-shell structure since functional groups on the surface of shell material can maintain the catalyst in a highly dispersed state [88]. With the development of the core-shell MNPs, various material like SiO_2 [89, 90], carbon [91, 92], noble metal [93, 94] etc. can be coated onto the MNP cores for different applications.

To synthesize composite magnetic particles with immobilized homogeneous catalysts, wet chemical synthesis is a preferable method. Typically, a layer of silica shell or polymer is coated onto the magnetic nanoparticles first and then a homogeneous catalyst is attached [78]. In this approach, magnetic nanoparticles are synthesized from the corresponding metal salts, and then the as prepared particles are immerged in the solution containing silica

precursors or polymers, forming the coating over the cores. The core-shell nanoparticles are further mixed with a solution containing a homogeneous catalyst, forming the strong bonds between the catalysts and the surface of the shell [75, 95, 96]. Some homogeneous catalysts were reported to directly form the bonding on the surface of magnetic cores. One-pot precipitation synthesis which is the mixing the metal salts and homogeneous catalysts together to precipitate the magnetic catalysts [76] and treating magnetic particles with solution containing homogeneous catalysts [77] was reported.

For heterogeneous catalysts supported on the magnetic nanoparticles, there exist several options to synthesize these composites. Sol-gel synthesis is the most common and conventional method to form the CMC with a core-shell structure, as the operation is facile and the properties like surface area and shell thickness can be easily tuned. In a typical sol-gel process, magnetic nanoparticles are prepared first. In the next step, these nanoparticles are dispersed in a solvent with surfactants or functional additives, and then a catalyst precursor is added. After an aging period, a gel is formed. After certain steps of centrifuging, drying and calcination, the shell covered magnetic particles are obtained. Several materials like silica, metal and metal oxide can be coated by sol-gel method using different precursors. Especially, a reducing agent should be added when synthesizing the metal shell. The types of precursors for common heterogeneous catalysts are listed in Table 1.3.

Table 1.3 Precursors of common heterogeneous catalysts for sol-gel method

Heterogeneous catalysts	Precursors	Ref.
SiO_2	Tetraethyl orthosilicate (TEOS)	[97]
TiO_2	Titanium ethoxide (TEOT)	[98]
	Tetrabutyl titanate (TBOT)	[99-101]
	Titanium isopropoxide (TTIP)	[102, 103]
ZnO	Zinc acetate	[100, 104-106]
SnO_2	$SnCl_4$	[107-109]
	Na_2SnO_3/ K_2SnO_3	[110-112]
Al_2O_3	Aluminium isopropoxide (AIP)	[113, 114]
MnO_2	$KMnO_4$	[115, 116]
	Manganese oleate	[117]
Y_2O_3	$Y(NO_3)_3$/YCl_3	[118, 119]
Au	$HAuCl_4$	[120]
Ag	$AgNO_3$	[121]

Besides the sol-gel method, a microemulsion method is often used for synthesis of silica coated magnetic nanoparticles. It produces monodisperse core-shell structures with high silica crystallinity [122] and desired narrow size distribution under mild conditions [123]. In this method, a suspension of the magnetic seeds in aqueous phase is prepared in advance, and then it is added dropwise to an oil solution containing one or several surfactants. The reverse micelle which has the hydrophilic heads contacting with the aqueous droplets and hydrophobic tail extended into the oil phase is formed, resulting in a stable water-in-oil (W/O) microemulsion. After the microemulsion become transparent, a silica precursor (TEOS) is added to the mixture under continuous stirring. The mixture is destabilised by an addition of large amounts of an aqueous phase. The obtained NPs are collected and washed. Another oil-in-water (O/W) method was also developed following a similar process while the surfactants form a micelle rather than a reverse micelle, which has the tails in the centre and hydrophilic heads in the bulk phase. A

gold shell can also be synthesized by the microemulsion method [94, 124-126].

The electrodeposition method is another option to obtain Au coating. In this method, a template of aluminium oxide is first immersed in a $HAuCl_4$ electrolyte to form a shell. Then the shell coated templates are added in the $HAuCl_4$ electrolyte. After proper deposition, the core-shell nanowires are formed [127, 128].

1.5.2 Synthesis of magnetic catalysts with a core-shell-shell structure

Composite magnetic catalysts with a core-shell-shell structure are synthesized for several reasons. First, as magnetic core has the poor bonding with certain types of catalysts, the middle layer acts as a platform to load the catalyst onto the outer layer [79, 80]. Secondly, the middle layer is synthesized as a barrier to avoid the direct contact between the magnetic core and the catalyst which might cause the change of their properties. For instance, Beydoun et al. [129] observed the photodissolution of titania shell at the boundary with the magnetic core, which changed the magnetic properties and reduced the catalytic activity of TiO_2. Thus a middle layer of SiO_2 is often introduced to prevent the electronic interactions [130-132]. Thirdly, an additional layer could enhance the properties of the outer shell or the magnetic core. In some cases, the outer shell is added to enhance the activity of the middle layer, such as $Fe_3O_4@TiO_2@Ag$ [133]. The magnetic properties of core are also reported to be enhanced by coating with a ZnO middle layer [134]. Also, an additional layer could further give the protection of the magnetic core, extending the lifetime of composite magnetic catalysts.

The shells are typically coated layer by layer onto the core by sol-gel method. Normally, the gel of the middle layer is coated onto the core first and then the as prepared materials are immerged in the sol containing the second precursors. After removing the surfactants, the magnetic catalysts with two shells are synthesized. A heterocoagulation colloidal process was reported by Costa et al [132]. In this process, a SiO_2 sol was mixed with a Fe_3O_4 sol first and then a TiO_2 sol was added. After spraying drying, a

Fe$_3$O$_4$@SiO$_2$@TiO$_2$ composite material was obtained. This technology is suitable for production of composite magnetic materials on a large scale.

1.5.3 Mechanochemical synthesis

Mechanochemical synthesis, which is usually performed in a ball mill, is a method using high energy compressive impact forces to grind the mixtures of powders together [135]. During the process, the change of the mixtures can be classified into five states (Figure 1.7), namely the initial period, the period of welding predominance, the period of equiaxed particle formation, the start of random welding orientation and the steady-state processing [136]. The powders of two components are firstly flattened, coalesced and fragmented. With the process going, the change turns from the physical binding to the chemical reaction, and finally the mixtures are scattered on atomic scale. The specific time of chemical change depends on the mill type, milling speed, temperature of the milling, ball-to-powder ratio and also the specific powders used [137].
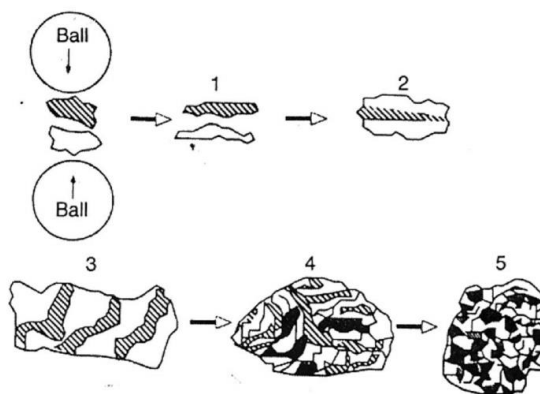
Figure 1.7 Scheme of powder evolution in five stages during ball mill [135]

Compared to the conventional synthesis, solid state synthesis uses less or no solvents and the steps are much simpler, which is environmentally-friendly and brings the convenience to scale up for industrial applications. In the first stage, this mechanochemical synthesis was widely applied to the synthesis of insoluble inorganic materials. With the development of complex heterogeneous catalysts, this method was gradually introduced to the manufacture of mixed metal oxides and ion-exchanged zeolites in

environmental catalysis, energy related reactions, and a series of chemical synthesis [138]. Several studies reported synthesis of magnetic catalysts by solid-state method. Fe_3Mo_3N and Co_3Mo_3N catalysts, that have both magnetic properties and catalytic activity in ammonia synthesis, were prepared by mechanochemical alloying. The gradual phase change in phase composition was observed after 5 h with a milling speed of 200 rpm and a ball-to-powder ratio of 19:1. [139]. Zeolitic imidazolate frameworks (ZIF-8) and Fe_3O_4@ZIF-8 composites were synthesized by mechanochemical synthesis as well, and the latter could be totally removed by an external magnet, indicating the uniformity of Fe_3O_4 distribution in the ZIF-8 zeolite framework after ball mill [140]. In our group, several $NiFe_2O_4$@TiO_2 composite magnetic catalysts were obtained by mechanochemical synthesis. It was shown that the specific adsorption value dropped after the longer milling time while the surface area remained near the same. The reaction rate in amide synthesis over ball milled $NiFe_2O_4$@TiO_2 composite catalysts was identical to that over the initial TiO_2. An optimum milling time was found out to be 0.5 h [1].

1.6 RF heating

RF heating corresponds to electromagnetic heating in the frequency range of 100-1000 kHz. The other two categories in electromagnetic heating are dielectric heating (in MHz range) and microwave heating (in the GHz range) respectively [141]. The comparison of these electromagnetic heating methods from different aspects is performed in Table 1.4. For microwave and dielectric heating, the reaction condition they could achieve and possibility of scaling up are quite limited by the equipment. Several drawbacks of microwave heating like safety issue, low penetration depth and uncontrolled heating limit the size of equipment which can be used, providing limited possibilities for scale-up [142, 143]. According to Moseley's report [144], there is no commercial microwave reactor which could meet the requirement for pharmaceutical industry. However, the requirements of RF heating on hardware are much easier to achieve and there is no significant limitation hindering its application towards industry. It was reported that RF

generators could also be combined with wind energy, providing a new way of green engineering [145].

Table 1.4 Comparison of RF heating and microwave/dielectric heating

	RF heating	Microwave/dielectric heating
mechanism	Magnetic relaxation, eddy current	Rotation of molecule's permanent dipoles in the dielectric
Heating property	Determined by magnetic material	Based on the dielectric constant of the molecules contained
Temperature limitation	Below the Curie temperature of magnetic material	Depend on equipment used
Scale-up	Easy to scale up	Limited by penetration depth of microwave field as well as the equipment
Application	Suitable for all chemical reactions	Magnetic compounds are not suitable

Different from the conventional heating, RF heating is regarded as a novel, green and highly efficient heating method. The efficiency of RF heating could be as high as 85% depending on the coil design [81]. In conventional heating, the start-up process is very slow due to the large heat capacity of additional equipment (heating rods, heat transfer medium etc.) and relatively low heat transfer rate from the heating elements to the catalysts. RF heating however could realize the rapid heating and be accompanied with the rapid cooling as well, if necessary. Also, as heat is generated from inside, the heat could be directly transferred from the heating source to the catalyst and reactants, avoiding the large heat loss during the process. As it is shown in Table 1.5, its efficiency of power transmission is much higher than other heating methods. In conclusion, RF heating as a novel heating method has a large potential on chemical synthesis.

Table 1.5 Power transmission of various heating methods [86]

Heating methods	Power transmission (W cm^{-2})
Convection	0.5
Irradiation	8
Heat conduction	20
Flame	1000
RF heating	30000

1.6.1 Mechanism of RF heating

In the RF range, the heat can be generated by eddy currents on a conductive material. If a magnetic material is applied, the relaxation loss is another source of heating. There exist two mechanism of relaxation namely Néel and Brownian relaxation. The rotation of magnetic moment inside the particle is called Néel relaxation while the rotation of the whole particle is named as Brownian relaxation which normally happens in a suspension of magnetic particles [146]. The hysteresis loss is the third type of heat generation if material is ferromagnetic. The type of the mechanism for heat dissipation depends on the particle size. For the size of the particles below superparamagnetic diameter, the heat generation is dominated by Brownian rotation while Néel relaxation loss gradually takes the place as the particle diameter roses [147, 148].

Table 1.6 Relationship between heating mechanism and particle size [72]

Particle size	$D \leq D_{sp}$[a]	$D \approx D_{sp}$	$D_{sp} < D < D_{sd}$[b]	$D \approx D_{sd}$	$D > D_{sd}$
Heat generation mechanism	Brownian[c]	Néel + Brownian	Hysteresis+ Néel + Brownian	Hysteresis	Hysteresis + Eddy current[d] + Anomalous[d]

a superparamagnetic diameter
b Single domin diameter
c only when medium is viscose
d at high frequency and high magnetic field

For ferromagnetic material, based on its hysteresis loop, the heat generated can be calculated by Eq. (1.1) [141].

$$P = \mu_0 \cdot f \cdot \oint_M H dM \qquad (1.1)$$

where P is the heat produced, μ_0 is the vacuum permeability, f is the frequency of the magnetic field, H is the intensity of the magnetic field and M is the magnetism of the measured sample.

1.6.2 RF-heated reaction system

Due to the efficient heating, RF brings the convenience to the areas that need high temperature operations such as alloy synthesis [149], formation of carbon nanostructures [150, 151] and silicon carbide [152, 153]. In these studies, a conventional furnace was replaced with an RF-heated furnace, where the magnetic sample holder or magnetic sample itself was surrounded by an induction coil.

The application of RF heating to catalytic reactions can be dated back to 1990, when various non-magnetic catalysts for steam reforming of heavy hydrocarbons were studied in the RF field generated with an induction [81]. Based on the heating mechanisms, the application of RF heating can be classified into two categories. The first method is to heat a metal reactor (surface heating) and the second method is to heat composite magnetic catalysts, which are placed into the reactor made from an RF transparent material and generate the heat inside the reactor (volumetric heating). In terms of using stainless steel reactor, Leclercq et al. coated $Pt-Al_2O_3$, Al_2O_3 and SnO_2 catalysts on the surface of a stainless steel tube which was placed in a Pyrex tube surrounded by an induction coil. It was demonstrated that a very high heating rate up to 800 °C/min and accurate temperature control could be achieved. Total transformation from isopropyl alcohol to CO_2 and H_2O happened in less than 30 s [154]. Pérez-Camacho et al. pelletized the perovskite-type mixed metal oxide catalysts and loaded them into a stainless steel reactor for the conversion of biogas to syngas. Under RF field, the

efficient heating with a heating rate of 100 °C/min and conversion as high as 76% were observed [145]. Similar method was applied to the regeneration of a filter blocked by the diesel particulate under a continuous air flow. The stainless steel meshes were heated by an induction coil to 600 °C at a frequency of 220 kHz to achieve the full recovery [155].

Prof Kirschning's group provided significant contribution regarding the application of composite magnetic catalysts under RF field. An RF-heated continuous reactor (RF-CR) for organic synthesis was set up at 25 kHz frequency provided by a U-shaped inductor (Figure 1.8 (a)). This concept was much simpler than a microwave flow reactor. Silica coated Fe_3O_4/Fe_2O_3 catalysts and a Pd functionalized catalyst were packed in a glass reactor to catalyse several organic reactions like transesterification, condensation to form thiazole, resulting in good yields from 63% to 92%. It also demonstrated a higher yield (80% vs. 65%) of certain organic reactions conducted in the RF-heated continuous reactor compared to that in the conventionally heated one [58], as the heat was directly generated inside the RF-heated reactor where reaction took place. A high-frequency magnetic field was generated by a coil-shaped inductor (Figure 1.8 (b)), providing the sufficient heating power for some nanostructured catalysts such as commercial MAGSILICA 300 (Evonik). A continuous synthesis of neurolepticum olanzapine in three consecutive RF-heated reactions was realized and the productivity was up to 3.97 mmol/(L·h) (Figure 1.9) [87]. To expand the range of possible applications of the commercial MAGSILICA catalyst, a gold functionalized MAGSILICA was studied in the oxidation of allylic and benzylic alcohols in a flow reactor [156].
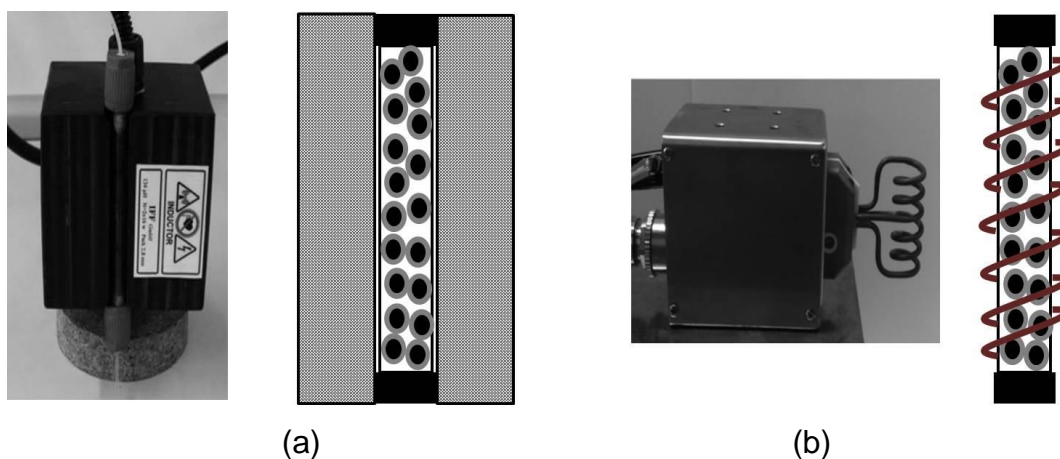
Figure 1.8 Flow reactor packed with magnetic catalysts in RF fields of (a) middle frequency (25KHz) [58] (b) high frequency (780-850 KHz) [87]
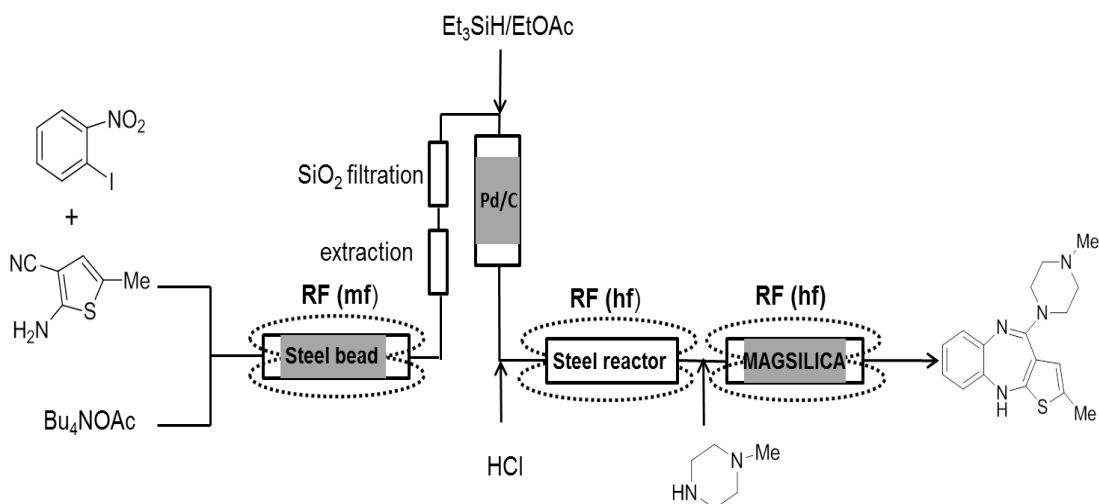
Figure 1.9 Multi-step synthesis of neurolepticum olanzapine in cascade RF-heated continuous reactors

The previous work in our group also promoted the application of RF-heated reactors. The work was firstly started in an RF-heated batch reactor. Stoichiometric amide thermal synthesis from different acids and amines was conducted in a vial where ferrite microparticles were heated by a coil-shaped inductor. At a current of 200 A at 287 kHz, the temperature could rise up to 100 °C in two min and a reactant conversion of 92% was obtained. It also showed that the influence of the electrical current on heating rate was more significant than the frequency of the electromagnetic field [15]. Moreover, an RF-heated flow reactor (Figure 1.10) was developed to realize a continuous production of amide over a $TiO_2/NiFe_2O_4$ catalyst obtained by a ball milling

method. The product yield was up to 50% at 170 °C and the catalyst deactivation was less than 30% in 15 h [1].
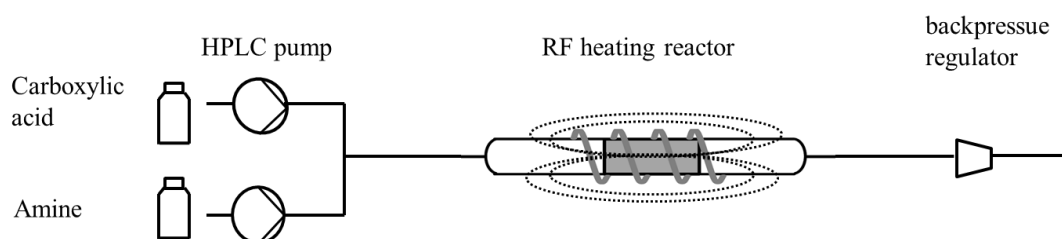
Figure 1.10 Schematic view of the RF-heated flow reactor for amide synthesis [1]

1.7 Design and operation of an RF-heated continuous reactor

1.7.1 Advantages of continuous reactor

The synthesis of fine chemicals nowadays relies almost exclusively on the batch reactor technology. Batch reactors allow multi-product manufacture from a single unit, which greatly reduces the initial capital cost of plants. At larger production scales, however, the inefficiencies of batch production cannot be discounted by flexibility. The dominant inefficiency is the poor use of the reactor volume, which arises from the batch operation mode itself because during reactor cleaning, recharging and discharging, no product is made by the reactor, but significant labour costs occur. Furthermore, batch reactors in multiphase catalytic reactions demonstrate a number of problems such as low heat and mass transfer coefficients and low energy efficiency resulting in higher environmental impact and increased operational and capital costs.

Even though batch reactors are employed widely in industry nowadays, flow technology has drawn much attention in academic field due to its advantages on synthesis of fine chemicals. Compared to batch reactor, continuous reactor has a much short processing time because of its non-stop production, leading to the cost and time saving. Mascia et al. [157] demonstrated that the processing time reduced from 300 to 47 h and number of necessary unit operations was reduced from 21 to 14 in a continuous process. Also, as

most of continuous reactors at the moment are micro or millireactors, the heat and mass transfer is very efficient, accelerating the reaction rates [158, 159]. Reaction conditions at each stage like temperature and pressure can be precisely monitored and controlled, making it easy to optimize the reaction process [160]. The sustainability is another strength of continuous reactor. Continuous reactor makes it possible to integrate all the synthesis steps from initial reactants to final products into a single production line [157]. For the reaction containing unstable or hazard intermediate, it can be easily protected by controlling the reaction conditions and converted to the next target chemicals in flow chemistry [161]. Finally, continuous reactor is easy to scale up by simply increasing the flow rates or extend the length or the diameter of catalytic bed.

1.7.2 Structure of the catalytic bed

In an RF-heated continuous reactor, CMCs were usually packed uniformly over the entire length of the catalytic bed [1, 58, 86, 87, 156]. As CMC can generate the equal heat in the uniform magnetic field, a temperature gradient is developing along the reactor. If heat loss via the fittings occurs, the temperature profile along the reactor is very uneven, resulting in a substantial temperature difference between the maximum and minimum value. The temperature difference observed in a 3 mm diameter reactor developed by Houlding et al. exceeded 75 °C and it increased at higher RF input powers [162] (Figure 1.11). This phenomenon hindered many aspects of RF-CR application. Firstly, the hot spot inside the reactor causes the faster deactivation of the catalysts and the decomposition of chemicals. This limits the range of possible reactions and the catalyst lifetime is short. Also, equipment which can stand for the highest temperature is needed, causing the unnecessary extra costs and safety issues. More importantly, this makes scale-up of the RF-CR quite hard. The temperature profile changes with the length of the reactor, making the performance of catalytic bed unpredictable. The temperature difference becomes larger once the length of the reactor is extended, requiring a redesign of the reactor. Under this situation, the RF-CR is difficult to scale up to the bench and industrial scale. Under this

circumstance, it is rather important to develop an RF-CR with a uniform temperature profile along the reactor length.
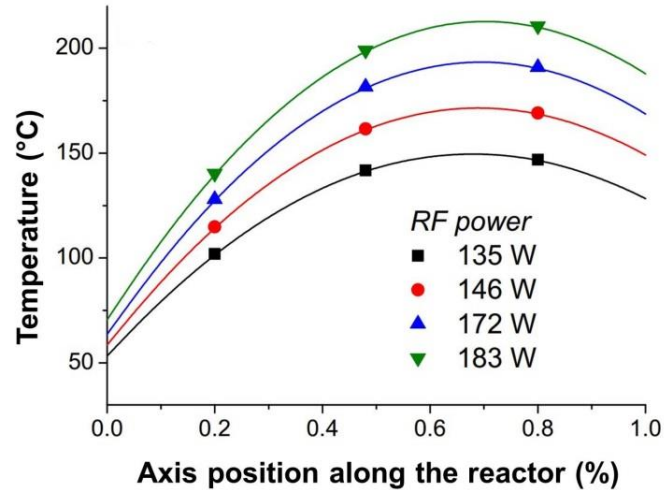
Figure 1.11 Temperature profiles along the RF-CR with a single 25 mm catalytic bed [162]

The temperature gradient can be reduced by a proper design of the packed bed [163]. The packed bed in an RF-CR can be split into several zones, sandwiched with inert zones where no heating occurs. Detailed simulation using convection and conduction heat transfer model allows to predict the length of each zone to realize a near-isothermal behaviour of the reactor (Figure 1.12 (a)). The temperature gradient decreased to 2 °C with three heating zones, which was significantly improved compared to that in the reactors with single or two heating zones (Figure 1.12 (b)). However, this isothermal behaviour could be only achieved at one specific flow rate. Once the flow rate or reaction temperature is changed, the heat balance will be broken, resulting in larger temperature non-uniformity.
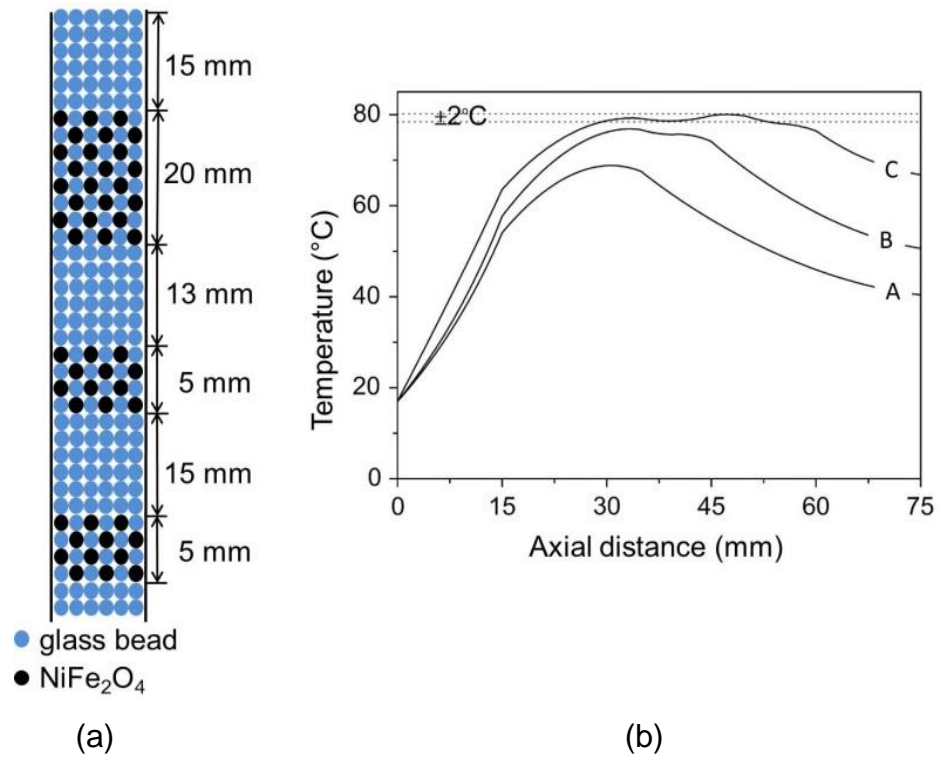
Figure 1.12 (a) Schematic view of the trickle bed RF-heated continuous reactor (b) Temperature profiles along the reactor. A - single heating zone, B - two heating zones, C - three heating zones [163]

Chapter 2

Experimental

2.1 Preparation of composite magnetic catalysts

2.1.1 Synthesis of sulfated P25 TiO₂ catalysts

To make sulfated titania, a desired amount of either a 1M sulfuric acid or ammonia sulfate solution was firstly dropped into the 40 mL deionized water. Then 1 g commercial P25 TiO_2 (Sigma Aldrich) was added into the solution. The obtained solution was further stirred at room temperature for 3 h and then centrifuged and washed by deionized water three times. The slurry was then dried overnight at 110 °C and calcined in a furnace at 400 °C for 2 h with a heating rate of 5 °C/min. The sulfated TiO_2 will be labelled as P25-XS, where index X stands for the nominal weight ratio of added SO_4^{2-}/TiO_2.

In a few experiments, to improve its wetting, an UV treatment of P25 catalysts with a 120 W UV lamp (Ace Glass) was performed in a chamber for 2 h prior to the sulfation process. The UV treated samples will be referred as UV-P25-XS hereafter.

In an opposite way, a silicate treatment was performed by immerging the sulfated P25 TiO_2 catalyst into a sodium silicate solution (TiO_2/SiO_2 = 2.25 wt.%) under continuous stirring at 40 °C for 24 h. After drying, the silicate treated sample will be named as Si-P25-XS. Part of the sample was further calcined at 400 °C for 2 h, which will be labelled as CSi-P25-XS.

2.1.2 Synthesis of nickel ferrite nanoparticles

All the chemicals required were purchased from Sigma Aldrich. Firstly, Iron (III) nitrate nonahydrate (51.7 g) and nickel nitrate hexahydrate (18.6 g) were

dissolved in ethanol (250 mL). Another solution was prepared by dissolving citric acid (36.9 g) in 150 mL ethanol. Then the citric acid solution was added into the former solution. After continuous stirring for 24 h, a 2 M ammonia solution was added dropwise to adjust the pH to 2. Under vigorous stirring, the temperature was increased to 90 $^\circ$C to evaporate the solvent until the total volume decreased to 150 mL. The obtained slurry was further dried in an oven at 90 $^\circ$C. Finally, the solids were grinded and then calcined at 700 $^\circ$C for 1 h with a heating rate of 2 $^\circ$C/min.

2.1.3 Mechanical mixture of sulfated TiO_2 and $NiFe_2O_4$ particles (T1 CMC)

The sulfated TiO_2 and $NiFe_2O_4$ particles (125 – 250 μm) were added into a vial with a certain weight ratio. The vial was then shaken by a laboratory digital shaker at the speed of 100 min^{-1} for 2 h. The mixture of the resulted particles will be named as T1-Y, where index Y represents the weight fraction of titania.

2.1.4 Mechanochemical synthesis of $TiO_2/NiFe_2O_4$ catalysts (T2 CMC)

To synthesize the CMCs, certain amounts of sulfated TiO_2 and magnetic nanoparticles were mixed and milled in an agate jar with 6 balls (Retsch planetary ball mill PM 400) at 300 rpm for 30 min. The obtained materials will be labelled as T2-Y, where index Y represents the weight fraction of titania in the CMC. The spent T2-Y will be named as ST2-Y hereafter.

2.1.5 Synthesis of $NiFe_2O_4@TiO_2$ core-shell catalysts (T3 CMC)

Solution A was prepared by redispersion of the 3 g nickel ferrite nanoparticles in a water (60 mL) /ethanol (210 mL) solution containing 2 M ammonia solution (15 mL) under sonication for 2 h. It was left overnight and then 0.3 g cetrimonium bromide (CTAB) was added under sonication for 2 h. Being left overnight again, 360 mL ethanol was added under continuous stirring. To prepare titania sol, tetrabutyl titanate (TBT, 85 mL) and diethanolamine (25 mL) with ethanol (285 mL) were firstly mixed. After

continuously stirring for 2 h, another solution containing ethanol (100 mL) and distilled water (10 mL) was then added dropwise (20 mL/h) into it. The mixture was stirred for 24 h and left for another 24 h, resulting in 0.48 mol/L TiO_2 sol (solution B). In the next step, the desired amount of solution B was added dropwise (20 mL/h) to solution A under vigorous stirring for 48 h. The temperature of the suspension was increased to 40 °C under reflux for 24 h and then further increased to 60 °C to evaporate until colloidal deposit was obtained. The obtained solids were dried in the oven at 80 °C and calcined at a desired temperature for 1 h at a heating rate of 1 °C/min under air flow. These samples will be referred as T3-Y-Z, where index Y represents the weight fraction of titania in the CMC and index Z stands for the calcination temperature. Index RT refers to the as-synthesized samples. The spent CMC (after the reaction) will be named as ST3-Y-Z.

2.1.6 Synthesis of NiFe$_2$O$_4$@SiO$_2$@TiO$_2$ core-shell-shell catalysts (T4 CMC)

Solution A and B as mentioned in the synthesis process of NiFe$_2$O$_4$@TiO$_2$ core-shell material were prepared in advance. An additional 0.49 mol/L silica sol (solution C) was prepared following the same procedure as solution B except for the precursor that was changed to tetraethyl orthosilicate. In a typical procedure, 12.5 mL solution C was added dropwise into solution A under continuous stirring. After aging for 2 days, the solution was heated to 40 °C under reflux to promote the formation of silica gel. Then the suspension was slowly evaporated at 60 °C until it became viscous. It was further dried at 80 °C and calcined at 700 °C for 1 h at a heating rate of 2 °C/min. The obtained NiFe$_2$O$_4$@SiO$_2$ composite nanoparticles were then re-dispersed in the way of preparing solution A.

To coat the TiO$_2$ onto the NiFe$_2$O$_4$@SiO$_2$ nanoparticles, 12.5 mL solution B was added dropwise into the prepared suspension of NiFe$_2$O$_4$@SiO$_2$ and the same procedure before the calcination step was undertaken as that in the process to obtain NiFe$_2$O$_4$@SiO$_2$ nanoparticles. The calcination was performed at a desired temperature for 1 h at a heating rate of 1 °C/min

under air flow. The obtained sample will be referred to as T4-Y-Z, where index Y represents the weight fraction of titania in the CMC and index Z stands for the calcination temperature.

2.1.7 Sulfation of T3 and T4 composite magnetic catalysts

Two methods were used to sulfate the $NiFe_2O_4@TiO_2$ (T3 CMC) and $NiFe_2O_4@SiO_2@TiO_2$ (T4 CMC) catalysts. For the first route, the prepared CMCs were mixed with a certain amount of 1M sulfuric acid in 40 mL deionized water separately at room temperature for 3 h. Then the CMCs were washed three times by water and dried overnight. Afterwards, they were calcined at 400 °C for 2 h with a heating rate of 5 °C/min. The samples will be named as T3a-Y-Z-S and T4a-Y-Z-S, where index Y represents the weight fraction of titania in the CMC and index Z stands for the calcination temperature. Index S here represents sulfation.

In another method, the as-synthesized T3 and T4 CMCs were mixed with a certain amount of 1M sulfuric acid in 40 mL deionized water for 3 h. The water was gradually evaporated at 90 °C until the residue became slurry. Then the slurry was dried overnight at 90°C and calcined at 500 °C for 1 h with a heating rate of 1°C/min under air flow. The CMC obtained will be labelled as T3b-Y-Z-S and T4b-Y-Z-S.

2.2 Characterization

2.2.1 XRD

The phase composition was analysed by powder X-ray diffraction (XRD) using a diffractometer (PANalytical Empyrean) with a Fe filtered Co Kα radiation (0.179 nm). The spectra were recorded at a scanning rate of 2 °2θ min^{-1}. The resulting data were recalculated into more traditional Cu Kα radiation (0.154 nm) source for presentation.

2.2.2 SEM-EDS

Morphology of the obtained nanoparticles was studied by scanning electron microscopy (SEM, Carl Zeiss Sigma Field Emission Microscope). The corresponding element composition and distribution were analysed by X-ray energy dispersive spectroscopy (EDS). The powdered sample was applied on an adhesive conductive tape and studied without metal coating.

2.2.3 VSM

The magnetic properties of the CMCs at room temperature were measured by a vibrating sample magnetometer (VSM, Oxford MagLab) equipped with a 2 T electromagnet. The saturation magnetization (Ms) and coercivity (H_C) was evaluated from the hysteresis loop. The magnetism at different temperatures was measured by a vibrating sample magnetometer (Princeton Measurements Corporation MicroMag 3900 VSM) equipped with a 2 Tesla electromagnet at different temperatures in the range from 298 to 773 K.

2.2.4 N$_2$ adsorption/desorption isotherms

The specific surface area and the total pore size were determined by N$_2$ adsorption/desorption isotherms measured at -196 ⁰C using a porosimeter (ASAP2010). Prior to analysis, the samples were degassed under vacuum by staying at 250 ⁰C for 1 h.

2.2.5 TEM

The microstructure analysis was performed with a JEOL2000fx transmission electron microscope (TEM) using a W/LaB6 filament operating at 200 kV, with images captured using a GATAN ORIUS 11 megapixel CCD camera. The sample was dispersed in ethanol under sonication and a droplet of the suspension was applied on the carbon-coated copper grids.

2.2.6 TPO

Temperature programmed oxidation (TPO) analysis was performed with the spent samples placing 50 mg of the sample into a U-shaped quartz tube between two plugs of quartz wool. After waiting for 1 h at 25 $^{\circ}$C in the flow of N_2, the flow was switched to 1% O_2, 1% Ar (internal standard) in N_2 and the temperature was increased linearly at a rate of 5 $^{\circ}$C/min. The concentrations of CO, CO_2 and H_2O were recorded by a quadrupole mass spectrometer (OMINI star).

2.2.7 XPS

The surface chemical composition and electronic state of catalysts were determined by X-ray photoelectron spectroscopy (XPS). The data were obtained using an ESCALab250 electron spectrometer (Thermo Scientific Corporation) with a monochromatic 150 W Al Kα radiation. Pass energy for the narrow scan was 30 eV. The base pressure was 6.5×10^{-10} mbar. The binding energies were referenced to the C1s line at 284.8 eV.

2.2.8 TG-DTA

The thermogravimetric and differential thermal analysis (TG-DTA) were obtained by a STA 449 C Netzsch Analyser at a 10 mL/min flow of 20% O_2/N_2 mixture and a heating rate of 10 °C/min from room temperature to 1000 °C. The alumina powder was taken as the reference sample.

2.2.9 FT-IR

The chemical composition was confirmed with a Fourier transform infrared spectrometer (FT-IR, Avatar360, Nicolet) in the wavenumber range of 2000-400 cm^{-1}. Samples' spectra were recorded by transmission in dry air atmosphere through a pastille made of a few milligrams of sample mixed with KBr.

2.2.10 FT-IR study of pyridine adsorption

The identification of acid sites was performed by FT-IR spectroscopy after pyridine adsorption. A sample was placed in a flow ceramic crucible in the FT-IR cell with a temperature controller. A Bruker Vertex 70 FTIR spectrometer equipped with a liquid N_2-cooled detector was used. Two 4-way valves (VICI) were installed to switch the gas between the Ar and pyridine. Prior to the experiments, the catalyst was degassed by heating up to 150 °C for 0.5 h under a 50 mL/min Ar flow. After it cooled down to room temperature, the pyridine flow was fed continuously for 0.5 h. Then the temperature of the cell was increased to 40°C. After temperature became stable, Ar was fed in and the pattern was recorded with the FT-IR spectrometer. The same procedure was repeated at 100, 150 and 200 °C.

2.2.11 Specific absorption rate measurement

10 mg of sample and 50 µL deionized water were added into a glass tube (i.d 5 mm). The tube was inserted into an insulated jacket and then placed along the centre axis of a 5-turn coil which connected to an RF inductor. To measure the temperature, a fibre optics temperature sensor (Fiso FOT-L-SD) connected to a signal conditioner (Fiso FPI-HR equipped with the Evolution software) was inserted in the tube (Figure 2.1 (a)). The RF field was turned on for 30 s at a current of 200 A. The temperature was recorded as a function of time for 60 s (Figure 2.1 (b)). The first section of the curve was due to the delay of the sensor signal which was caused by heat transfer from the solution to the measured element. The specific absorption rate (SAR) was calculated from the linear section of the curve by Eq. (2.1). This approach is widely adopted to determine the heating property of the material [82, 164].
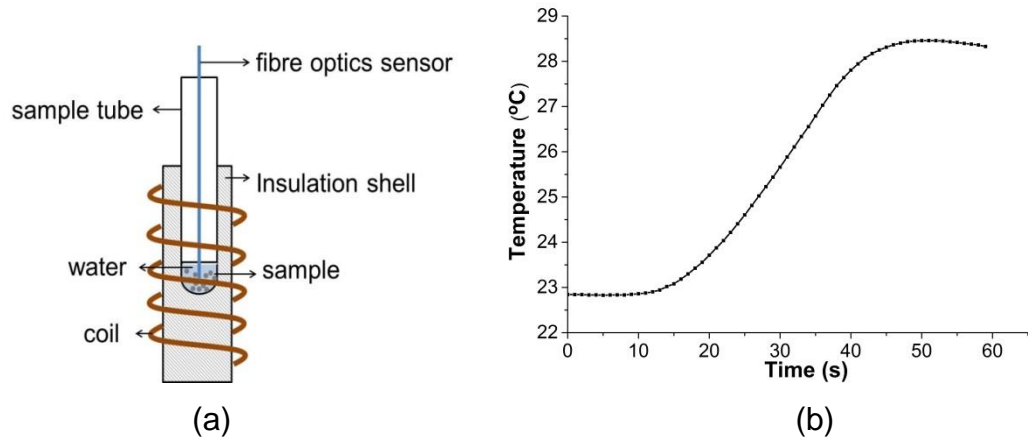
Figure 2.1 (a) Schematic view of SAR-testing device (b) A typical heating curve of nickel ferrite material

$$SAR = \frac{\sum_i (m_i C_{p,i})}{m_{sample}} \cdot \frac{d(T)}{d(t)} \qquad (2.1)$$

where m_i and $C_{p,i}$ represent the mass and heat capacity of each component in the tube respectively. $d(T)/d(t)$ is the slope of linear line from the heating curve. The value of heat capacity for each component is listed in Table 2.1.

Table 2.1 Heat capacity of $NiFe_2O_4$ and water

Component	Heat capacity ($J\ g^{-1}K^{-1}$)
$NiFe_2O_4$	0.62
Deionized water	4.18

2.3   RF heating module

The high frequency alternant magnetic field was provided by a copper coil connected to a 1 kW induction heating generator (Ambrell Easyheat 0112). The coil and electronic module were cooled with water. The water temperature was controlled at 20 °C with a chiller (WKL1000 Lauda). The RF frequency was automatically adjusted in the 100-500 kHz range depending on the induction of the coil to run the RTL circuit in resonance. The frequency can be adjusted with the number of turns in the coil, the coil diameter and the coil length.

Figure 2.2 Image of coils (upper left), fibre optics signal conditioner (upper right) and induction heating units (bottom)

To limit the range of operational frequencies, two induction coils were used in all experiments. The physical characteristics of two coils are listed in Table 2.2. The temperature was measured by fibre optics temperature sensors (Opsens) controlled with a PID controller (appendix-A).

Table 2.2 Coils configuration

	Diameter (mm)	Length (mm)
5-turn	40	55
8-turn	38	70

2.4 Catalytic activity measurements

2.4.1 Continuously stirred tank reactor

Both initial screening of catalytic activity and detailed reaction kinetics were studied in a 160 mL continuously stirred tank reactor (Parr 4564). Typically,

100 mL p-xylene solution of 4-phenylbutyric acid, aniline and tetradecane (internal standard for GC) were premixed with a certain amount of catalyst. After the reactor was tightly sealed, it was firstly purged by N_2 three times and then pressurized to 6 bars. The heating rates and the reaction temperature were controlled by a PID temperature controller (Parr 4848). An impeller with four blades was used to stir and stirring speed of the reactor ranged from 100 to 1500 rpm. Sample could be collected from a sample tube at regular time intervals. The solution collected was diluted 10 times by p-xylene for GC analysis.

Gas chromatography analysis was performed by a Shimazu 2010 plus GC, equipped with a fused silica capillary column (Length: 60 m, internal diameter: 0.53 mm, film thickness: 3.0 µm) and an FID detector. The GC analysis method is described in appendix B.

2.4.2 Conventionally heated continuous reactor

The conventionally heated continuous reactor (CH-CR) used in this study (internal diameter: 6.6 mm, maximum length: 150 mm, Omnifit HiT) is shown in Figure 2.3. It has one fixed plug and one adjustable plug, which is allowed to change the length of catalytic bed. Fibre optic temperature sensors (sensitive zone: 5 mm Opsens, OTG) were attached on the reactor surface to measure the temperature. Under conventional heating, a heating tape was attached tightly on the inlet tube and the reactor. The power supplied was controlled by a PID controller (Electrothermal). Glass wool was wrapped around the reactor as insulation.

The reactant flows (carboxylic acid and amine) were fed with two HPLC pumps (Shimadzu LC-20ADXR) and premixed in a T-mixer. The vessels with reactants were bubbled by a continuous N_2 flow to remove dissolved oxygen before and during the process. The pressure was maintained at 7 bars with a backpressure controller placed downstream of the reactor to avoid the solvent boiling. The samples were collected for GC analysis at regular time intervals and then diluted 10 times by p-xylene.
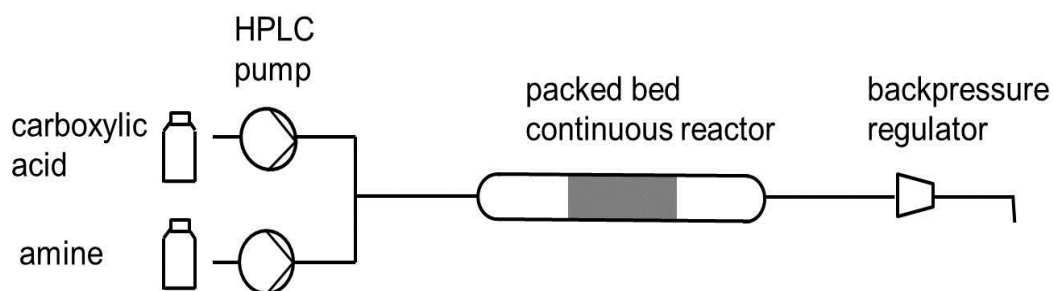
Figure 2.3 Scheme of packed bed continuous reactor

2.4.3 RF-heated continuous reactor

Under RF heating, the reactor described in section 2.4.2 was placed along the centreline of the coil connected to the same RF generator (1 kW, 100-400 kHz, Easy Heat) (Figure 2.4).

(a)   (b)
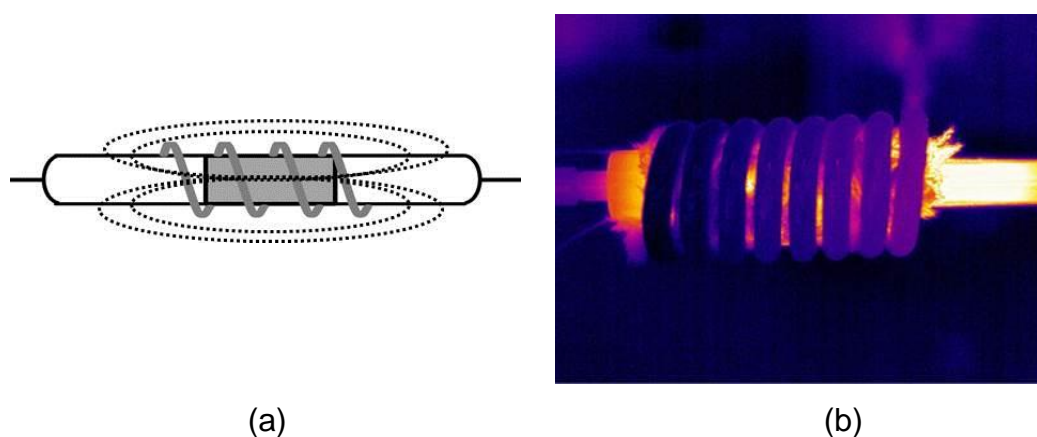
Figure 2.4 (a) Schematic view of RF-CR (b) Thermal image of RF-CR taken by an infrared camera (yellow – hot zone, purple – cool zone)

A single-zone RF-CR packed with T2 CMCs (fraction: 125-250 µm) was developed. Glass beads (fraction: 106-125 µm) were used to separate the CMC bed and the adjustable plug, and also to condition the flow prior entering into the reactor. Another glass bead zone at the end of the reactor bed was placed to keep the catalytic bed in the correct position. Two fibre optics sensors were attached along the reactor surface to measure the temperature. The power supplied was changed manually to achieve the reaction temperature.

The structure of RF-CR was adjusted to compare the catalytic activity of different CMCs. In order to keep the reaction temperature the same for all

experiments and reduce the temperature gradient under RF heating, the length of the packed bed was limited to 5 mm. The preheating of the reaction mixture was realized in a 5 mm section of Fe_3O_4 particles (fraction: 125-250 μm). The generator input power was controlled with a PID controller and the temperature was maintained within 0.1 K of the set-point value (Figure 2.5).
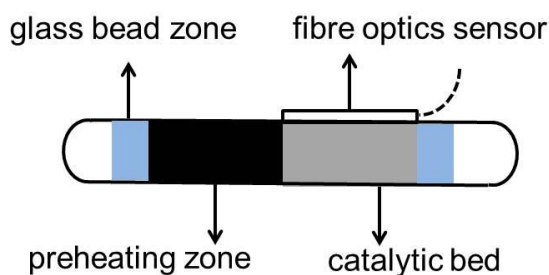
Figure 2.5 Schematic view of the RF-CR for catalytic activity test of CMCs

2.5   Catalyst regeneration

The spent T2 CMCs were recovered by calcination. In a typical experiment, the catalyst was heated inside the furnace with a heating rate of 5 °C/min to 400 °C for 1 h under air flow. The regenerated T2 CMC will be labelled as RT2-Y-C, where C represents the number of regeneration cycles. Same calcination procedure was also used to recover T3 CMC. The samples after this treatment are named as TRT3-Y-Z. The index Y represents the weight fraction of titania in the CMC and index Z stands for the calcination temperature.

Chemical regeneration was used for regeneration of T3 CMC as well. The spent T3 CMC was mixed with 20 mL 35 wt.% hydrogen peroxide solution at 90 °C for 20 h under continuously stirring. The CMC after treatment was labelled as WRT3-Y-Z hereafter.

2.6   Development of an isothermal RF-heated continuous reactor

A two-point controlled isothermal RF-CR system was set up as shown in Figure 2.6. Before the catalytic zone, the reactor was packed with a 35 mm

preheating zone using pelletized Fe_3O_4 microparticles (fraction: 500-707 μm). A 5-mm glass bead zone was placed between these two zones. At least three fibre optics sensors (FO1, FO2, FO3) were attached to the external reactor wall every 5 mm and the number of the sensors used were determined by the length of the catalytic bed. In the PID assisted two-point controlled RF-CR, FO2 sensor was connected to the PID controller. The heat generation in the preheating zone was controlled by adjusting the length of preheating zone inside the coil and the current applied was automatically adjusted by the PID controller. In this way, the energy provided to the preheating and catalytic zones was controlled separately, making this system suitable for various reaction conditions. In a typical experimental operation, the value of reaction temperature in the controller was firstly set to 150 °C, and then RF heating was started. After FO2 reached to 150°C, the reactor was manually moved along the centre axis of coil to adjust the length of preheating zone inside the coils until the reading of FO1 was150 °C. The temperature profile of the catalytic bed was measured by the readings from the fibre optics temperature sensors along the reactor.
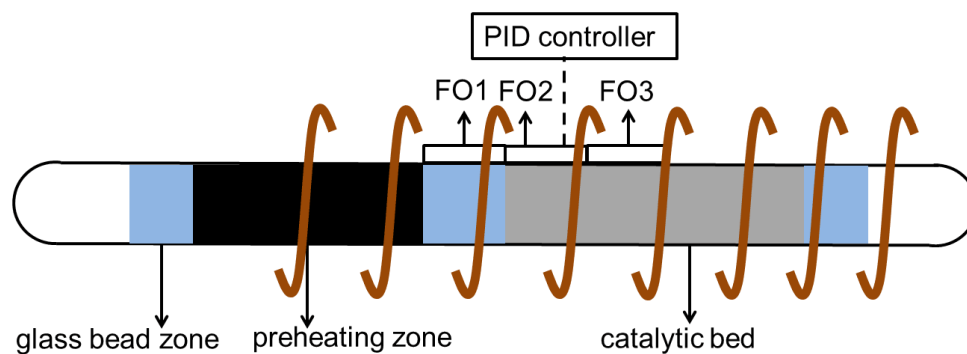
Figure 2.6 Schematic view of two-point controlled isothermal RF-CR

For the manually two-point controlled RF-CR, the set-up of the RF-CR system was the same as shown in Figure 2.6 without PID connection. In this way, both the length of preheating zone in the coil and electric current were controlled manually. They were continuously adjusted until reaching to the minimum temperature gradient along the catalytic bed.

Chapter 3

Catalyst development for direct amide synthesis

3.1 Introduction

As thermal direct amidation undergoes rather low reaction rate, the choice of catalyst is of great importance to promote the reaction rate. A very active catalyst makes it possible to produce the amide in a continuous reactor. In this chapter, the catalysts were firstly screened in the direct amide synthesis reaction and a kinetic study of the reaction over the optimal catalyst was performed in the batch reactor. The selected catalyst was further optimized by different treatments to enhance the catalytic activity. Finally, the optimized catalyst was loaded in the conventionally heated flow reactor to realize the continuous production. The variations of reaction rate with reaction temperature and time on stream were also studied in the CH-CR.

3.2 Direct amide reaction selection

To perform the amide synthesis in the fixed bed continuous reactor, several factors of the reaction should be firstly considered. The formation of an ammonium carboxylate salt is one of the main concerns. If the reactants are more likely to react towards salt formation, the large production of amide could not be realized in the flow reactor. More importantly, the salt which is insoluble in organic solvents may cause the serious flow blockage in the continuous reactor. Besides, as the activity of different reactants is various, the carboxylic acid-amine pairs which have rather low reaction rates without a catalyst provide the possibility to enhance the reaction rate by the catalysts. Based on the data presented in Table 1.1, the amidation between 4-

phenylbutyric acid and aniline formed no salt in the reaction mixture and the amide yield without catalyst was as low as 4% after 48 h, making this group a perfect reaction model to explore the catalysis and adopt the process in the flow reactor (Figure 3.1).
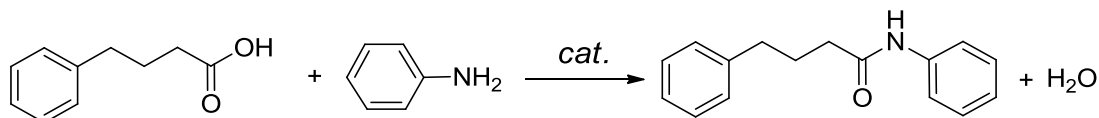
Figure 3.1 Amidation of 4-phenylbutyric acid and aniline

3.3 Kinetics study

3.3.1 Reaction condition study

For a heterogeneous reaction, the overall reaction rate depends on both mass transfer rate and the chemical reaction rate on the active sites. If mass transfer is much slower than the reaction, the total reaction rate is mass transfer limited. If it behaves opposite, it is kinetically limited. To study and compare the catalytic performance of various catalysts in the batch reactor, a proper reaction condition should be chosen first to perform the reaction under kinetic control. For the reaction in the batch reactor, there exist two parameters affecting the mass transfer rate, namely the stirring rate and catalyst loading. The relationships between the reaction rate and these two parameters are shown in the Figure 3.2.
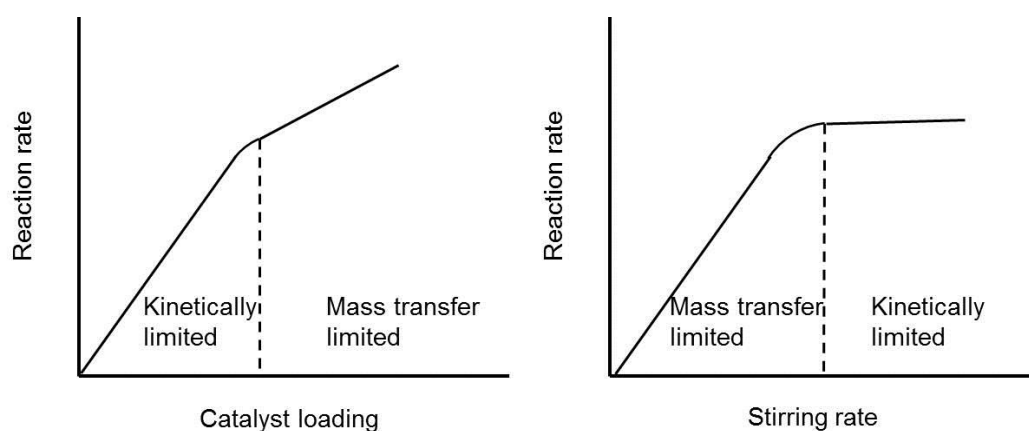
Figure 3.2 Relationship of reaction rate vs catalyst loading and stirring rate

To avoid mass transfer limitations, a kinetic study of amidation of 4-phenylbutyric acid and aniline in the batch reactor was performed at the highest possible temperature (200 °C). The amount of P25 TiO_2 catalyst in the reactor and the stirring speed were varied to observe the onset of mass transfer limited regime. At first the stirring speed was kept constant at 950 rpm and three different amounts of catalyst were studied: 114, 165 and 203 mg. In the next series of experiments the amount of catalyst was fixed at 165 mg and several stirring speeds of 645, 857, 1053, 1500 rpm were studied.

The reaction rate showed a linear dependence on the mass of the P25 TiO_2 catalyst in the studied range of catalyst concentrations while the value was rather constant as the stirring rate increased from 645 to 1500 rpm (Figure 3.3), indicating both selected ranges were located in the kinetics regime. Based on these results, a titania loading of 165 mg (10 wt.%) and a stirring rate of 950 rpm were selected as the reaction conditions in the following experiments conducted in the batch reactor.

(a)   (b)
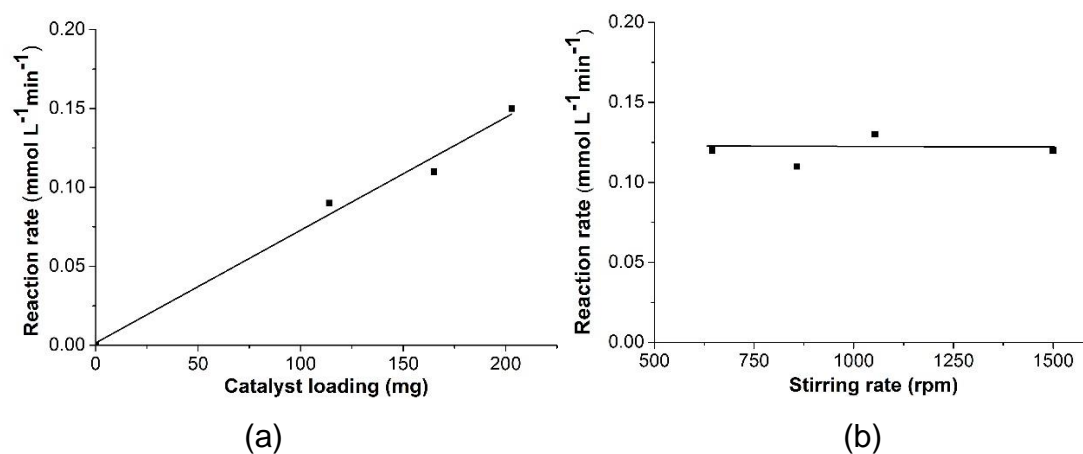
Figure 3.3 Reaction rate as a function of (a) catalyst loading and (b) stirring rate. Reaction conditions: 50 mmol/L 4-phenylbutyric acid and 50 mmol/L aniline in 100 mL p-xylene, 200 °C, 6 bars.

3.3.2 Kinetics study of amide synthesis from 4-phenylbutyric acid and aniline

Since the non-catalytic amide synthesis with 4-phenylbutyric acid and aniline reacted at an extremely low reaction rate, to explore the reaction kinetics, the reaction was conducted over a commercial P25 TiO_2 catalyst. As reactants added were equimolar, the variable in the kinetics equations can be

simplified to a single concentration (either acid or amine). The corresponding linearized equations are listed in Table 3.1. The experimental data was fitted by using equations of different orders (Figure 3.4). Judging from the value of R^2, the relationship between the deformation value of aniline concentration (C_A) and reaction time was the most accurately described using the second order kinetics. The same result was also confirmed by Houlding's research [162].

Table 3.1 Reaction rate equations of zero, first and second orders kinetics

Reaction order	Reaction rate	Linearized equation	
Zero order	$r = k$	$C_{A_0} - C_A = kt$	(3.1)
First order	$r = kC_A$	$ln(C_{A_0}) - ln(C_A) = kt$	(3.2)
Second order	$r = kC_A^{\,2}$	$\dfrac{1}{C_{A_0}} - \dfrac{1}{C_A} = kt$	(3.3)
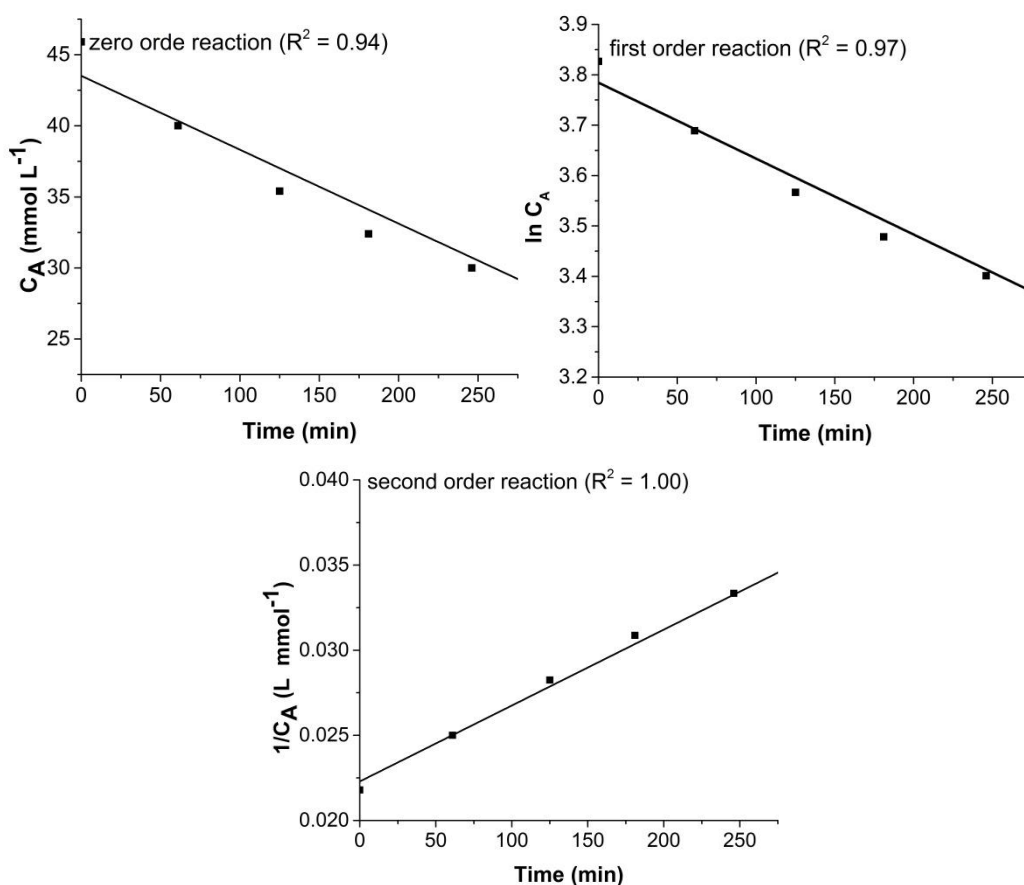
Figure 3.4 Linear fitting of rate equations of different order kinetics. Reaction conditions: 46 mmol/L 4-phenylbutyric acid and 46 mmol/L aniline in 100 mL p-xylene, 165 mg P25 TiO_2, 200 °C, 6 bars.

However, the reaction rate over sulfated titania was observed to sharply slow down after 400 min. To further explore the yield curve, the reaction time was extended up to 29 h. It can be seen from Figure 3.5 that the amide yield increased very slowly after 8 h and only reached to 62% amide yield after 22.5 h. The difference between the experimental data and ideal reactant concentration obtained using the second order kinetics is presented in Appendix C.1.

Figure 3.5 Amide yield as a function of time in the batch reactor. Reaction conditions: 50 mmol/L 4-phenylbutyric acid and 50 mmol/L aniline in 100 mL p-xylene, 165 mg P25-7.5S catalyst, 200 °C, 6 bars.

As the amide yield in the reaction of 4-phenylbutyric acid and aniline was proved by Comerford et al. [24] to be not affected by the removal of water from the reaction mixture, this demonstrates that it is an irreversible reaction, which is also agrees with the conclusion from Houlding's research [162]. Because the reaction temperature was as high as 200 °C, the organic species in the reactor could have easily decomposed to form the coke on the surface of the catalyst [1]. The deactivation of the catalysts by the formed coke might have been the main reason for the significant decrease in the reaction rate with time. The effect of temperature on catalytic deactivation was studied in Section 3.7.2 and the coke was analysed and studied in the sections exploring the deactivation mechanism of each magnetic catalyst. The production inhibition which was possibly caused by the adsorption of water on the titania catalyst might have also contributed to the partial loss of the catalytic activity. The effect of water adsorption on the acid sites of the catalysts has been reported in literature and the specific change brought by

the water depended significantly on the catalyst nature [165-169]. For the titania in particular, He et al. demonstrated chemisorption of water on anatase TiO_2 by both experiments and simulation [170]. Adsorbed water was found to negatively affect the interaction between carboxyl group and TiO_2 surface and thus decreased the photocatalytic activity of TiO_2 according to Nosaka et al [167]. Kulkarni et al. found out that the adsorption of the original molecules on both the Lewis and Brønsted acid sites were replaced by the water molecules once TiO_2 or sulfated TiO_2 was exposed to water [169]. In this case, catalyst tolerance to the aqueous environment was considered as the key factor by Comerfold et al. [24] when K60 silica catalyst was applied to catalyse the direct amide synthesis. Thus it can be deduced that in the long-term stability experiment (Figure 3.5), the catalytic activity was suppressed by the coke formation as well as the adsorption of water obtained in the reaction. The reaction rate has reduced to the un-catalysed value after a long-time reaction. The effect of water on the activity of the optimal titania catalyst was further confirmed in Section 3.6.3.

Amide which was the main product could also be the reason causing the product inhibition. To verify it, the reaction was firstly conducted under the original reaction condition in the first 40 min. Then the reactor was quickly cooled to 50 °C and an extra 25 mmol/L amide was added. The reactor was sealed, flushed, pressurized and temperature was raised to 200 °C again. As it can be seen from Figure 3.6, the reaction rate after the addition of amide did not decrease compared to the original value, which was 0.19 and 0.15 mmol $L^{-1}min^{-1}$ respectively. This phenomenon indicates that the concentration of amide did not have the effect on the reaction rate, thus it is not the reason causing the product inhibition.
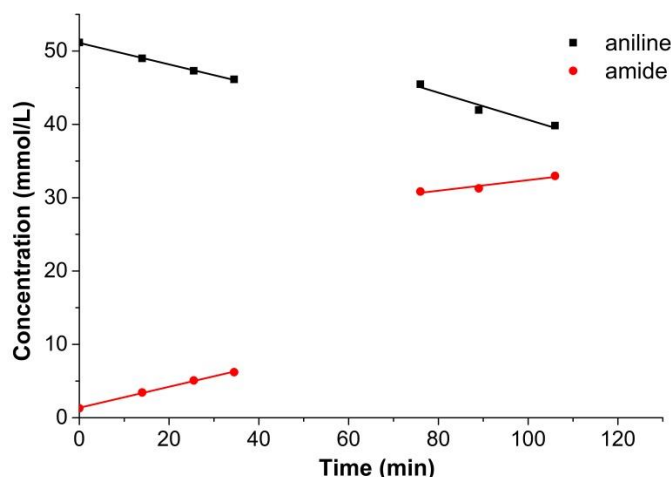
Figure 3.6 Concentration profiles of aniline and amide as a function of time in the batch reactor. Reaction conditions: Initial mixture: 50 mmol/L 4-phenylbutyric acid and 50 mmol/L aniline in 100 mL p-xylene, 121 mg P25-7.5S catalyst, 200 °C, 6 bars. Extra 25 mmol/L amide was added into the mixture after 40 min.

As both product inhibition and coke caused the decrease of the reaction rate in Figure 3.5, to properly describe the effect of water inhibition observed in the batch reactor, the data in first 400 min when coke had little impact on activity was used and fitted. The kinetics considering product inhibition describing can be described by Eq (3.4). The reactant concentration (C_A) as a function of time (t) was firstly derived and then fitted into the equation (Figure 3.7).

$$\frac{dC_A}{dt} = -\frac{kC_A^{\,2}}{1+k_pC_p} \tag{3.4}$$
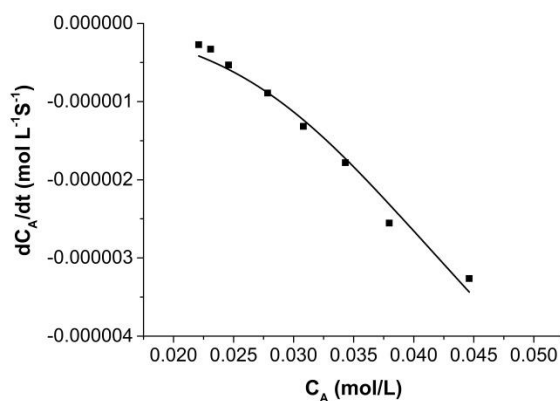
Figure 3.7 Fitting of the experimental data to the equation considering the product inhibition

50

Where C_A and C_p is the concentration of aniline and amide respectively. k is the reaction rate constant and k_p is the product inhibition constant. The obtained values of k, k_p are 2.0 x10^{-3} L mol^{-1}s^{-1}, 26 L/mol respectively with R^2=0.95.

3.4 Screening of heterogeneous catalysts in direct amide synthesis

Even though certain types of heterogeneous catalysts are considered as solid acids, the strength and distribution of acid sites vary with the type of the catalyst, further affecting the catalytic performance on different amide synthesis. Too weak acid sites will not influence the electron density around the carbon of carboxyl group significantly, showing no catalytic activity. Nevertheless, the acid sites which are too strong may cause the blockage of sites by slow desorption of the products. Also, strong Lewis acid sites could react with the water as the by-product in the direct amidation and turn into Brønsted acid sites which are not reactive according to the mechanism [34]. The catalytic activities of several heterogeneous catalysts were tested in the batch reactor and the corresponding reaction rates of synthesizing 4, N-diphenylbutyramide are listed in Table 3.2.

Table 3.2 Reaction rates of 4,N-diphenylbutyramide formation over different heterogeneous catalysts. Reaction conditions: 50 mmol/L 4-phenylbutyric acid and 50 mmol/L aniline in 100 mL p-xylene, 165 mg heterogeneous catalyst, 200 °C, 6 bars.

Type of catalysts	Reaction rate (mmol L^{-1} min^{-1})	Source
P25 TiO$_2$	0.170	Commercial
Sulfated P25 TiO$_2$	0.200	Lab-made
ZrO$_2$	0.005	Commercial
Sulfated ZrO$_2$	0.004	Lab-made
Rutile TiO$_2$	0.003	Commercial
Silica gel	0.010	Commercial
silica gel after700 °C	0.008	Lab-made
CeO$_2$	0.012	Commercial

Type of catalysts	Reaction rate $(mmol\,L^{-1}\,min^{-1})$	Source
99% H_2SO_4	0.020	Commercial
ZSM	0.003	Commercial
Al_2O_3	0.000	Commercial

In the amidation of 4-phenylbutyric acid and aniline, the higher reaction rate was observed over a P25 TiO_2 catalyst which contained both the anatase and rutile phases. However, the rutile resulted in a rather low reaction rate, indicating the active sites were located onto anatase surface accelerating this reaction. However, the reaction rate was 0.020 mmol $L^{-1}min^{-1}$ when concentrated sulfuric acid, which is a typical strong Brønsted acid, was used, demonstrating that strong Brønsted acid could not be an efficient catalyst for this reaction. The reaction mechanism by strong Brønsted acid includes the attack of the oxygen atom in double bond of the carbonyl group by the large amount of dissociative protons. The break of the double bond makes the carbon atom in the carbonyl group more positive and be easier to react with aniline. The poor performance of other solid acids was attributed to the improper strength or distribution of acid sites on the surface. The positive effect of sulfation on the activity of the P25 TiO_2 catalyst was verified by the enhanced reaction rate increasing from 0.17 to 0.20 mmol $L^{-1}min^{-1}$ compared to the P25 TiO_2 catalyst.

3.5   Sulfation of TiO_2 catalysts

As shown in section 1.3.2, type and concentration of the sulfating agent determined the strength and distribution of the acid sites, resulting in different catalytic activities. Sulfation of TiO_2 had showed an improved catalytic activity in the synthesis of 4,N-diphenylbutyramide. To explore the optimal sulfation conditions, the effect of several parameters included in the sulfation process was studied.

3.5.1 Sulfate precursors

Ammonia sulfate and sulfuric acid were the common alternatives to provide the sulfate functional group. The effect of sulfate precursors on catalytic activity was compared in reaction between 4-phenylbutyric acid and aniline. The amide yield as a function of time is shown in Figure 3.8. It can be seen that the sulfuric acid treated P25-38.4S catalyst demonstrated a higher reaction rate than P25 TiO$_2$ catalyst, which confirmed the positive effect of the presence of sulfate groups on the catalyst surface. To the opposite, the sulfation by ammonia sulfate (P25-38.4AS) suppressed the catalytic activity, resulting in a lower product yield. The sulfation by ammonia sulfate enhanced both Lewis and Brønsted acid sites while sulfuric acid only affected the Lewis acid sites [43]. Therefore a lower activity of the P25-38.4AS catalyst might be attributed to the increased number of Brønsted acid sites on the surface. The result suggested that sulfuric acid was superior to ammonia sulfate when considered as the sulfate precursor to modify P25 catalyst in this reaction.

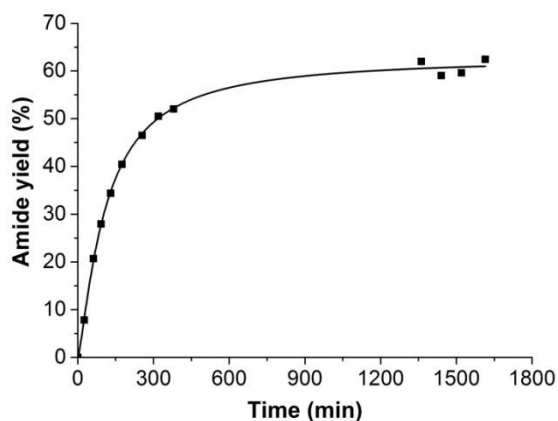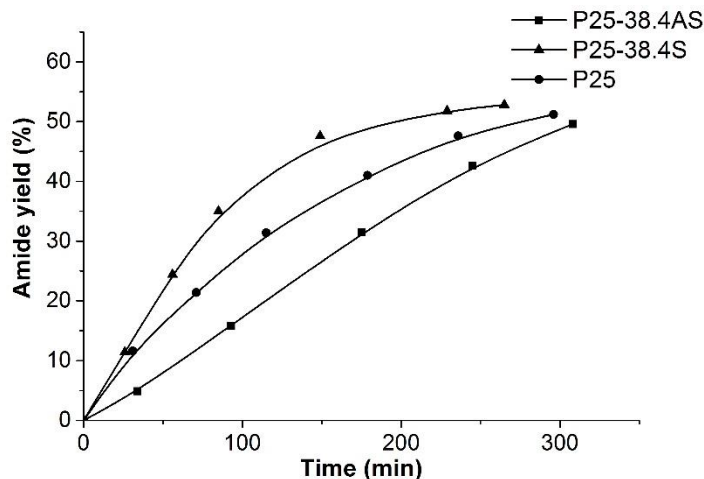Figure 3.8 Amide yield as a function of time over P25 TiO$_2$ catalysts sulfated by sulfuric acid and ammonium sulfate in the batch reactor. Reaction conditions: 50 mmol/L 4-phenylbutyric acid and 50 mmol/L aniline in 100 mL p-xylene, 165 mg catalyst, 200 °C, 10 bars.

3.5.2 Identification of sulfation method

The distribution of sulfate groups on the catalyst was firstly identified by EDS. It can be seen from elemental map that sulfur element was detected and

53

distributed evenly on the surface, indicating the successful doping of sulfate group by the method used.
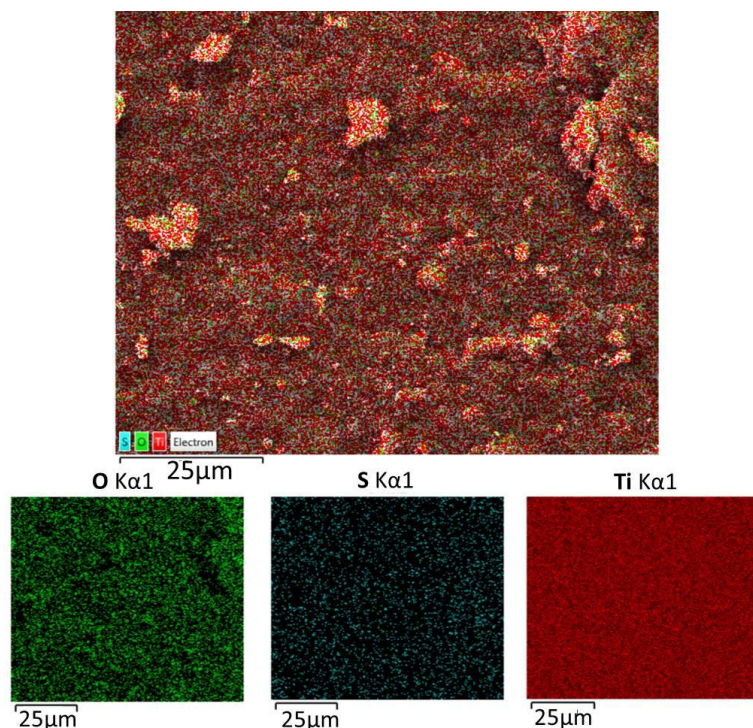
Figure 3.9 Elemental maps of P25-38.4S catalyst detected by EDS.

In the next step, the properties of the sulfated P25 TiO$_2$ catalyst after the sulfation treatment were compared with those of initial P25 TiO$_2$ catalyst. XRD pattern (Figure 3.10) showed the existence of both anatase and rutile TiO$_2$ in the P25 TiO$_2$. The peaks locating at 25.0, 36.6, 37.4, 38.2, 47.6, 54.8, 62.7 °2θ indicated the existence of anatase phase (JCPDS card no. 71-1169). The rutile phase was verified by the peaks at 27.1, 35.7, 40.8, 43.5, 54.0, 56.4 °2θ (JCPDS card no. 76-0320). Compared to the pattern of P25 TiO$_2$, the phase composition did not change after sulfation. The crystal size was calculated according to the main peaks at 25.0 and 27.1 °2θ for anatase and rutile phase respectively by using Scherrer equation (Eq. (3.5)).

$$D_C = \frac{K\lambda}{\beta \cos\theta} \tag{3.5}$$

where D_c is the crystalline size, K is the shape factor ($K= 0.89$), λ is the X-ray wavelength, β is the broadening at half the maximum intensity, and θ is the Bragg angle.

The crystal sizes of both phases remained virtually the same after the treatment, indicating no phase transformation occurred at the calcination temperature of 400 °C. The surface area increased from 50.5 to 53.5 m^2/g, showing a small change on morphology of the catalyst possibly due to an additional calcination step (Table 3.3).

Table 3.3 Physical properties of P25 TiO_2 and sulfated P25 TiO_2 catalysts

	Crystal size of anatase (nm)	Crystal size of rutile (nm)	Surface area (m^2/g)
P25	21.6	39.3	50.5
P25-38.4S	22.3	37.8	53.5
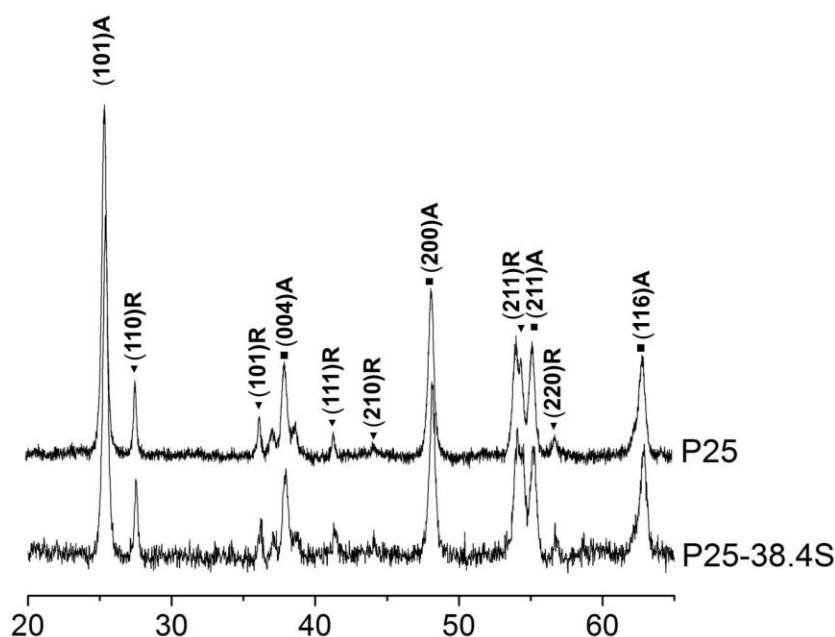
Figure 3.10 XRD patterns of titania (P25) and sulfated titania (P25-38.4S). The peaks are assigned as (A) anatase, (R) rutile

In conclusion, the P25 TiO_2 could be successfully functionalized by sulfate groups without significant change on its phase composition, crystallinity, and surface area, showing the parameters such as mixing time with sulfuric acid, calcination temperature were suitable to be further used.

3.5.3 Catalysts with different sulfate loadings

A small amount of sulfate groups added in the catalysts was proved to affect the catalytic activity significantly [37, 41, 42]. To explore the optimal loading of sulfate groups onto TiO_2 for direct amide synthesis, the initial mass ratio of SO_4^{2-}/TiO_2 added in water was varied from 1.0 to 38.4 wt.%, forming the sulfated titania catalysts with different degrees of sulfation. The electronic state of the elements on the surface would be changed according to the mechanism shown in section 1.3.2. In order to study this effect, the electronic state of the elements in the sulfated P25 TiO_2 were analysed by XPS and a spectrum of P25 TiO_2 is presented for comparison (Figure 3.11). The XPS spectra showed the strong peaks representing Ti and O in all samples, and peak standing for S appearing in the sulfated samples indicated the successful sulfation of TiO_2, which was coincident with the data of EDS. In the P25 TiO_2 catalyst, the spin-orbital doublet was observed at 458.2 and 464.0 eV corresponding to Ti $2p_{3/2}$ and Ti $2p_{1/2}$ respectively. The position of the Ti $2p_{3/2}$ peak confirmed the electronic state of Ti^{4+}. After sulfation, the binding energy up-shifted revealing Ti cation became more positively charged, which was due to the strong interaction between the SO_4^{2-} ions and the Ti cation (Figure 3.11 (a) (b)). The binding energy of S $2p_{3/2}$ in the range from 168.4 to 168.7 eV confirmed sulfur was in the S^{4+} oxidation state, verifying the S-O-Ti bond on the surface. A small S $2p_{1/2}$ peak observed at 169.5 eV indicated the existence of S^{6+} chemical state, which was due to the residue free sulfate ions on the surface [171] (Figure 3.11 (c)). The binding energy of the sulfur atom decreased from P25-1S to P25-38.4S catalysts, demonstrating the electron density of the sulfur atom increased with the sulfate content. This shows that the interaction between sulfate groups and Ti^{4+} was stronger as sulfate groups increased. The peak of O 1s at 529.7 eV in the pattern of P25 TiO_2 corresponded to oxygen atoms in the O-Ti bonds. There was also a shoulder observed at 531.5 eV, which was related to the oxygen atom in the chemical adsorbed moisture. In the spectra of sulfated TiO_2, the peak of O 1s was shifted to a higher binding energy, demonstrating lower electron density on the oxygen atom in the S-O-Ti bridge [39, 172, 173] (Figure 3.11 (d)).

The elemental composition was calculated from the peak areas and it provided a relative quantity of each compound (Figure 3.11 (e)). The actual sulfate content was proportional to the amount of sulfate added in the synthesis process when the ratio was below 10 wt.%. With addition of sulfate groups above a 10 wt.% loading, the Ti atoms became more positively charged, thus it was difficult to form new bond between the Ti atom and free sulfate groups. Even though more sulfate groups were added, the rate of forming new Ti-SO_4^{2-} bond on the surface decreased. This phenomenon was verified by the slower slop shown in the relationship between actual and theoretical value SO_4^{2-}/TiO_2 after a 10 wt.% loading.

(a)

(b)

(c)

(d)
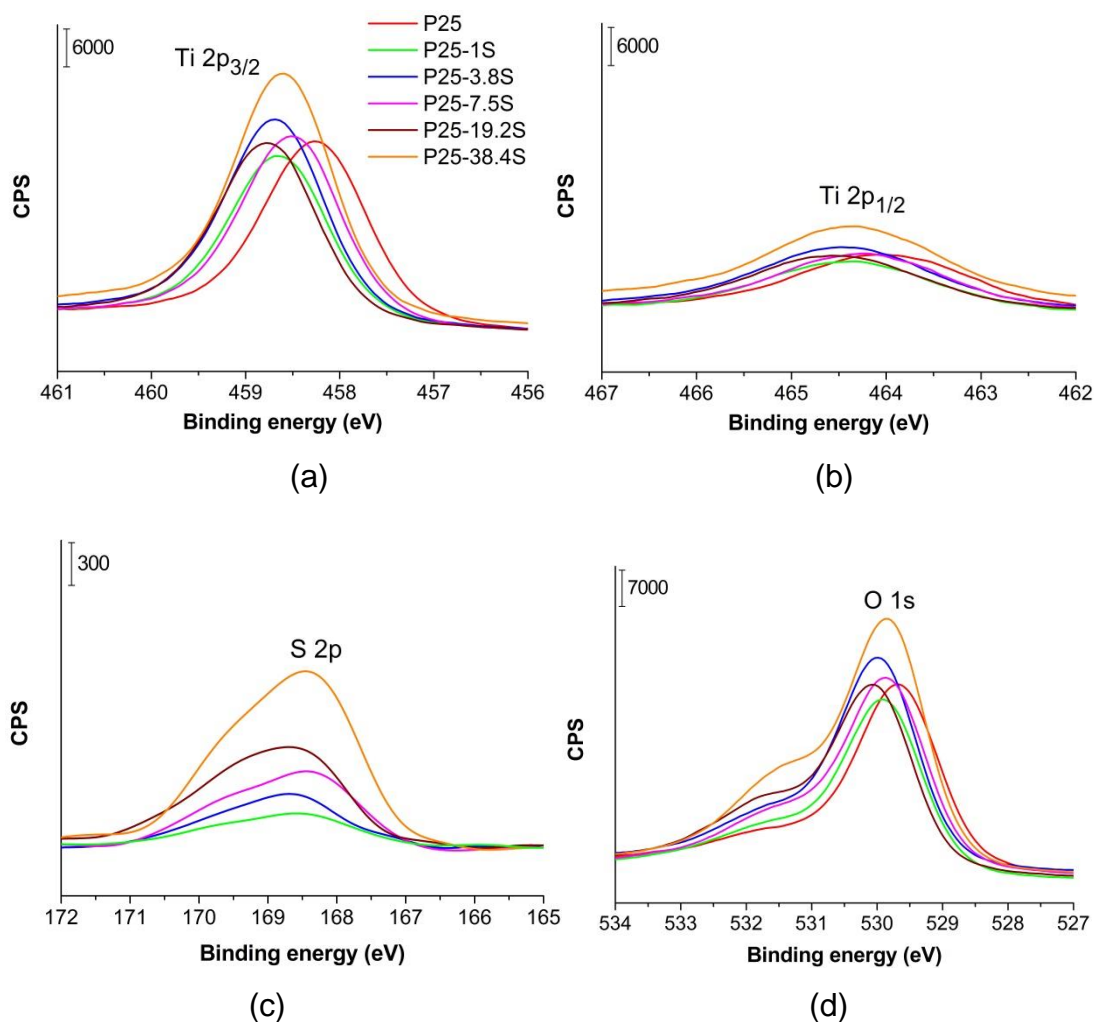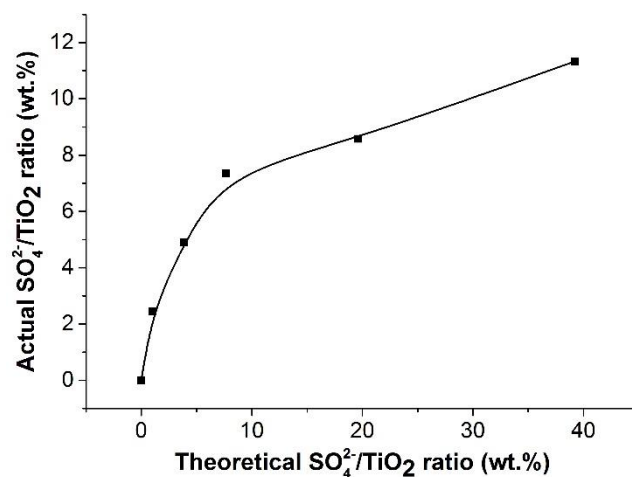
(e)

Figure 3.11 XPS analysis of sulfated P25 with various sulfate contents (a) Ti $2p_{3/2}$ peak (b) Ti $2p_{1/2}$ peak (c) S 2p peak (d) O 1s peak (e) Relationship between nominal and experimental values of SO_4^{2-}/TiO_2 weight fraction

The change of acid sites after the sulfation treatment was identified by pyridine adsorption studied with FT-IR (Figure 3.12). The peaks at 1445, 1574 and 1604 cm^{-1} were attributed to the interaction between pyridine and Lewis acid sites [48], and the peak at 1490 cm^{-1} was assigned to both Brønsted and Lewis acid sites [174]. There was no peak showing up around 1540 cm^{-1}, indicating the absence of Brønsted acid sites [37, 43, 175]. It can be concluded that Lewis acid sites were the main acid types existing on the surface of the sulfated TiO_2 catalyst. All the peak intensities of sulfated catalysts were higher than those of pure P25 TiO_2, showing the growth of Lewis acid sites after sulfation. The sulfated catalyst had an additional band at 1297 cm^{-1} due to the vibration of S=O [176], which proved the existence of sulfate group from another aspect. Particularly, the peak of S=O shifted from 1266 to 1303 cm^{-1} as temperature increased. This was due to the interaction between pyridine and the S=O groups modifying the electronic density. Even though pyridine desorbed at high temperature, their covalent character still affected the state of S=O, resulting in the shift of the vibration to higher wavelength [177]. To compare the variation of Lewis acid strength in the P25-XS catalysts, the peak area at 1445 cm^{-1} in the spectra of the same sample taken at different temperatures was normalized. It can be seen from Figure 3.12 (b) that the peak area of the samples with higher sulfate content

decreased slower with temperature, indicating the formation of more stronger acid sites when more sulfuric acid were used in the synthesis process.
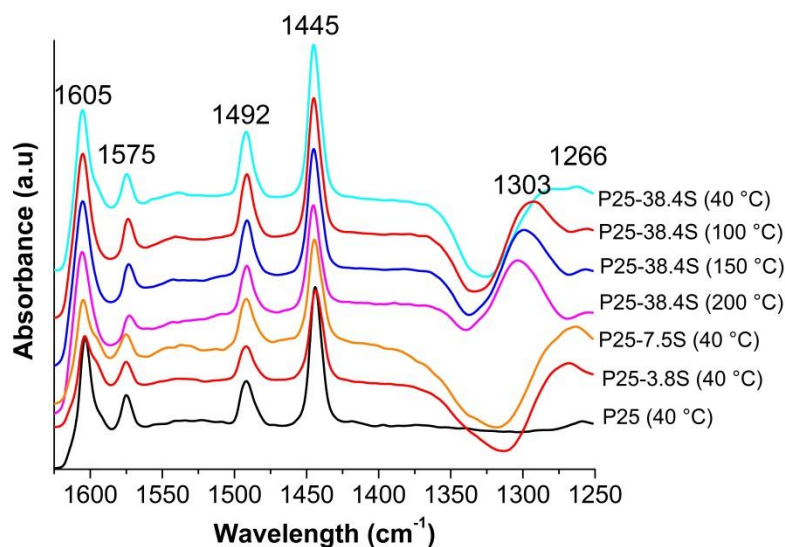
(a)
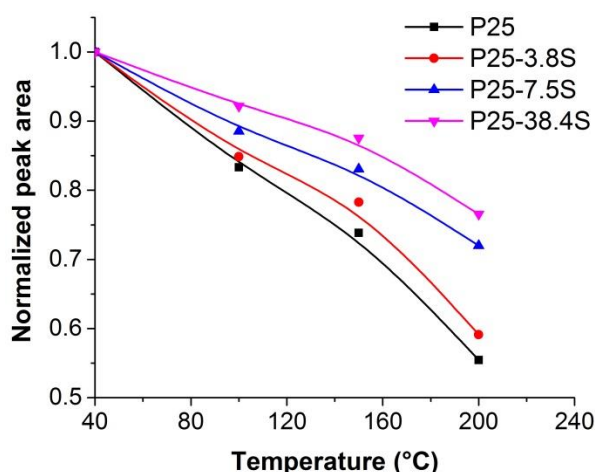
(b)

Figure 3.12 (a) FT-IR spectra of adsorbed pyridine over P25 TiO_2 and P25-XS catalysts recorded at different temperatures (b) Normalized peak area at 1445 cm^{-1} in the spectra recorded at different temperatures

To test the activity of the sulfated catalysts, the reaction was conducted in the batch reactor catalysed by various sulfated catalysts. As this can be regarded as a second order reaction in the initial period, the rate constant was calculated to compare the catalytic activity of each catalyst. According to Figure 3.13, the value of reaction rate constant increased sharply over three-fold as the nominal SO_4^{2-}/TiO_2 ratio increased from 0 to 7.5 wt.%. It is worthy

pointing out that even sulfation with 1 wt.% of SO_4^{2-}/TiO_2 could have a significant improvement on reaction rate constant compared to the initial P25 TiO_2. This demonstrates the bond between the Ti atoms and the SO_4^{2-} groups can be easily formed even in a quite diluted solution of sulfuric acid. After 7.5 wt.%, the rate constant however showed the slight decrease, making P25-7.5S the optimal catalyst. As the strength of the acid sites was found to increase with the sulfate content, the decrease of the rate constant for catalysts with higher sulfation content might be due to the over-strong adsorption of chemicals on the surface, resulting in the slow reaction rate. Thus it can be deduced that the strength of acid sites on the surface of P25-7.5S was most suitable for activation of 4-phenylbutyric acid (Figure 1.2).
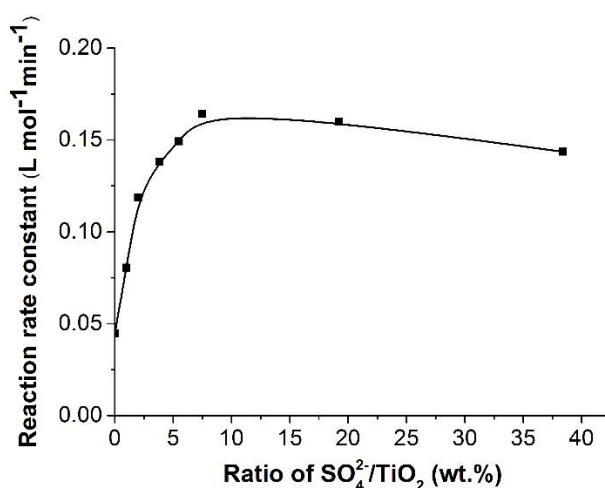
Figure 3.13 Reaction rate constant as a function of nominal weight ratio of SO_4^{2-}/TiO_2. Reaction conditions: 50 mmol/L 4-phenylbutyric acid and 50 mmol/L aniline in 100 mL p-xylene, 165 mg catalyst, 200 °C, 6 bars.

3.6   Additional treatments of TiO_2 catalysts

3.6.1 UV treatment

It is well known that the electronic state of TiO_2 can be changed by UV light. When it is irradiated by UV light, if the energy is high enough for electrons to go across the band-gap, a positive hole will be left by the excited electrons, forming the stronger active sites for certain reagents to react [178, 179]. However, if it is not exposed under UV light continuously, the effect of UV

illumination was found out to fade with the time [180, 181]. Also, TiO_2 after illumination could interact with water, resulting in the transformation of the Lewis acid sites on the surface into Brønsted acid sites [34]. In the same process, OH and O^{2-} were produced from water which can decompose organic molecules [182]. If UV treated TiO_2 catalyst is directly used in the amide synthesis, the UV treatment will cause the instability of the catalysts during stream time, as the amount of active Lewis acid sites will decrease in the presence of water which is a reaction by-product. Nevertheless, the UV activated surface was used to induce more sulfate groups in the sulfation process and change the acid sites distribution.
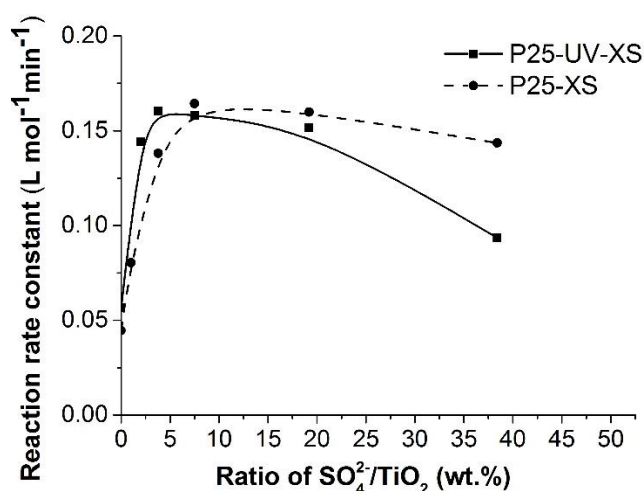
Figure 3.14 Reaction rate constant as a function of nominal weight ratio of SO_4^{2-}/TiO_2 after UV treatment. The curve for the P25-XS catalysts is shown for comparison. Reaction conditions: 50 mmol/L 4-phenylbutyric acid and 50 mmol/L aniline in 100 mL p-xylene, 165 mg catalyst, 200 °C, 6 bars.

To explore the effect of UV treatment on sulfation, the P25 TiO_2 catalyst was irradiated by UV light before the sulfation treatment and they catalysed the amide reaction in the batch. The reaction rate constant at 200 °C showed a similar dependence to that without UV treatment while the same catalytic activities were observed at lower SO_4^{2-} loadings. The optimum loading shifted from 7.5 to 3.8 wt.% while the corresponding reaction rate constants were nearly the same. This indicates that after UV treatment less sulfuric acid is needed to achieve the same reaction rate. It can be deduced that UV irradiation made the Ti sites more positively charged, thus being easier to

bond with the sulfate groups (Figure 3.14). To summarize, the UV treatment could help to reduce the amount of acid required for sulfation.

3.6.2 Silicate treatment

As there exist both Lewis and Brønsted acid sites on the surface of TiO_2 in the present of water, there is possibility that weak Brønsted acid sites which donated proton might affect the bonding between neighbouring Lewis acid sites and sulfate groups. To study the effect, a proper way should be found out to diminish the concentration of the Brønsted acid sites. According to the literature, silicate compound could replace OH group, resulting in a very low concentration of hydroxyl groups on the surface [183, 184]. Following this idea, the P25-7.5S catalyst was treated by a sodium silicate solution and then calcined. As calcination could result in the condensation and formation of siloxane groups [183], a silicate treated sample without calcination (Si-P25-7.5S) was also studied.
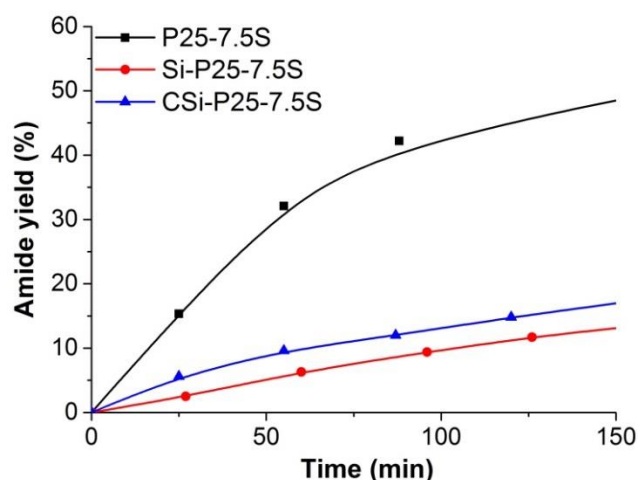
Figure 3.15 Amide yield as a function of time over uncalcined (Si-P25-7.5S) and calcined silicate treated sulfated catalyst (CSi-P25-7.5S). Reaction conditions: 50 mmol/L 4-phenylbutyric acid and aniline (100 mL), 165 mg catalyst, 200 °C, 6 bars.

The silicate treated catalysts were dispersed in the aqueous solution and it was hard to centrifuge them into the bottom, showing the obvious hydrophobic property. The catalytic activities of the silicate treated catalysts are shown in Figure 3.15 and the amide yield curve of P25-7.5S is presented as reference. It shows that catalytic activity of P25-7.5S was drastically

reduced after the silicate treatment, indicating the hydrophobic surface area was not good for the amide formation. A similar effect was also observed by Pazokifard et al. [185]. They showed that the electronic state of silca grafted P25 TiO_2 shifted towards the similar electron state in the rutile TiO_2 and silica, leading to a reduced photocatalytic activity. The calcined catalyst Si-P25-7.5S behaved slightly better than the uncalcined one. For the uncalcined but dried sodium silicate, it was hydrated Na_2SiO_3 with chemisorbed water while it turned into anhydrous Na_2SiO_3 after calcination [186]. It was possibly due to the release of water strengthening the Brønsted acid sites when uncalcined silicate treated catalyst was used.

3.6.3 TiO_2 mixing with water absorbents

As the existence of water in the reaction mixture was reported to affect the activity of titania catalyst [167, 169, 170], to study the catalyst tolerance to water, an extra 500 µL (28 mmol) water was added into the initial reactant mixture. Catalysed by the same catalyst under fixed reaction conditions, the amide yield curves with and without water added are shown in Figure 3.16. The reaction rate decreased by 30% when water was added. This result demonstrates that the activity of this titania catalyst is affected when exposed to the water phase, and removing water could help to accelerate the reaction rates.
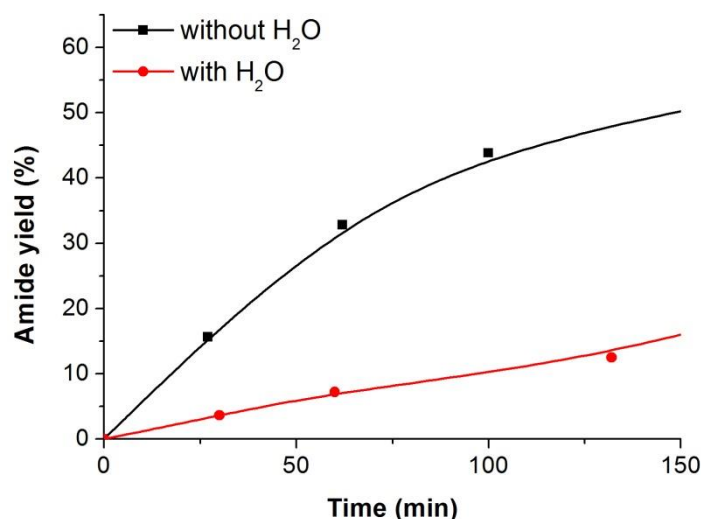
Figure 3.16 Amide yield as a function of time in reactions with or without water. Reaction conditions: 50 mmol/L 4-phenylbutyric acid and 50 mmol/L aniline in 100 mL p-xylene, 165 mg catalyst (UV-P25-7.5S), 200 °C, 6 bars.

To get rid of water in the reactor, material which can absorb water was considered to be added into the reactant solution together with the catalysts. Molecular sieves (MS) as the most common absorbent material can absorb water up to 22 wt.% of its mass. Another material chosen was poly(acrylic acid sodium salt) (PAASS), which is a super water absorbent polymer and can absorb mass of water 200 to 300 times over its own weight. In the following experiments, 0.5 g 4 Å MS and PAASS (Sigma Aldrich) were added separately with 0.165 g P25-7.5S to perform the reaction between 4-phenylbutyric acid and aniline. Nevertheless, amide yields in the present of the absorbent materials were in contrary much lower than that in the experiment with pure catalyst (Figure 3.17). Experiment with PAASS which was supposed to absorb more water actually resulted in an even lower yield than the one with MS. This result was possibly caused by a strong interaction between the reactants and absorbent material. The component of 4 Å MS used was $H_xNa_{12-x}[(AlO_2)_{12}(SiO_2)_{12}] \cdot mH_2O$ which may contain stronger acid sites and therefore may hold the phenylbutyric acid on its surface. For PAASS, the carboxylate in the polymer chain might react with aniline and then reduce the concentration of the amine in the solution. In conclusion, besides removing water, the water absorbent itself affected the reaction negatively and this side effect was over the contribution of removing water.

With the development of absorbent materials, there is still a possibility to have the water absorbent with reactant-inert components.
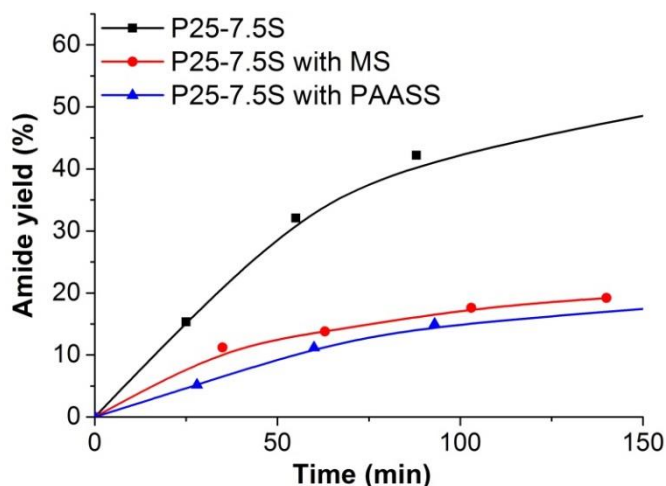
Figure 3.17 Amide yield as a function of time in batch reactor with 0.5 g water absorbent. Reaction conditions: 50 mmol/L 4-phenylbutyric acid and 50 mmol/L aniline in100 mL p-xylene, 165 mg P25-7.5S catalyst with 0.5 g absorbent, 200 °C, 6 bars.

3.7 Catalytic activity in batch and conventionally heated continuous reactors

3.7.1 Direct amide synthesis catalysed by the optimal catalyst in the batch reactor

The effect of reaction temperature on the reaction rate of direct amide synthesis reaction over the P25-7.5S catalyst was studied in the batch reactor in the range from 130 to 170 °C. The reaction rate constant at each temperature was calculated from the second order reaction kinetics (Eq. (3.3)). The reaction rate constant increased sharply from 0.013, 0.029 to 0.076 L $mol^{-1}min^{-1}$ corresponding to the temperatures at 130, 150 and 170 °C respectively. The activation energy of the reaction over the P25-7.5S catalyst was calculated according to the Arrhenius equation (Eq. (3.6)). The value calculated from the linear curve shown in Figure 3.18 was 66 kJ/mol.

$$ln(\frac{k_1}{k_2}) = \frac{E_a}{R}(\frac{1}{T_2} - \frac{1}{T_1})$$

(3.6)

where k is the reaction rate constant, E_a is the activation energy, T is the reaction temperature, R is the ideal gas constant of 8.31 J/(mol·K).
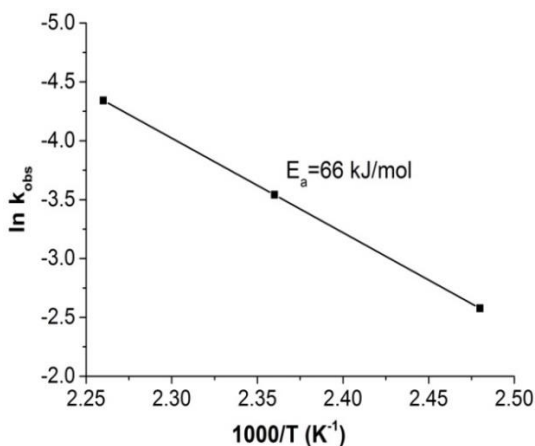
Figure 3.18 Arrhenius plot of the reaction rate constant. Reaction conditions: 50 mmol/L 4-phenylbutyric acid and 50 mmol/L aniline in 100 mL p-xylene, 165 mg P25-7.5S catalyst, 6 bars.

According to the mechanism, the acid is the main reactant activated by the catalyst. To extend the range of possible applications, two other acids having the similar pKa values as 4-phenylbutyric acid namely acetic acid and propionic acid with aniline were also catalysed by P25-7.5S in the batch mode (Table 3.4). The acetic acid and propionic acid with aniline showed higher reaction rates than 4-phenylbutyric acid, which were 0.74 and 0.85 µmol (g-TiO$_2$) $^{-1}$ s^{-1} respectively. As the activity of the acids to react with aniline were similar according to the pKa value, the faster reaction rates of acetic and propionic acids might be due to the smaller molecules of the reactants which led to the faster mass transfer. It can be concluded that this sulfated TiO$_2$ has a good catalytic activity on amidation of 4.7 – 4.9 pKa acids with aniline. As both of the acids in this pKa range and aniline were inactive to react, it can be deduced that the sulfated TiO$_2$ will also show the good catalytic activity on direct amidation of more active acids and amines. Besides direct amide synthesis, the good performance of sulfated TiO$_2$ was also proved in other organic synthesis as well (see section 1.3.3), demonstrating other potential application areas of P25-7.5S.

Table 3.4 pKa values of various acids and corresponding reaction rates in the batch rector. Reaction conditions: 50 mmol/L acids and 50 mmol/L aniline in 100 mL p-xylene, 165 mg P25-7.5S catalyst, 6 bars.

Substrate	pKa	Reaction rate ($\mu mol\ g^{-1}\ s^{-1}$)
4-phenylbutyric acid	4.76	0.50
Propionic acid	4.86	0.74
Acetic acid	4.76	0.85

3.7.2 Catalytic activity of the optimal catalyst in the conventionally heated continuous reactor

A packed bed conventionally heated continuous reactor was used to study the effect of temperature on reaction rate in the continuous mode as well as the deactivation kinetics over P25-7.5S catalyst. The temperature of the catalyst bed was fixed at the same values as those in the batch reactor, namely 130, 150 to 170 °C. To compare the productivity of the batch and continuous reactors, the production rate of the whole catalytic bed is presented as the ratio of moles of the amide at the outlet to the mass of the catalyst contained in the reactor.

The initial rate constant k was calculated from the Eq (3.4) using the input and output concentration of the reactants before catalyst deactivation. The inhibition constant was assumed to be the same for the reaction model catalysed by titania catalysts. The residence time for the heterogeneous catalyst bed was the ratio of liquid volume in the catalytic bed to the volumetric flow rate (Eq (3.7)). The corresponding concentration profiles along the catalytic bed are presented in the Appendix C.

$$\tau = \frac{(1-\varepsilon_p) \cdot \pi r_1^2 \cdot L_c}{F} \tag{3.7}$$

Where ε_p is the bed porosity, r_1 is the inner radius of the continuous reactor, L_c is the length of the catalytic bed, F is the volumetric flow rate.

The initial production rates normalized by the mass of catalyst and the initial rate constants in the batch reactor and CH-CR are compared in Figure 3.19. The rate constants observed in the CH-CR were two orders of magnitude higher than those in the batch due to the high catalyst loading in the continuous reactor. As the temperature increased from 130 to 170 °C, the production rate increased from 0.15 to 0.22 µmol g^{-1}s^{-1} in the CH-CR while the value in the batch reactor showed a much sharper increase from 0.19 to 1.02 µmol g^{-1}s^{-1}. The production rates in the batch reactor were higher than those in the CH-CR in the whole range of temperatures studied. This was possibly due to the presence of external mass transfer limitations in the continuous reactor. The smaller effect of temperature on production rate in the flow reactor was also attributed to the mass transfer limitation.
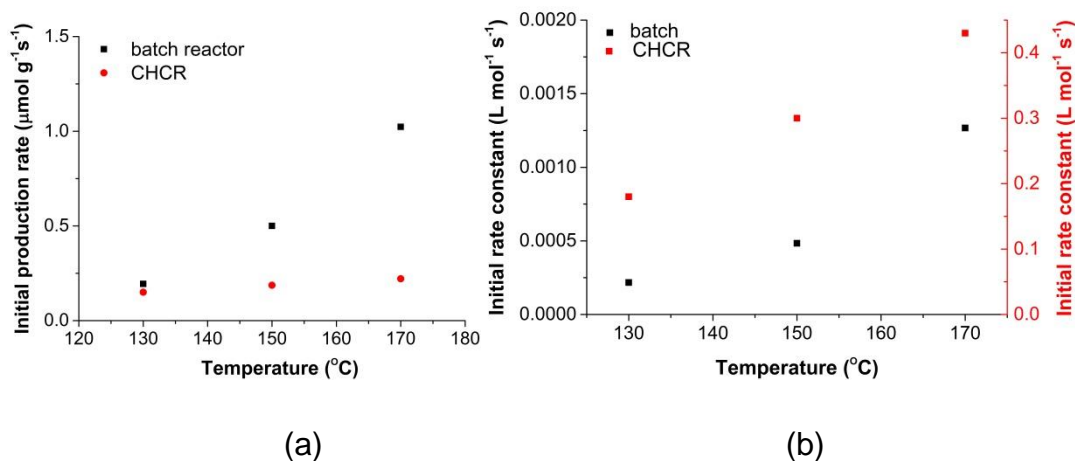
Figure 3.19 (a) Production rates (b) initial rate constants at 130, 150, 170 °C in the batch reactor and conventionally heated continuous reactor

Catalyst deactivation was observed in all the experiments in the CH-CR. The deactivation extent changed with the reaction temperature. The higher reaction temperature accelerated the rate of deactivation (Figure 3.20). The catalytic activity at 170 °C dropped by 25 % after 800 min while at 130 °C only by 5% of the initial catalytic activity was lost. The colour of the product mixture was observed to change in the course of reaction from transparent to yellow, dark yellow and finally brown at high reaction temperature, indicating the deactivation was caused by the decomposition and/or carbonization of the organic compound. Thus a balance between production rate and extent

of deactivation extent should be considered when choosing the proper reaction temperature.
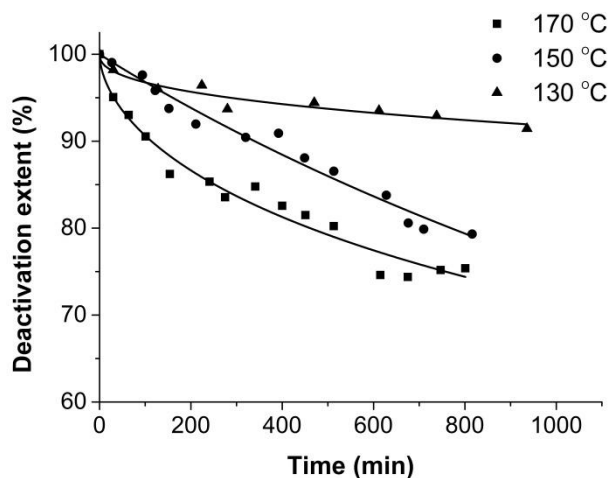
Figure 3.20 Deactivation extent as a function of time in conventionally heated continuous reactor with a 10 mm catalytic bed. Reaction conditions: 425 mg P25-7.5S catalyst (125-250 µm), 228 µL/min flow rate, 7 bars.

3.8   Conclusions

In summary, a series of modified P25 TiO_2 catalysts demonstrated high catalytic activity in the direct synthesis of 4, N-diphenylbutynamide. The catalytic activity was increased after a sulfation treatment with sulfuric acid due to the increased positive charge of Ti cations bonded with sulfate groups. The formation of Lewis acid sites was observed after the sulfation treatment. The number of the strong acid sites on the titania surface increased proportionally to the concentration of the sulfuric acid in the sulfation process. Over the catalyst with a numerical SO_4^{2-}/TiO_2 ratio of 7.5 wt.%, a 4-fold increase in catalytic activity was observed as compared to the commercial P25 TiO_2 catalyst. The activation energy of reaction catalysed by P25-7.5S was 66 kJ/mol. Moreover, the production rates per gram of the titania in the conventionally heated flow reactor were lower than those in the batch reactor under the same reaction condition due to the insufficient heat and mass transfer in the conventionally heated flow reactor. Deactivation of the catalyst was observed in the conventionally heated flow reactor and higher reacting temperature resulted in a faster deactivation.

Chapter 4

Mechanochemical synthesis of TiO$_2$/NiFe$_2$O$_4$ catalysts for direct amide synthesis under RF heating

4.1 Introduction

To apply the optimal sulfated TiO$_2$ catalyst in the RF-heated flow reactor, a method to combine the catalyst and magnetic material together should be explored. Both the catalytic activity of the initial catalyst and the magnetic property of the magnetic material should be maintained after the combination. Mechanochemical synthesis, which uses high power forced ball mill to grind and combine the magnetic and catalytic particles, is one of the options to make the desired magnetic catalysts. Compared to the sol-gel method, the process is much simpler and no other solvents or surfactants need to be added, making it easier to produce the magnetic catalysts on a large scale. Houlding et al. ever studied the effect of ball milling time on the synthesis of CMCs [1], showing that the magnetism of CMCs decreased with the milling time and 0.5 h was the minimum time to synthesize the uniform CMCs. To further optimize the ball milled CMC applied in the RF-heated reactor, TiO$_2$ content which affects both the catalytic and magnetic properties of CMC needs to be explored. The catalytic activity in the RF-heated continuous reactor, mechanism of deactivation and regeneration method should be further studied as well.

In this chapter, CMCs with different TiO$_2$ contents were synthesized by ball milling the mixture of NiFe$_2$O$_4$ and sulfated TiO$_2$ (P25-7.5S) catalyst. The obtained CMCs (T2 CMCs) were characterized by N$_2$ adsorption/desorption isotherms, XRD, SEM, VSM. To study the effect of TiO$_2$/NiFe$_2$O$_4$ weight fraction on the catalytic activity and deactivation, the catalytic activities of

CMCs with different TiO_2 loadings were measured in the RF-CR with a single packed bed. As deactivation occurred in all the experiments, deactivation mechanism and regeneration method were also explored to recover the spent CMCs.

4.2 Characterization of ball milled magnetic catalysts

The CMCs with the sulfated TiO_2 (P25-7.5S) loading varying from 33 to 50 wt.% were synthesized at 300 rpm speed for 0.5 h by ball mill. Before ball mill the catalyst and magnetic particles could be distinguished by their white and brown colours, while they became uniform dark brown powders after ball mill. The particular combination could be seen from the TEM image shown in Figure 4.1. The two components were coalesced and welded into each other instead of sticking together as two separate fine particles. The uniformity was verified by SEM-EDS as well (Figure 4.2). The element of Ni, Fe and Ti, S dispersed evenly, indicating P25-7.5S and $NiFe_2O_4$ were finely combined.
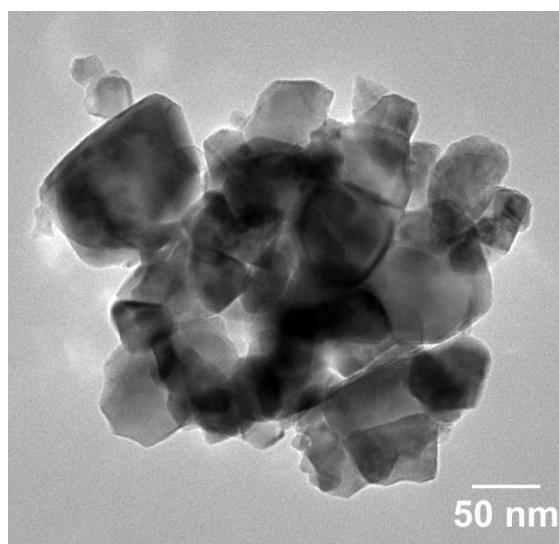
Figure 4.1 TEM image of the ball milled CMC (T2-33)
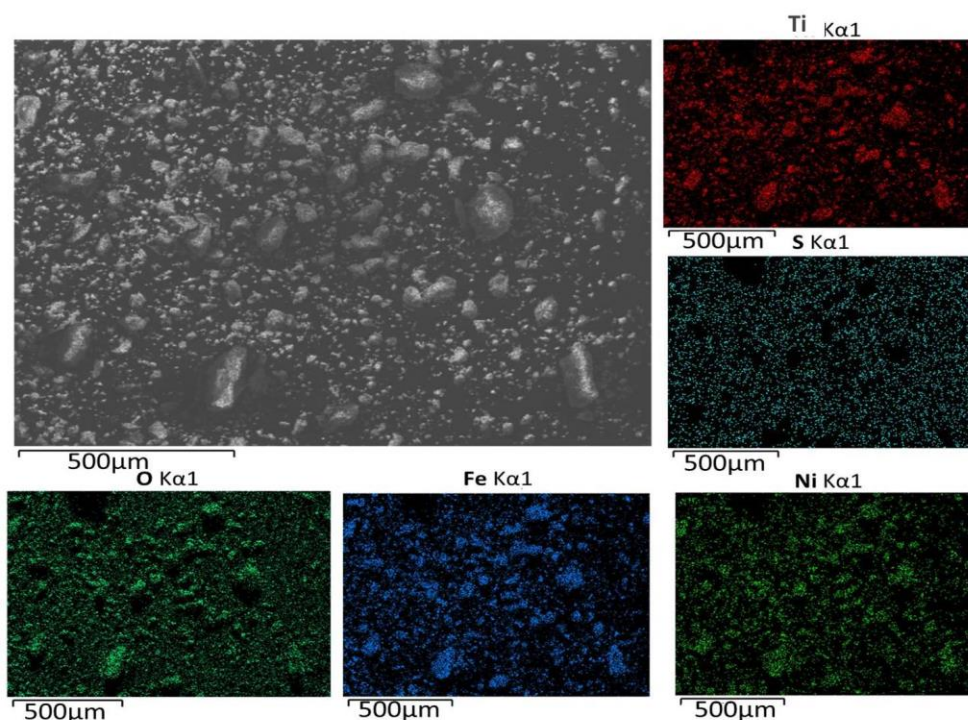
Figure 4.2 SEM image and the element map of the ball milled CMC (T2-33)

As ball mill can induce the chemical reaction between two compounds, both the catalytic activity of the sulfated TiO_2 and the magnetic property of $NiFe_2O_4$ cannot be maintained at the initial values once the new phase is formed. To identify the milling condition used, crystal form of synthesized CMCs was analysed by XRD. Patterns of ball milled CMCs with TiO_2 loadings varying from 33 to 50 wt.% are shown in Figure 4.3 and those of P25-7.5S and $NiFe_2O_4$ are presented as the references. The XRD peaks at 25.4, 48.2 and 64.9 °2θ were attributed to the (101), (200), (211) crystal phases of anatase respectively (JCPDS card no. 78-2486). The peak at 32.1 °2θ was assigned to the (110) reflection of rutile. The peaks at 30.7, 36.0, 37.6, 43.8, 54.8, 58.1, and 64.4 °2θ were associated to the (220), (311), (222), (400), (422), (511) and (440) crystal planes of $NiFe_2O_4$ (JCPDS card no. 74-2081). There were also peaks showing up at 31.4 and 41.3 °2θ corresponding to the (220), (113) crystal planes of α-Fe_2O_3 (JCPDS card 33-0664), indicating the formation of a small amount of α-Fe_2O_3 during the synthesis of $NiFe_2O_4$. As TiO_2 content increased from 33 to 50 wt.%, the intensity of titania peaks gradually increase while that of $NiFe_2O_4$ and α-Fe_2O_3 decreased, which was coincident with the mass ratio of the TiO_2 content. By comparison with the reference peaks, it can be concluded that

although the obtained CMCs were uniform, there was no formation of new crystal phases during the mechanochemical synthesis of all the CMCs. It is also proved that variety of the titania loading did not have the effect on transformation of the crystals. In this way, ball mill using rotation speed of 300 rpm for 0.5 h could be applied for the synthesis of magnetic catalysts.
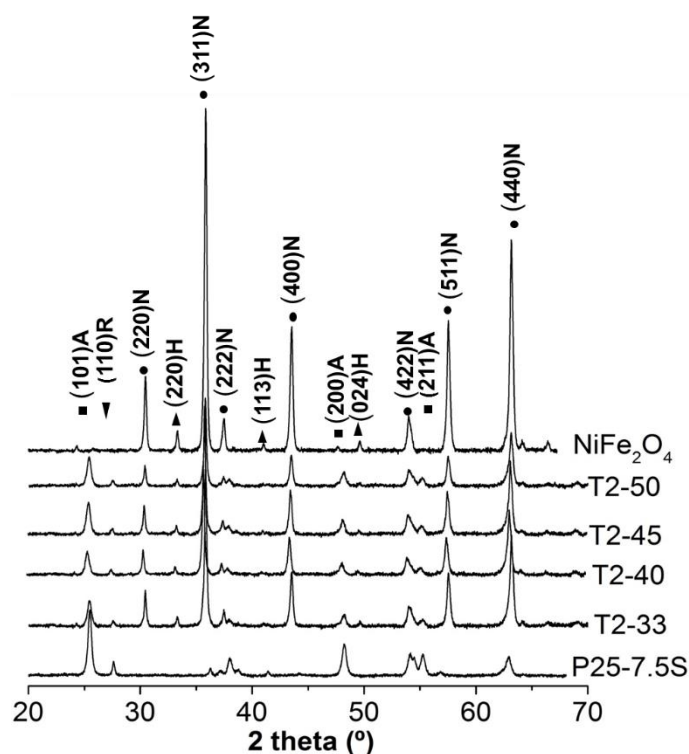
Figure 4.3 XRD patterns of ball milled CMCs with different titania loadings (33 – 50 wt.%), P25-7.5S catalyst and $NiFe_2O_4$. The peaks are assigned to (N) $NiFe_2O_4$, (A) anatase titania, (H) hematite Fe_2O_3.

The combination of two different compounds resulted in the change of several physical properties. On the aspect of surface area, the value of P25-7.5S as the catalytic part was $49.1 m^2 g^{-1}$ while that of $NiFe_2O_4$ was as low as 2.2 $m^2 g^{-1}$. With the increase of the titania loading, the surface area of T2 CMCs changed from 22.6 to 30.2 $m^2 g^{-1}$ (Table 4.1). According to the mass ratio of $NiFe_2O_4$ and P25-7.5S, the nominal surface area (S) varying with the weight fraction of titania (x) can be calculated using Eq. (4.1). The nominal and measured values of surface area were compared in Figure 4.4 (a).

$$S_{CMC} = S_{TiO_2} \cdot x + S_{NiFe_2O_4} \cdot (1-x) \tag{4.1}$$

According to Figure 4.4 (a), the measured surface area was higher than the nominal value, which was due to the much finer particles caused by milling.

(a)   (b)
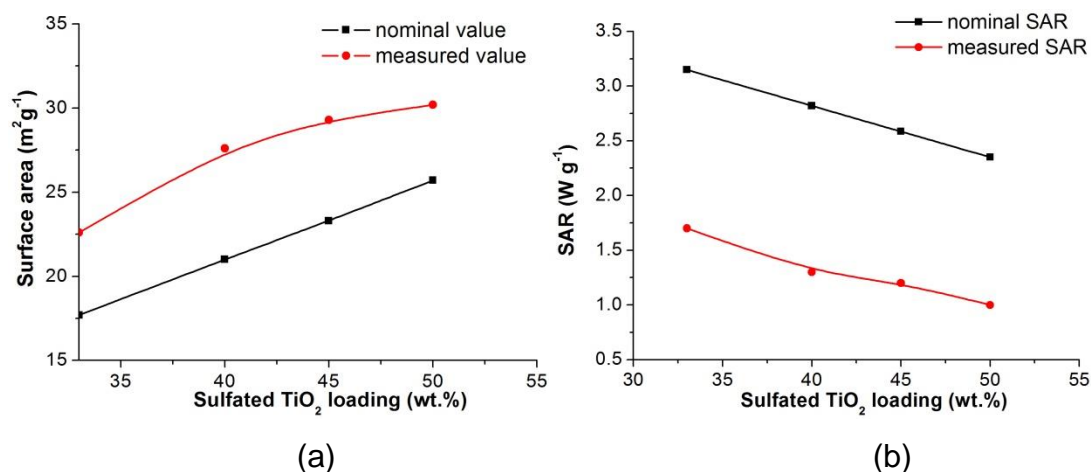
Figure 4.4 Nominal and measured values of (a) surface area and (b) SAR as a function of weight fraction of the sulfated TiO_2

On the aspect of heating property, specific absorption rate (SAR) of ball milled CMC was firstly measured. The SAR dropped from 1.7 to 1.0 W g^{-1} as more TiO_2 contained in the CMC (Table 4.1). Based on the SAR of $NiFe_2O_4$ at 4.7 W g^{-1}, the nominal values calculated using the similar equation to Eq. (4.1) were higher than the measured ones (Figure 4.4 (b)). This was caused by the addition of the sulfated TiO_2 catalysts which reduced mechanical fraction between magnetic particles [1]. The change of the magnetism was further tested by VSM. Different hysteresis loops of CMCs with various titania loadings are presented in Figure 4.5. Coercivity of each sample fluctuated in a rather small scale from 0.24 to 0.31 kG as titania content increased from 33 to 50 wt.%. However, the saturated magnetism dropped significantly from 32.0 to 17.9 emu g^{-1} with the increasing titania loading. For the ferromagnetic material, the main parameter of magnetism determining the heating property is the area of hysteresis loop [141]. As shown in Table 4.1, the hysteresis area of T2 CMC decreased from 0.12 to 0.06 J/g as the titania loading increased, which agreed with the trend of the SARs.
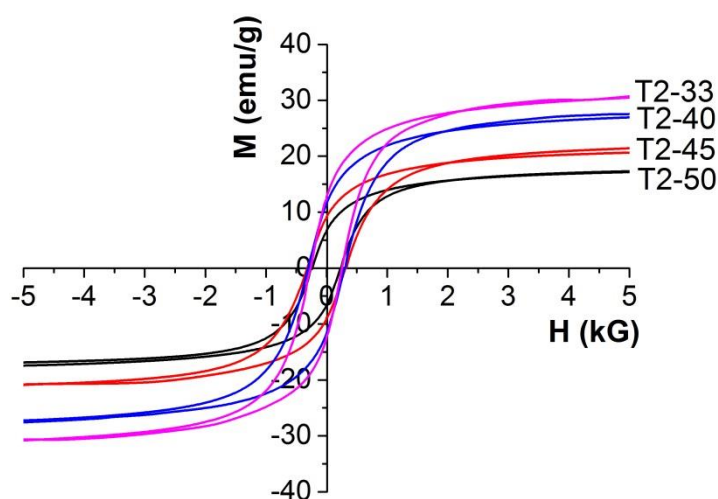
Figure 4.5 Hysteresis curves of ball milled CMCs with different titania loadings.

Table 4.1 Physical properties of P25-7.5S catalyst, $NiFe_2O_4$ and T2 CMCs with different titania loadings.

	Surface area (m^2/g)	SAR (W/g)	M_S (emu/g)	H_C (kG)	Hysteresis area (J/g)
$NiFe_2O_4$	2.2	4.7	n.d	n.d	n.d
P25-7.5S	49.1	-	-	-	-
T2-33	22.6	1.7	32.0	0.26	0.12
T2-40	27.6	1.3	28.1	0.30	0.10
T2-45	29.3	1.2	21.6	0.31	0.08
T2-50	30.2	1.0	17.9	0.24	0.06

n.d – not determined

4.3   Catalytic activities of ball milled magnetic catalysts

An RF-heated continuous reactor with a single catalytic bed packed with ball milled CMCs was set up as shown in Figure 4.6. Assumed a certain amount of P25-7.5S catalyst in the bed is required, the weight ratio of $TiO_2/NiFe_2O_4$ in the catalytic bed can be changed by packing ball milled CMCs with the different titania loadings. In this way, the weight of $NiFe_2O_4$ is varied in each catalytic bed. To reach the same reaction temperature, the heat produced per unit of $NiFe_2O_4$ should be higher in the packed bed containing less $NiFe_2O_4$, which may have the effect on both the catalytic activity and

deactivation. To study their catalytic activities in direct amide synthesis in the RF-CR, the reactor was packed with various ball milled CMCs and run at fixed reaction conditions. The total mass of sulfated TiO_2 was fixed at 260 mg in all the experiments. The specific amount of each T2 CMC used and corresponding lengths of the catalytic bed are listed in Table 4.2. In order to compare the catalytic activity of sulfated TiO_2 in the CH-CR and RF-CR, the weight hourly space velocity (WHSV) in the RF-CR was kept at 9 μL (g-TiO_2)$^{-1}$ s^{-1}, which was the same as that in the CH-CR. Thus the flow rate was determined at 142 μL/min. All the reaction temperature of the bed was kept at 150 °C by adjusting the current manually.
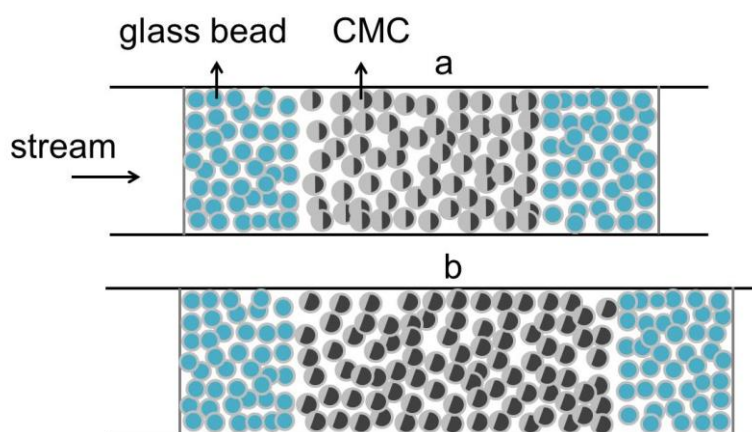
Figure 4.6 Schematic view of RF-heated continuous reactor packed with ball milled CMCs having (a) higher and (b) lower titania contents

Table 4.2 Reaction conditions for the RF-CR packed with different T2 CMCs

	CMC (mg)	Current (A)	Length of catalyst bed (mm)
T2-33	782	100.8	14
T2-40	653	113.6	12
T2-45	595	116.8	11
T2-50	526	121.6	10

As shown in Table 4.3, the initial rate constant and production rate normalized by the mass of CMC increased as the CMC having higher titania loading, which was under expectation. To compare the catalytic activity of P25-7.5S catalyst in each CMC, the production rates were then normalized

by the mass of TiO_2. The results are shown in Figure 4.7 and corresponding value of P25-7.5S catalyst in the CH-CR is presented as the reference. The production rates normalized by the amount of titania for T2 CMCs were nearly the same from 0.23 – 0.24 $\mu mol \cdot g\text{-}TiO_2^{-1} \cdot s^{-1}$, indicating the catalytic activity of P25-7.5S catalyst was not affected by the weight fraction in the CMC. The value in the CH-CR dropped by 17% to 0.19 $\mu mol \cdot g\text{-}TiO_2^{-1} \cdot s^{-1}$ as compared with that of the RF-CR. The lower value of the production rate in the CH-CR was due to lower temperature in the centre of the reactor as heat transferred from the wall. The better activity of the catalyst in T2 CMC indicated that the large temperature gradient on the cross section of the conventionally heated reactor could be diminished in RF-heated reactor.

Table 4.3 Production rates and initial rate constants of direct amide synthesis over T2 CMCs in RF-heated continuous reactor. Reaction conditions: 50 mmol/L 4-phenylbutyric acid and 50 mmol/L aniline, total flow rate 142 µL/min, 150 °C, 7 bars

	Initial rate constant ($L \cdot mol^{-1} \cdot s^{-1}$)	Initial production rate ($\mu mol \cdot g^{-1} \cdot s^{-1}$)	Specific production rate ($\mu mol \cdot m^{-2} \cdot s^{-1}$)
T2-33	0.22	0.076	0.0034
T2-40	0.28	0.096	0.0035
T2-45	0.30	0.104	0.0035
T2-50	0.34	0.118	0.0039
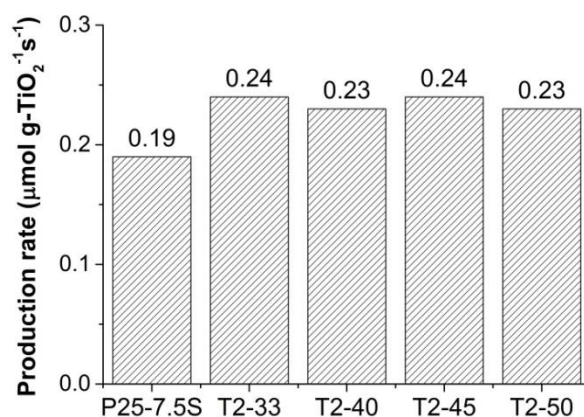
Figure 4.7 Production rates normalized by the mass of TiO_2 in the RF-heated and conventionally heated flow reactors.

4.4　Deactivation study

Although the TiO_2 loading of T2 CMC did not affect the catalytic activity, different deactivation curves of various T2 CMCs were observed in the RF-CR (Figure 4.8). As deactivation was related to the temperature, the difference on deactivation indicated the various temperature profiles of the catalytic bed using different CMCs as well as the overheated zone on pellet size. The CMC could be stabilized at the initial activity for a longer time if containing more $NiFe_2O_4$. This was due to the less heat generated per single CMC if more $NiFe_2O_4$ contained, decreasing the overheated spots on pellet size. Nevertheless, once the deactivation started, the deactivation was faster in the CMC containing more $NiFe_2O_4$. This was possibly attributed to the different temperature profiles along the catalytic bed. As the catalytic bed of CMC having more $NiFe_2O_4$ was longer, there would be more overheated section in this packed bed, leading to the deactivation caused by the high temperature.
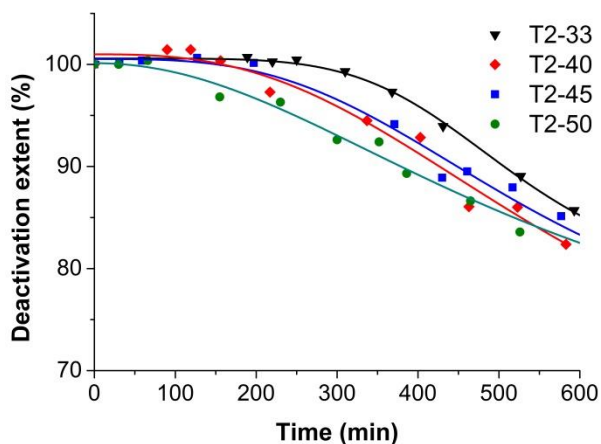
Figure 4.8 Deactivation extent of direct amide synthesis over ball milled CMCs with various titania loadings in the RF-heated continuous reactor

Besides the product inhibition by water produced in the process, there are three possible mechanisms of the CMC deactivation. As high temperature and organic compounds involved, coke is the most possible reason causing the deactivation. The formed coke can block the pores, resulting in the decrease of the surface area. The surface area can also be reduced by the sintering of the catalysts caused by the high temperature. Other factor inducing the deactivation may be the loss of sulfate groups or permanent

poisoning of the active sites on the surface. To identify the mechanism of deactivation, spent ball milled CMCs were firstly analysed by N_2 adsorption and desorption isotherms. Compared to the surface area of fresh CMCs, spent CMCs all showed lower surface areas ranging from 18.4 to 25.4 m^2/g. The production rates normalized by the surface area before and after the reaction were calculated to study the change of the active sites (Table 4.3 and Table 4.4). The specific production rates stabilized around 0.0035 $\mu mol \cdot m^{-2} \cdot s^{-1}$ for all fresh CMCs and the values for spent CMCs were nearly the same, indicating catalytic activity on available surface area did not decrease. Thus the hypothesis of the loss or poison of active sites on the catalysts could be excluded. The mass of coke formed in each CMC was analyzed by TPO. With the temperature continuously increasing from room temperature to 650 ºC, the CO_2 profile for all the samples showed the same wide peak locating from 150 to 550 ºC. The mass of coke calculated from peak areas in Figure 4.9 increased in the order of ST2-50, ST2-45, ST2-33, ST2-40 from 8.4 to 10.3 mg/g-CMC, which was coincident with the deactivation trend. In conclusion, the coke was one of the main reason causing the deactivation.
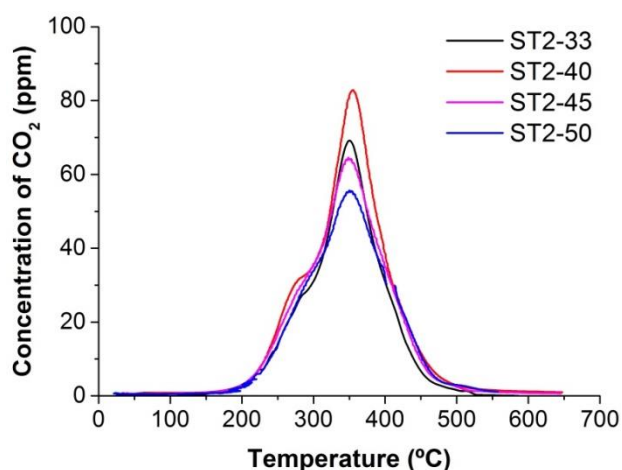
Figure 4.9 CO_2 profile of spent T2 CMCs in the TPO analysis

Table 4.4 Characterization and catalytic activity of spent T2 CMCs

	Surface area (m^2/g)	Mass of formed coke (mg /g-CMC)	Specific production rate ($\mu mol\ m^{-2}s^{-1}$)
ST2-33	18.4	9.5	0.0033
ST2-40	22.5	10.3	0.0039
ST2-45	23.2	8.8	0.0034
ST2-50	25.4	8.4	0.0036

4.5   Regeneration of ball milled magnetic catalysts

Due to the uniformity of ball milled CMCs, all of the CMC particles could be easily separated by the magnet from the packed bed. To remove the coke formed on the CMCs, calcination is the most common treatment. A proper condition to remove the coke was studied by TPO analysis. The temperature in the TPO analysis was set to increase with a heating rate at 5 ºC/min and then stay constant after reaching 400 ºC. The curve of CO_2 shows that most of the coke was burnt out before reaching at 400 ºC and the residue was totally removed after staying at 400 ºC for 45 min (Figure 4.10). Thus to regenerate the T2 CMCs, the spent CMC was calcined at 400 ºC for 1 h with a heating rate of 5 ºC/min in the air-flow tubular furnace.
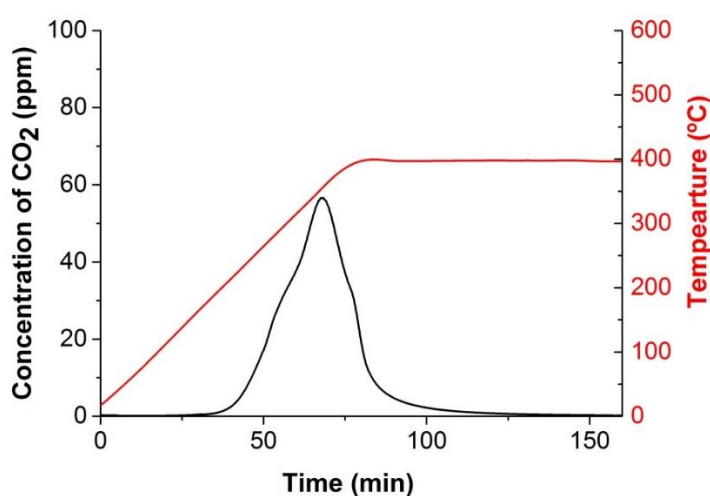
Figure 4.10 CO_2 profile of spent ball milled CMC (ST2-50) in the TPO analysis

Following this approach, ST2-50 CMC was regenerated for several cycles. Surface areas of T2-50 decreased slightly with the regeneration steps (Table 4.5). It was also observed that some small pores merged into bigger ones after each cycle according to the pore size distribution (Figure 4.11), indicating that the inner structure was slightly changed after each cycle.
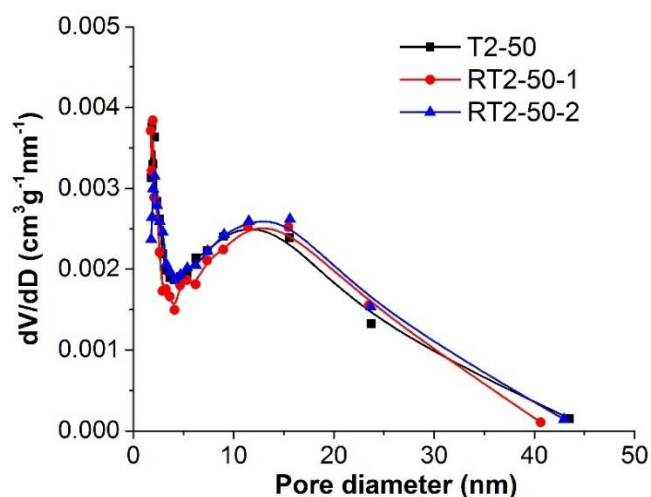
Figure 4.11 BJH pore size distribution of fresh and spent T2-50 CMCs derived from adsorption isotherm

Table 4.5 Surface area and initial rate constants of fresh and regenerated T2-50 CMCs

	Surface area (m^3/g)	Initial rate constant $(L \cdot mol^{-1} \cdot s^{-1})$
T2-50	30.2	0.34
RT2-50-1	29.1	0.34
RT2-50-2	28.3	0.35

The catalytic activities of regenerated CMCs were tested in the RF-CR under the same reaction condition. The initial rate constant of regenerated CMCs were around the same with a negligible trend of increasing, which demonstrated that the catalytic property could be fully recovered after the regeneration step. The slight increase of initial rate constant could be attributed to the faster internal diffusion of the reactants in larger pore sizes. Nevertheless, the deactivation was observed to accelerate after each regeneration process (Figure 4.12). This was possibly due to the change of the pore size distribution as well. If formed coke blocked the pore channels, it

would hinder the mass transfer to a larger surface area due to the bigger pore size and volume in regenerated CMC.
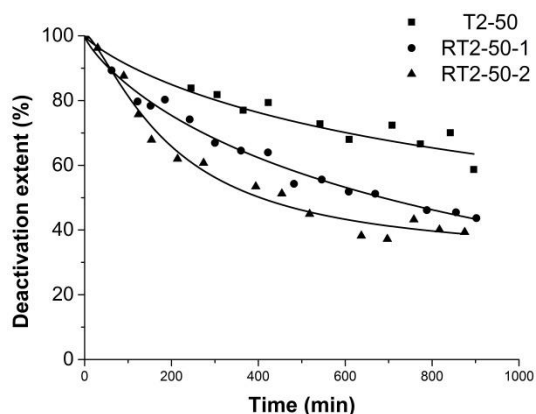
Figure 4.12 Deactivation extent of direct amide synthesis as a function of time over regenerated T2-50 CMCs. Reaction conditions: 50 mmol/L phenylbutyric acid and 50 mmol/L aniline, total flow rate 142 µL/min, 526 mg CMC, 150 °C, 7 bars.

4.6   Conclusions

Ball mill is a facile method to synthesize magnetic catalysts applied for RF heating. By milling the mixture at 300 rpm for 0.5 h, the uniformity could be achieved without forming new crystal phase. Both the surface area and SAR of the synthesized CMC could be maintained at good values in the obtained CMC. The production rate of direct amide synthesis over sulfated titania was promoted by 21% to 0.23 µmol·g-TiO_2^{-1}·s^{-1} in the RF-CR as compared to the value in the CH-CR, demonstrating a diminished temperature gradient in the RF-CR. The variation of titania loading in CMC did not affect the catalytic activity of titania but resulted in different deactivation rates. The deactivation occurred earlier but at a slower rate when the CMC with higher titania loading was applied. Overall, the CMC having 50 wt.% titania (T2-50) showed the highest catalytic activity and the lowest deactivation rate. Deactivation was mainly caused by the carbonization of organic compounds. The formed coke could be fully removed by calcinating the spent CMC at 400 °C for 1 h under air flow. The catalytic activity of the spent CMC could be totally recovered to the initial value by this regeneration process. However, faster deactivation was observed after each cycle due to the change of the morphology.

82

Chapter 5

Synthesis of NiFe$_2$O$_4$@TiO$_2$ core-shell catalysts for direct amide synthesis under RF heating

5.1 Introduction

Even though ball mill provides a facile way to synthesize the magnetic catalysts, the application area of ball milled CMC is actually limited due to the weak chemical resistance of the magnetic material. The exposed NiFe$_2$O$_4$ is easily corroded in the strong acidic or basic solutions, limiting the types of the reactants. To protect the magnetic property, the magnetic catalyst with a core-shell structure is synthesized to improve this situation. By covering the core with a shell, the core can be well protected from the surroundings, making the magnetic property stable during use. Moreover, the morphology of the shell can be easily tuned by synthetic process. Surface area and catalysts content in each CMC can be increased, further promoting the catalytic activity. However, the thickness of the shell also affects the heat transfer, resulting in different SARs of CMCs. The CMC with thinner shell has a relative higher SAR. In a word, properties of shell affected the heating and catalytic abilities in opposite ways. These two characteristics should be balanced when core-shell CMC is synthesized.

In this chapter, the core-shell NiFe$_2$O$_4$@TiO$_2$ (T3) CMC was synthesized by the sol-gel method. Calcination temperature as the main parameter affecting crystal form and surface area was studied and optimized. The effects of TiO$_2$ content on heating property, surface area were explored as well. The catalytic activities of all the core-shell CMCs were tested and compared in the RF-CR with a 5 mm single catalytic bed under the same reaction

83

condition. Characterization methods like TGA, XRD, SEM, N_2 adsorption/desorption isotherms and VSM were used to study the physical properties of CMCs. Deactivation mechanism and regeneration method were explored as well to regenerate the spent CMCs.

5.2 Characterization of core-shell magnetic catalysts

5.2.1 Identification of TiO_2 content

CMCs with different TiO_2 content were synthesized by varying the volume of TiO_2 sol added in during the synthesis process. As shell acted as the catalyst, the content of TiO_2 in T3 CMC was the main parameter to be concerned. According to the results from SEM-EDS (Table 5.1), actual TiO_2 content changed from 8.9 to 32 wt.%, which was coincident with the nominal TiO_2 loading calculated from mass of each precursor. The actual TiO_2 content was slightly higher than the nominal value, which was due to the accidental error. According to the data the precursor of TiO_2 was fully incorporated on the surface of the core by this method.

Table 5.1 Nominal and actual titania loadings in T3 CMCs calcined at 400 $^{\circ}$C.

	Nominal TiO_2 content (wt.%)	Actual TiO_2 content (wt.%)
T3-9-400	7.4	8.9
T3-17-400	13.9	16.7
T3-26-400	24.3	26.0
T3-32-400	32.5	32.0

Nearly spherical particles were observed in TEM images of all four samples. The mean $NiFe_2O_4$ particle size remained rather constant and was close to 50 nm. Arrows shown in Figure 5.1 point to the TiO_2 detected by EDS, showing the existence of TiO_2 shell with the thickness of about 5-10 nm. The incorporation of titania coating did not change the average dimension of the

NiFe$_2$O$_4$ core (40–60 nm in diameter), showing no chemical interaction between the core and the shell during the synthesis.
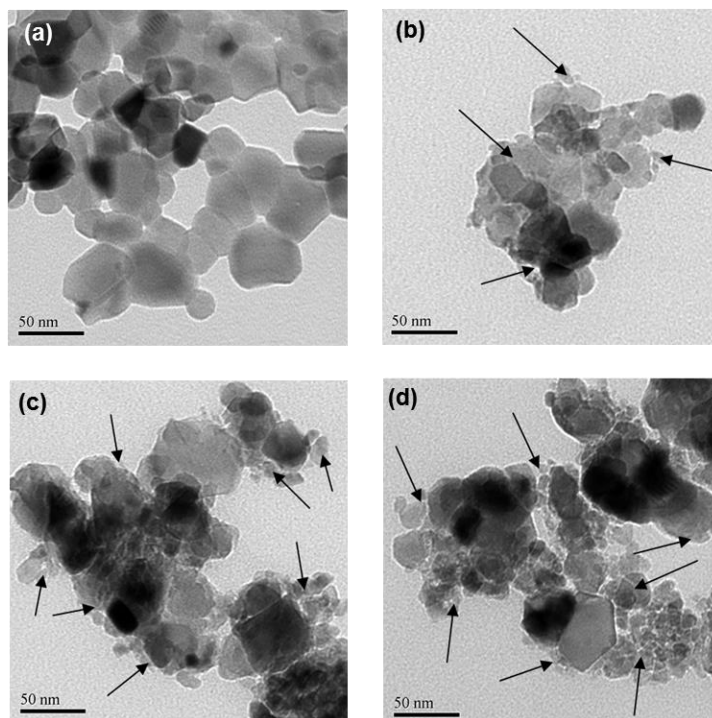
Figure 5.1 TEM images of (a) initial nickel ferrite nanoparticles and T3 CMCs calcined at 400 °C with different TiO$_2$ loadings (b) T3-17-400 (c) T3-26-400 (d) T3-32-400. Arrows point to the TiO$_2$ shell.

The FT-IR spectra of the T3 CMCs calcined at 400 °C along with dry gel of TiO$_2$ and NiFe$_2$O$_4$ spectrum are shown in Figure 5.2. The peaks at 590 cm^{-1} were assigned to stretching vibrations of Fe-O [187] in NiFe$_2$O$_4$. Stretching of Ti-O-Ti framework was located in the wide range from 1000 to 400 cm^{-1} in the spectrum of the dry gel of TiO$_2$ [43, 179, 188, 189], which were partially overlapped by the NiFe$_2$O$_4$ bands in the T3 CMCs. The intensity of the Fe-O peak at 590 cm^{-1} increased proportionally to NiFe$_2$O$_4$ content. Also the width of the Fe-O band, which was close for all composite catalysts, was noticeable broader compared to that of NiFe$_2$O$_4$. This broadening suggests very close contact between NiFe$_2$O$_4$ and TiO$_2$ and confirms the formation of the core-shell structure in agreement with TEM data.
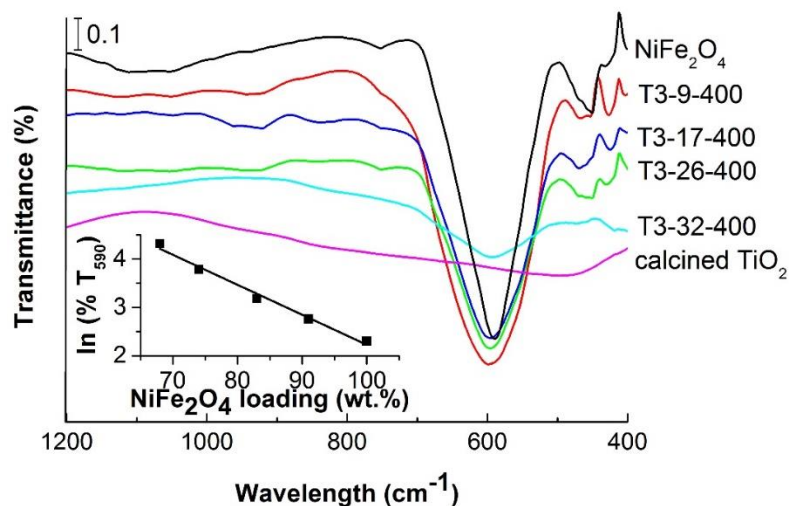
Figure 5.2 FT-IR spectra over 400 °C calcined TiO_2 gel, $NiFe_2O_4$ and T3 CMCs calcined at 400 °C.

5.2.2 Thermal behaviour

Removal of the surfactants remaining in the as-synthesized CMCs is of crucial importance for the properties of final products. Total remove of the surfactants can generate the maximum number and volume of pores in the shell, resulting in the highest surface area. Surfactants from sol-gel are normally removed by calcination process. High temperature can accelerate the burn out of the surfactants, and also it determines the crystal phase formed. However, over high temperature may result in the phase transformation of the original catalytic and magnetic part or even formation of new compound at the boundary layer between core and shell, leading to the loss of heating and catalytic properties. In this way, it is necessary to understand the thermal behaviour of the T3 CMCs.

The TG-DTA curves ranging from room temperature to 1000 °C of the TiO_2 dry gel, nickel ferrite particles and uncalcined T3 CMCs with TiO_2 loading of 17, 26 and 32 wt.% were presented in Figure 5.3. For the TiO_2 dry gel, the weight loss between 75 to 165 °C was attributed to the desorption of ethanol and water remaining in the gel. The decomposition of the precursors was observed in the range from 270 to 323 °C [190]. Finally, the oxidation of residual organic compounds occurred above 475 °C and weight became constant after 570°C, indicating full removal of combustible materials. DTA

curve showed the main exothermal peak starting from 500 °C, indicating the fast combustion of coke or organic residue (Figure 5.3 (a)). $NiFe_2O_4$ showed good thermal stability according to Figure 5.3 (b). The weight of the nickel ferrite sample remained virtually the same during the whole process, which dropped only 1.5% after 1000 °C. The slight weight loss after 300 °C was due to the residue carbon left in the synthesis process. The stable phase of $NiFe_2O_4$ was obtained by calcination at 700 °C in agreement with the previous reports [191, 192]. Thermogravimetric analysis of composite samples with different TiO_2 loadings depicted the similar TG-DTA curve as TiO_2 dry gel (Figure 5.3 (c)). The as-synthesized samples exhibited continuous weight losses at the temperature below 570 °C caused by the removal of the solvents and organic compounds and the main exothermic peaks appeared at 550 °C because of the combustion of residue coke. In particular the thermal effect above 570 °C in the composite materials was lower than that of $NiFe_2O_4$ and no other exothermal peaks observed after 600 °C, which means no solid-state reaction happening between TiO_2 and $NiFe_2O_4$ in the CMCs. The weight loss increased from 10.2% to 25.1% as TiO_2 content in the samples increased from 8.9 to 32 wt.%. These values agreed well with the theoretical loss calculated from the weight loss of nickel ferrite, TiO_2 and the actual TiO_2 loading in the composite materials.
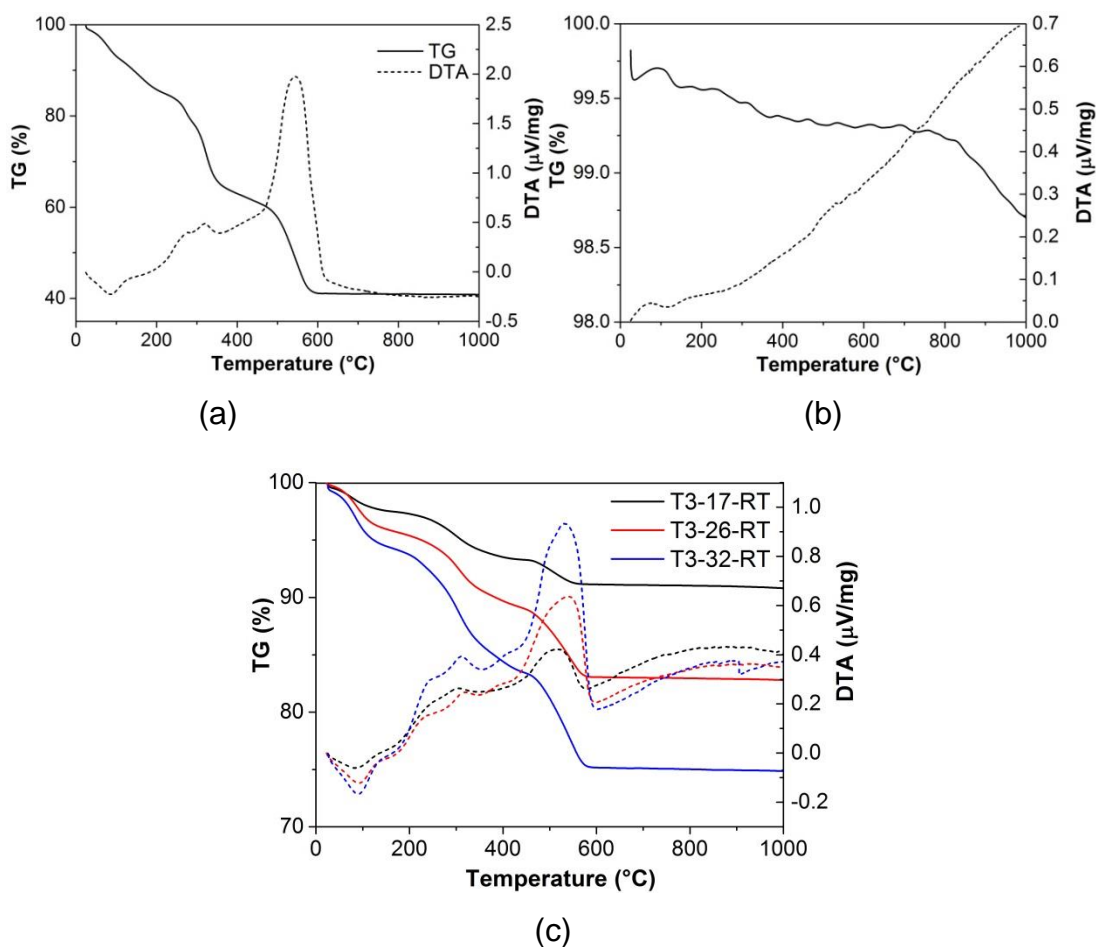
Figure 5.3 Thermal gravimetrical and differential thermal analysis of (a) dry gel of TiO_2 (b) $NiFe_2O_4$ (c) uncalcined T3 CMCs with various titania loadings

5.2.3 Magnetic properties

The magnetic property of original magnetic particles can be diluted by the portion of TiO_2 in the CMC. The magnetisation curves and corresponding parameters of the T3 CMC calcined at 400 °C are shown in Figure 5.4 (a) and Table 5.2 respectively. As coercivity (H_c) significantly depends on magnetic particle dimensions [141], the same coercivity at 0.2 kG for all samples indicates the dimension of $NiFe_2O_4$ particle was not affected by the introduction of TiO_2 shell, which was in agreement with the TEM data (Figure 5.1) and TGA data (Figure 5.3). With the increase of the titania loading, the saturation magnetization decreased from 31.3 to 22.0 emu/g because of the decreasing amount of the magnetic $NiFe_2O_4$. As shown in Figure 5.4 (b), saturation magnetization (M_s) had a linear relationship with TiO_2 content, showing the magnetism loss of T3 CMC was only due to the dilution of TiO_2.

There was no additional loss of magnetism observed due to the formation of titania shell. For ferromagnetic material, the heating property was proportional to the hysteresis area according to Dr. Gao's research [141]. The decreased hysteresis area indicates the heating property dropped as more TiO_2 contained. Curie temperature measured from M-T curve was nearly constant at 565 °C for all samples, proving the stability of $NiFe_2O_4$ phase after coating the TiO_2 shell. It is also worthy pointing out that the application of these CMCs should be under this temperature to avoid the change of the magnetism.

(a)   (b)
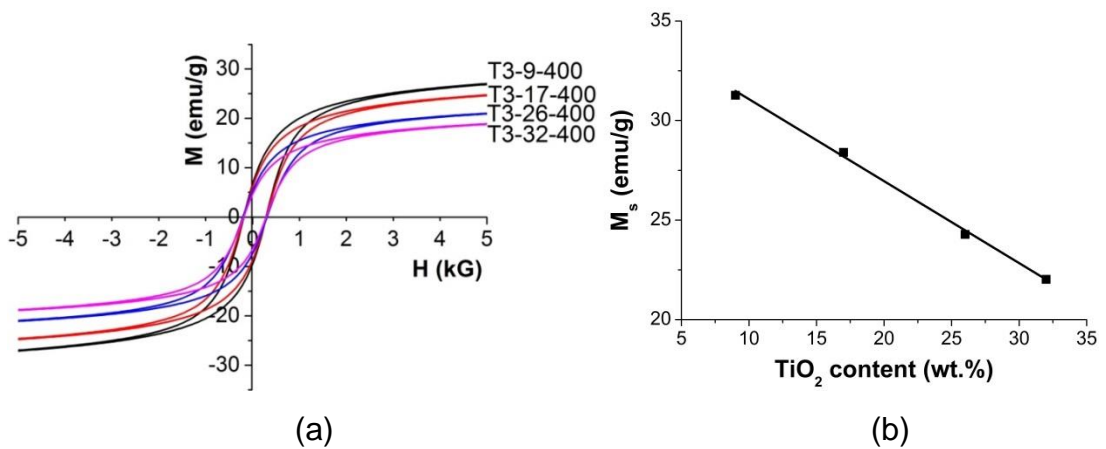
Figure 5.4 (a) Hysteresis curves of T3 CMCs with different TiO_2 loadings measured at 20 °C (b) Relationship between M_s and TiO_2 content

Table 5.2 Magnetic properties of T3 CMCs with different TiO_2 loadings calcined at 400 °C

	M_s (emu/g)	H_c (kG)	Curie temperature (°C)	Hysteresis area (J/g)
T3-9-400	31.3	0.2	565	0.22
T3-17-400	28.7	0.2	570	0.20
T3-26-400	24.3	0.2	565	0.17
T3-32-400	22.0	0.2	565	0.15

5.3 Effect of calcination condition on physical properties

The calcination temperature has a major influence on the phase composition of the resulting core-shell CMCs. The calcination step is necessary to remove the remaining structure directing agent from the porous network and the temperature should be sufficiently high for its full oxidation. Moreover, the temperature should provide transition of titania into catalytically active anatase phase, but not high enough for the sintering or conversion into a less active rutile phase [193, 194]. According to the TGA analysis (Figure 5.3), all the surfactants can be removed at 500 °C. Transformation temperature from anatase to non-catalytic rutile was ever reported from 400 to 1200 °C according to the specific condition [195]. Also, the calcination temperature should be below Curie temperature at 565 °C to keep the magnetism of the cores. Considering all three aspects mentioned above, the calcination temperature was chosen in the range of 350 to 500 °C. The effects of calcination temperature on surface area and SAR were studied with the core-shell CMC having a TiO_2 loading of 26 wt.%. The sample was calcined at 350, 400, 450 and 500 °C to study phase composition and check for possible core-shell interaction.

XRD spectra of CMC with TiO_2 loading of 26 wt.% calcined at different temperature are shown in Figure 5.5. The XRD peaks at 25.4 and 48.2 °2θ were corresponding to the (101), (200) crystal planes of anatase (JCPDS card no. 78-2486). It could be seen that the formation of characteristic anatase phase began at 450 °C and the peak intensity increased as temperature rose to 500 °C. The peaks at 30.7, 36.0, 37.6, 43.8, 54.8, and 64.4 °2θ were assigned to a $NiFe_2O_4$ structure (JCPDS card no. 74-2081). These peaks were well indexed to the crystal plane of spinel ferrite (220), (311), (222), (400), (422), (511) and (440), respectively. The very small peaks at 31.4 and 41.3 °2θ proved the existence of (220), (113) crystal planes of α-Fe_2O_3 (JCPDS card 33-0664), which was the impurity when nickel ferrite was synthesized. As less surfactant and thus larger weight fraction of $NiFe_2O_4$ contained in CMC calcined at a higher temperature, intensity of observed peaks representing $NiFe_2O_4$ slightly grew as calcination

temperature increased from 350 to 500 °C. In the patterns of all the T3-26-Z samples, besides peaks of α-Fe_2O_3, TiO_2 and $NiFe_2O_4$, no other peaks were observed in the pattern, indicating no further solid reaction between catalytic and magnetic part happening at 500 ºC. The crystal size of $NiFe_2O_4$ in each sample was estimated using FWHM of the highest $NiFe_2O_4$ peak (311) by Scherrer equation (Eq. (3.5)). The crystal sizes of $NiFe_2O_4$ for the initial and calcined CMC were 52 - 57 nm. Which were in good agreement with the size estimated from TEM images (Figure 5.1). Hence, the calcination temperature of 450 – 500 ºC was beneficial considering anatase formation, while no core-shell interaction or rutile formation occurred.
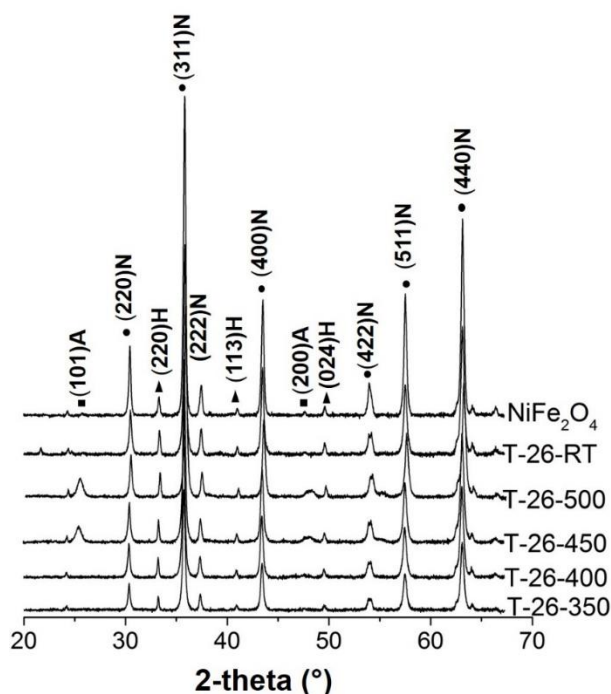
Figure 5.5 XRD patterns of $NiFe_2O_4$ and T3 CMCs with 26 wt.% titania calcined at different temperatures. The peaks are assigned to (N) $NiFe_2O_4$, (A) anatase titania, (H) hematite Fe_2O_3.

Besides the removal of the surfactants, calcination could also affect the surface area as well as the heating properties. Details of surface area and SAR for calcined samples are listed in the Table 5.3. Compare to the as-synthesized CMC, values of both surface area and SAR decreased by 30% after calcination at 350 ºC. The decrease of surface area was likely caused by the condensation and densification of the amorphous titania network

during the calcination resulting in the increase in TiO_2 particle sizes, which was observed for many porous materials[196-198]. The surface area remained constant in the CMCs calcined at 350-450 ºC range and it slightly increased after calcination at 500 ºC due to complete removal of the structure directing agent.

As mentioned in section 1.6.1, the mechanism of RF heating varied according to the magnetic particle dimension [72]. As the superparamagnetic and single domain diameters for $NiFe_2O_4$ are 28 and 100 nm respectively [72, 199], the particle size of $NiFe_2O_4$ around 50 nm was located in the range where Néel relaxation, Brownian rotation and hysteresis loss all existed. The higher SAR value of T3-26-RT CMC might be attributed to the different surface properties of uncalcined CMCs resulting in a stronger interaction with water and a higher Brownian heat generation. For the series of T3 catalysts containing 26 wt.% of titania, an increase in calcination temperature from 350 to 500 °C resulted in a minor increase of SAR values likely due to residue extent of the surfactants in the CMCs calcined at different temperatures.

Table 5.3 Surface area and SAR of T3 CMCs

	Surface area (m^2/g)	SAR value (W/g)
T3-26-RT	44.9	1.00
T3-26-350	31.8	0.73
T3-26-400	30.7	0.76
T3-26-450	32.4	0.86
T3-26-500	35.1	0.87
T3-9-500	21.9	1.08
T3-17-500	25.0	1.05
T3-32-500	51.9	0.88

Calcination at 500 °C was proved to result in the T3 CMC having the maximum surface area, heating property as well as the anatase TiO_2. However besides calcination temperature, calcination time was another factor affecting the components of CMC. To determine the calcination time,

uncalcined CMC having 32 wt.% titania was analysed by programmed TPO analysis which was designed to heat at 5 °C/min to 500 °C and then stay for 7 h. According to Figure 5.6, the curve of H_2O showed two peaks at 30 °C and 245 °C, representing the release of water moisture and desorption of bonded H_2O on the surface respectively. CO_2 curve showed a wide peak area starting from 162 °C to 500 °C, which was due to the multi types of carbon species contained in the CMC. CO_2 and H_2O were totally removed after temperature stabilizing at 500 °C for 20 min. Thus the calcination condition of heating at the rate of 5 °C and then stabilizing at 500 °C for 1 hour was enough to remove all the impurities in the T3 CMCs.
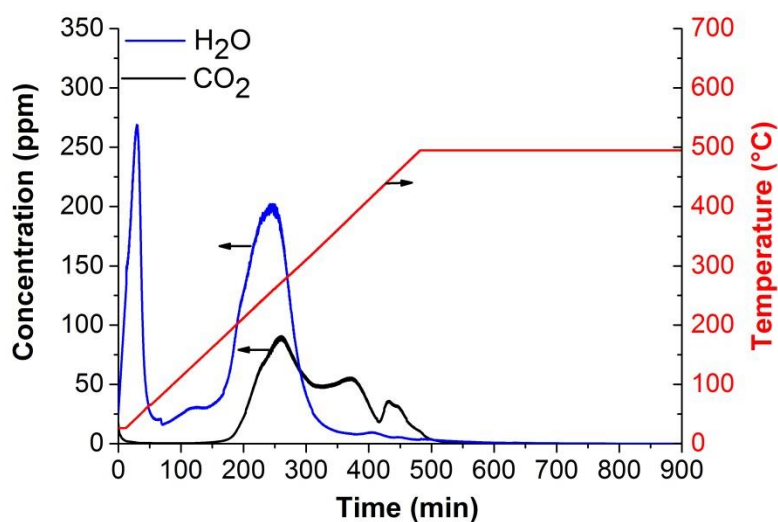
Figure 5.6 CO_2 and H_2O profiles of uncalcined T3 CMC with 32 wt.% titania in a TPO analysis

To study the effect of titania loading, T3 CMCs having various TiO_2 loadings from 9 to 32 wt.% were calcined at 500 °C for 1 h. The surface area and SAR of each CMC are listed in the Table 5.3. The surface area increasing from 21.9 to 51.9 m^2/g was due to the thicker shell of TiO_2. However, SAR values decreased steadily with increasing TiO_2 content. This phenomenon was obviously associated with the decrease in $NiFe_2O_4$ content. Compared to the ball milled CMC having nearly the same TiO_2 extent at 33 wt.% , the surface area of core-shell CMC having 32 wt.% titania was 2.3 fold of that of ball milled T2-33 CMC. However, the SAR of T3-32-500 CMC at 0.88 W/g was lower than that of T2-33 CMC at 1.7 W/g, which was probably due to the reduced effect of Brownian rotation in the core-shell CMC. In conclusion,

93

compared to the ball milled CMC, the surface area of core-shell CMC was improved while heating ability lost to some extent.

5.4 Catalytic activity and stability

5.4.1 Effect of calcination temperature on catalytic activity

The content of catalytic TiO_2 anatase phase was proved to change with the calcination temperature. To verify the effect on catalytic property, T3-26 CMC calcined at different temperatures were applied to catalyse the amidation of 4-phenylbutyric acid and aniline in the batch reactor (Figure 5.7). In order to compare with the activity of pure P25 TiO_2, the reaction rates over CMCs were normalized by the mass of TiO_2. The reaction rate showed an increased trend with the calcination temperature from 350 to 500 °C. Remarkably, the samples calcined at 450 and 500 °C demonstrated similar reaction rates at 0.093, 0.097 µmol $(g\text{-}TiO_2)^{-1}s^{-1}$ respectively, which were 2.5 times higher than that over the catalyst calcined at 350 °C. The sharp increase was mainly attributed to the rapid formation of active anatase phase, which had been verified by the XRD patterns. An increase in the specific surface area for the T3-26-500 CMC compared to that of T3-26-450 CMC might also contributed to a slightly increased reaction rate. Importantly, the catalytic activity per gram of TiO_2 for the T3-26-500 CMC reached the value of the reference P25 TiO_2 catalyst, demonstrating that magnetic functionality can be introduced into catalysts without affecting their catalytic activities.
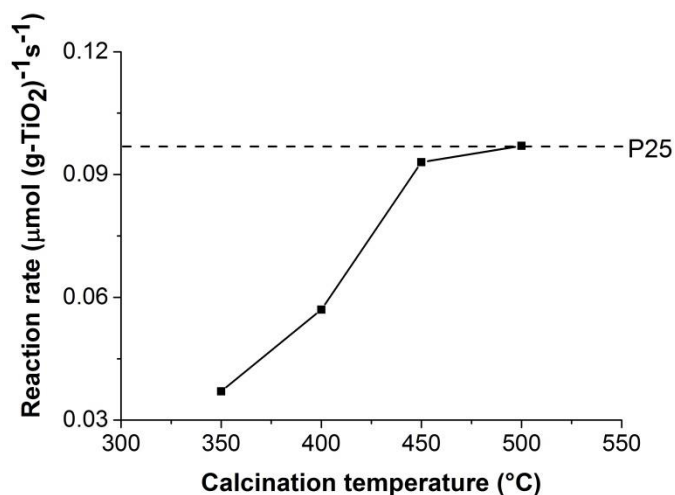
Figure 5.7 Reaction rates of direct amide synthesis over T3 CMCs with 26 wt.% titania calcined at different temperatures (T3-26-Z) in the batch reactor. Reaction condition: 50 mmol/L 4-phenylbutyric acid and 50 mmol/L aniline in p-xylene (100 mL), 0.635 g CMC, 150 °C, 6 bars. The dashed line designated the reaction rate over commercial P25 TiO_2 catalyst.

5.4.2 Effect of TiO_2 loading on catalytic activity

To explore the effect of titania content, the activities of CMCs with different TiO_2 loading were measured in a flow reactor with 5 mm catalytic bed under RF heating. The catalytic bed was shortened to the minimum in order to avoid the temperature gradient along the reactor. To preheat the stream, a 5 mm preheating packed bed filled with Fe_3O_4 (125-250 µm) was placed prior to the catalytic bed. Because T3 CMCs with various TiO_2 content showed different SARs, the intensity of the magnetic field (i.e. current) was adjusted with various CMCs in order to keep the same reaction temperature. The specific reaction conditions are listed in Table 5.4. As the CMC with higher TiO_2 content had the lower SAR, It can be seen that the RF power needed to maintain the reaction temperature increased from 101 to 142 W as the titania loading increased from 9 to 32 wt.%.

Table 5.4 Production rates and power supplied in the RF-CR packed with T3 CMCs containing various titania loadings. Reaction conditions: 50 mmol/L 4-phenylbutyric acid and 50 mmol/L aniline in p-xylene, total flow rate 40 μL/min, 320 mg CMC, 150 °C, 7 bars

	Current (A)	Power (W)	Initial rate constant $(L\,mol^{-1}s^{-1})$	Initial production rate		
				$(\mu mol\ g^{-1}s^{-1})$	$(\mu mol\ g\text{-}TiO_2^{-1}s^{-1})$	$\times 10^{-4}$ $(\mu mol\ m^{-2}s^{-1})$
T3-9-500	94.4	101	0.006	0.0048	0.05	2.4
T3-17-500	99.2	117	0.040	0.023	0.14	9.9
T3-26-500	105.6	134	0.059	0.030	0.12	9.0
T3-32-500	110.4	142	0.150	0.049	0.15	9.7

Under the same reaction condition, the initial production rates and rate constants over T3-Y-500 CMC increased with the TiO_2 content, which was expected because of the increasing number of the active sites. However, The large difference between the initial rate constants of T3-9-500 and T3-32-500 indicates that not only number of the acid sites affected catalytic activity. According to the initial production rate normalized by the mass of TiO_2, it showed that T3-9-500 CMC had a much lower value while other three samples were close (Table 5.4). It indicates that a negative interaction between $NiFe_2O_4$ and TiO_2 existed for thinner TiO_2 layer. The electronic interaction between TiO_2 and ferrite named as photodissolution phenomenon were also reported in other studies [129-132]. When the TiO_2 shell became thicker, such detrimental effect decreased likely due to minimisation of the contact with magnetic core.

A strong deactivation occurred but performed differently during the direct amide synthesis in the RF-CR packed with various CMCs. For a proper comparison of deactivation kinetics, the production rates were normalised by the initial production rate (r/r_0) to obtain the deactivation extent (Figure 5.8). Such deactivation behaviour is usually modelled using simple first order kinetics considering slow deactivation caused by blockage of catalysts surface which is caused by the occurring chemical reaction [198, 200]. The

corresponding deactivation rate (production rate r normalised by the initial rate r_0) is presented in Eq. (5.1), where $k_{deactiv}$ is the deactivation constant and t is time on stream.

$$r / r_0 = \exp(-k_{deactiv} \cdot t)$$ (5.1)

The values of deactivation constant were proportional to titania loading as shown in Figure 5.8 (b). Hence, the deactivation rate constant for the catalyst containing 9 wt.% titania was almost 3 times as high as for the catalyst containing 32 wt.% titania. However, this result is not surprising considering that a blockage of an active site for the catalyst containing a small number of sites provides much higher relative deactivation compared to the catalyst with a larger number of sites. In fact, the linear relationship between the deactivation constant and TiO_2 loading (number of active sites) suggests the same deactivation mechanism and the same overall deactivation rate constant.

(a)   (b)
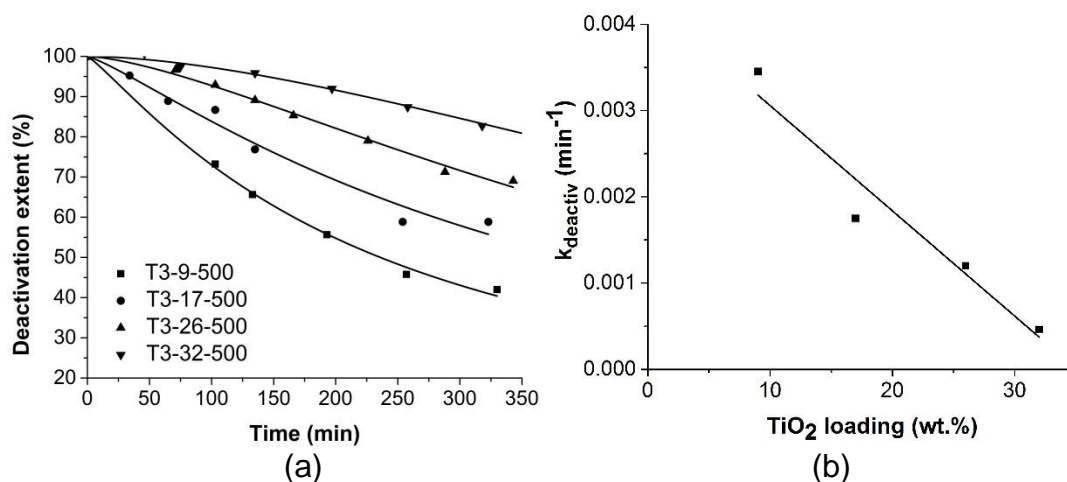
Figure 5.8 (a) Deactivation extent of direct amide synthesis over T3-Y-500 CMCs as a function of time (b) Deactivation constant as a function of TiO_2 loading. Reaction conditions: 50 mmol/L 4-phenylbutyric acid and 50 mmol/L aniline in p-xylene, total flow rate 40 µL/min, 320 mg CMC, 150 °C, 7 bars

To verify the benefit of RF heating, T3-32-500 CMC was loaded in both the conventionally heated and RF-heated reactors filled with the same T3-32-500 CMC (Figure 5.9). The initial rate constant obtained in the RF-CR was 2.3 times of that in the CH-CR, which were 0.065 and 0.15 L·mol^{-1}s^{-1} respectively. It was due to the different temperature distribution in the reactors. For conventionally heated reactor, as heat was transferred from the

heated outer surface via the reactor wall to the CMC inside, it created an axial temperature gradient on the radical axis of the reactor, resulting in a colder stream in the centre. However, in the RF-heated reactor, heat was contributed by each CMC particle thus temperature gradient was largely reduced on the cross section. As temperature of the bulk phase in conventionally heated reactor was lower, it led to a lower rate constant compared to RF heating. The higher temperature achieved in the RF-CR can also be proved by the faster deactivation observed in Figure 5.9.
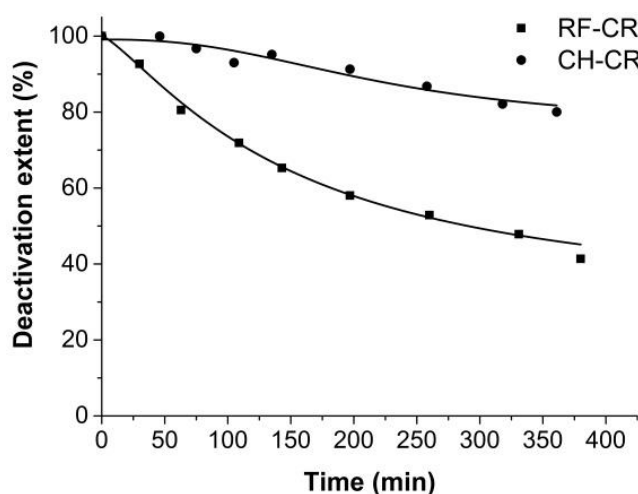
Figure 5.9 Deactivation extent of direct amide synthesis over T3-32-500 CMC as a function of time in the RF-heated and conventionally heated continuous reactors. Reaction conditions: 50 mmol/L 4-phenylbutyric acid and aniline in p-xylene, total flow rate 40 µL/min, 320 mg CMC, 150 °C, 7 bars

5.5   Deactivation study

Deactivation was observed during all the experiments in flow reactor on T3 CMCs. The deactivation was likely caused by the formation of trace amounts of azobenzene species on the catalyst surface which readily decompose to form coke and block the catalyst surface [1, 15]. Production inhibition by H_2O was also the reason causing the deactivation. Another possible reason was the permanent loss of active sites. To verify the reactivity of acid sites, initial and final production rates were normalized by the surface area instead of mass of CMC (Table 5.5). It should be mentioned that as the surface area was analysed after the sample was degassed, the effect of H_2O could not be

studied by this parameter. The slight weight loss after degassing process at 250 °C was observed in each sample which was dried at 110 °C previously, indicating the existence of chemisorbed water on the spent CMCs. The production rate normalized by surface area of TiO_2 shell remained virtually the same (9.7×10^{-4} vs 10.1×10^{-4} μmol m^{-2}s^{-1}) in the spent ST-32-500 CMC having the highest titania loading while it slightly reduced in the catalysts with lower titania loadings (Table 5.5). However, after reaction, it was observed that surface area of ST3-Y-500 CMC significantly dropped by 20% to 30% compared to the fresh catalysts. It indicates that it was the decrease of the surface area and site blockage caused the deactivation instead of the permanent loss of the acid sites. These processes may occur separately or can be caused by the same reason such as surface coking.

Table 5.5 Surface area of spent T3 CMCs having various titania loadings

	Surface area (m^2/g)	Specific production rate x 10^{-4} (μmol m^{-2}s^{-1})
ST3-9-500	15.6	1.5
ST3-17-500	20.0	7.5
ST3-26-500	26.7	8.3
ST3-32-500	40.8	10.1

In order to study the deactivation mechanism caused by coke, TPO analysis was further performed on spent CMCs (Figure 5.10). It should be mentioned that the coke was normalized by the amount of titania for proper comparison. Peak area showed in the wide range from 200 to 500 °C. The main peaks at 260, 350 and 465 °C indicate there were three types of coke species formed during the reaction. The peak at 465 °C only showed in pattern of ST3-9-500 CMC, indicating the strongly adsorbed coke was formed when TiO_2 layer was as thin as T3-9-500 CMC. As heat was generated by magnetic core and transferred through the shell, solution was easily overheated in the CMC particle having thinner layer of TiO_2. The amount of cokes gradually decreased from ST3-9-500 to ST3-32-500 CMCs, which was consistent with the deactivation kinetic data. From these data it can be concluded that the formation of the coke on the surface was the dominating reason for the

decrease of the surface area and further the deactivation. The minimum activity loss was 40% in 6 h, which was faster than the catalyst reported from mechanochemical synthesis. It is possibly caused by a larger contacting surface area between catalyst and magnetic parts.
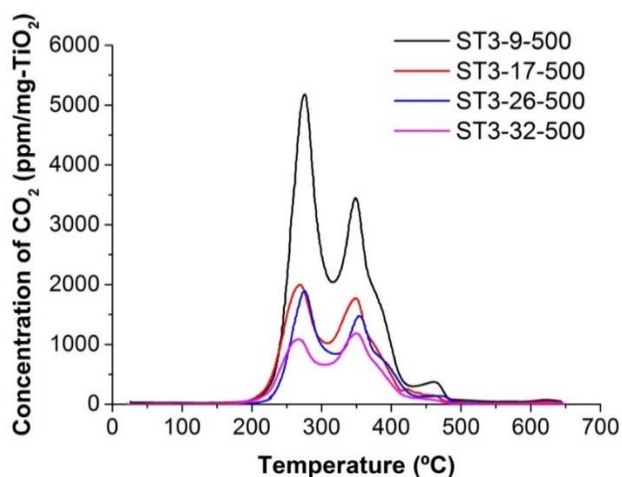
Figure 5.10 Normalized CO_2 curves of spent T3 CMCs with various titania loadings in TPO analysis

5.6   Regeneration of core-shell magnetic catalysts

As formation of the coke and adsorbed water resulted in the deactivation, a proper method to remove the coke and water should be found out. Calcination was the most common used method. According to the TPO curve shown in Figure 5.10, peaks representing two types of coke showed at 260 °C and 350 °C respectively, thus 400 °C was enough to burn out all the cokes. To study the calcination condition, programmed TPO analysis up to 400 °C was done on ST3-32-500 CMC. Figure 5.11 shows that no residue of coke remained after temperature reaching to 400 °C for 40 min. The regeneration process of calcinating at 400 °C for 1 h was enough to remove all the coke formed.
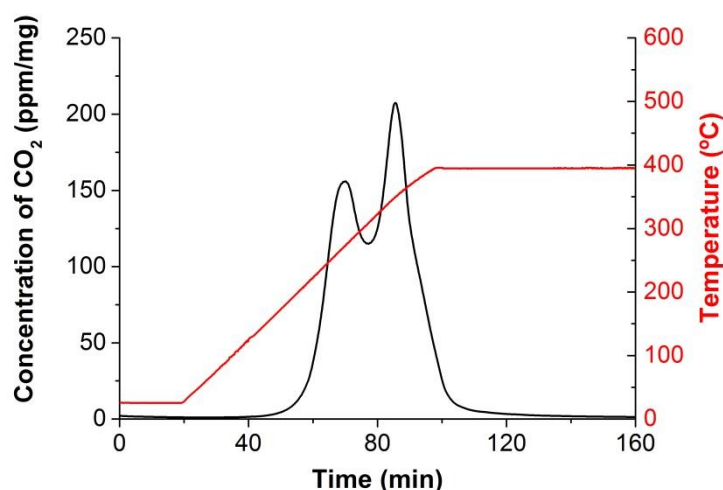
Figure 5.11 CO_2 profile of spent T3-32-500 CMC in TPO analysis.

A sharp decrease of surface area was observed after regeneration by calcination. Surface area dropped to 30.2 m^2/g likely due to the sintering while that of the fresh catalyst was 51.9 m^2/g (Table 5.6). This led to a much lower initial rate constant as shown in Table 5.6. The production rate was even lower than the spent CMC while surface area normalized production rate was the same (Figure 5.12). This indicates the catalytic activity of active sites did not change with the calcination process while the surface area of T3 CMC was decreased due to the high temperature. Deactivation also became fast due to the less active sites. A proper method avoiding high temperature should be tried.

Table 5.6 Surface area and catalytic activity of regenerated T3-32-500 CMCs. Reaction conditions: 50 mmol/L 4-phenylbutyric acid and aniline, total flow rate 40 μL/min, 320 mg CMC, 150 °C, 7 bars

	Surface area (m^2/g)	Initial rate constant $(L\ mol^{-1}s^{-1})$	Specific production rate x 10^{-4} (μmol $m^{-2}s^{-1}$)
TRT3-32-500	30.2	0.130	10.1
WRT3-32-500	48.5	0.059	9.8
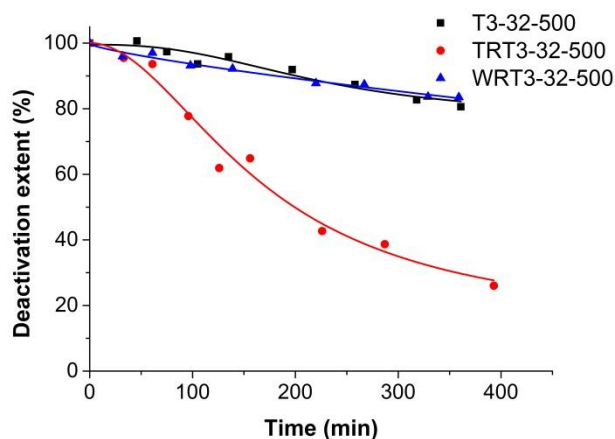
Figure 5.12 Deactivation extent of direct amide synthesis as a function of time over fresh T3-32-500, calcination regenerated T3-32-500 (TRT3-32-500) and H_2O_2 regenerated T3-32-500 (WRT3-32-500). Reaction conditions: 50 mmol/L 4-phenylbutyric acid and aniline, total flow rate 40 µL/min, 320 mg CMC, 150 °C, 7 bars.

According to Querini [201], 99.38% of coke could be removed by immerging the sample in hydrogen peroxide at 90 °C for 20 h. Following this approach, the surface area of regenerated CMC was 48.5 $m^2 g^{-1}$, which was marginally lower than the value of initial fresh catalyst (Table 5.6). The TPO data and the fact that the surface area of the spent catalyst can be recovered almost completely by mild treatment discards the possibility of catalyst deactivation via sintering and demonstrates that the dominant deactivation mechanism was associated with the formation of coke. In particular, the surface area of WRT3-32-500 CMC did not show the remarkable decrease while the amount of the bigger pore sizes increased compared to the fresh T3-32-500 CMC (Figure 5.13). This phenomenon was also observed in the regeneration of ball milled CMC (Section 4.5). As T2 and T3 CMCs were regenerated by different methods, it can be inferred that the change of the pore sizes was possibly caused by the mechanical force during the rotation of magnetic particles in RF field instead of the regeneration procedure.

The results of the catalyst testing show that when carrying out the treatment of spent catalyst with hydrogen peroxide at 90 °C overnight, the coke can be removed completely without catalyst sintering, because the catalytic activity was fully restored in the chemically regenerated sample (Table 5.6). Also the second catalytic run using WRT3-32-500 catalyst followed the same

deactivation kinetics as the first run indicating that the slight change of the pores distribution did not affect the deactivation in the observed time on stream. Therefore, H_2O_2 treatment could be regarded as an efficient route to recover T3 CMC.
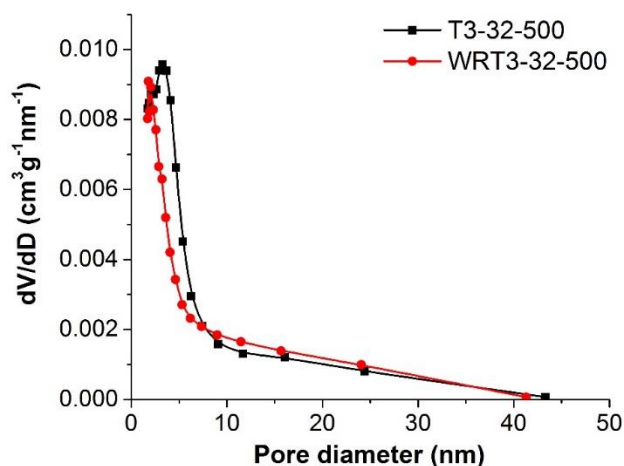
Figure 5.13 BJH pore size distribution of fresh (T3-32-500) and regenerated T3-32-500 CMCs (WRT3-32-500) derived from N_2 adsorption isotherm

5.7 Conclusions

In summary, core-shell $NiFe_2O_4@TiO_2$ CMCs have been successfully prepared by sol-gel method. By this approach, the TiO_2 content could be accurately adjusted by changing the amount of titania precursor in the initial synthesis sol. Also, no chemical reactions happened between $NiFe_2O_4$ and TiO_2 during the synthesis, which avoided the loss of both heating and catalytic properties. The optimisation of the catalyst calcination temperature showed that the transition of titania into catalytically active anatase phase started at 450 °C, resulting in the highest catalytic activity of the catalyst calcined at 500 °C and no sintering of the titania shell.

In terms of TiO_2 content in CMC, the catalytic activity increased as CMC contained more TiO_2 while the specific production rate (i.e. normalised by titania content) was constant for the catalysts with the titania loading above 17 wt.%. However, the catalyst with 9 wt.% showed an activity lower by 60% likely because of a significant contribution of electronic interaction between the magnetic core and the catalytic shell in the catalyst. The catalyst

103

deactivation rate was described by first order kinetics demonstrating deactivation rate constant was inversely proportional to titania loading, i.e. the catalyst with the highest titania loading of 32 wt.% deactivated by a factor of 6 slower compared to the catalyst with 9 wt.% titania. Thus CMC containing 32 wt.% titania was determined as the optimized point, for it had the good heating property, best catalytic performance as well as the least deactivation extent. Deactivation during the reaction was proved to be caused by the formation of the coke on the surface and it can be fully removed by calcination in air at 400 °C. A milder regeneration method in a solution of 35 wt.% hydrogen peroxide performed at 90 °C for 22 h did not result in sintering of the catalytic shell and provided full recovery of the catalytic properties. As a result, a RF-heated composite core-shell catalysts provide a promising way for direct amide synthesis with easy catalyst regeneration and magnetic separation.

Chapter 6

Synthesis and sulfation of NiFe$_2$O$_4$@SiO$_2$@TiO$_2$ core-shell-shell catalysts for direct amide synthesis under RF heating

6.1 Introduction

As mentioned in section 1.5.2, a direct contact between the magnetic core and TiO$_2$ layer might decrease the catalytic activity. Even though the NiFe$_2$O$_4$@TiO$_2$ catalysts (T3 CMC) demonstrated good specific heating rate and high initial catalytic activity in the amide synthesis, the catalytic activity can be further promoted by synthesizing a middle layer between the magnetic core and the catalyst layer to avoid the interaction. The structure with two shells can also provide a better protection for the cores, enhancing the chemical resistance. SiO$_2$ which has several advantages like good thermal and chemical resistance, being easily functionalised as presented in section 1.5.2, is the common material to be chosen as the middle shell [202-204]. Besides the addition of a middle layer, another way which was shown to improve the catalytic activity is the sulfation of TiO$_2$. Thus a proper method to introduce the sulfate groups onto core-shell catalysts with different morphology needs to be explored.

Following these ideas, the core-shell-shell composite magnetic catalysts (T4 CMCs) containing NiFe$_2$O$_4$ core, a SiO$_2$ middle layer and a TiO$_2$ outer layer were synthesized. The method to sulfate both T3 and T4 CMCs was explored in this chapter as well. The obtained CMCs were characterized with XRD, SEM, VSM, TPO, N$_2$ adsorption/desorption isotherms and SAR measurement. Their catalytic activities were measured in the RF-CR to study the effect of the addition of the middle layer and the sulfation treatment.

6.2   Synthesis of core-shell-shell NiFe$_2$O$_4$@SiO$_2$@TiO$_2$ composite magnetic catalysts

6.2.1   Determination of calcination condition

To verify the effect of the addition of the middle layer, a core-shell-shell CMC with a nominal composition of 11 wt.% SiO$_2$ and 14 wt.% TiO$_2$ was synthesized. As new layer was added, the calcination condition including the temperature and dwell time should be optimized to remove all the surfactants. To identify an appropriate calcination temperature, the as-synthesized T4 CMC was studied by TPO (Figure 6.1). The main peak of H$_2$O observed at 250 °C was assigned to the desorption of chemically bonded water. The CO$_2$ profile shows several peaks at temperature of 263, 387 and 500 °C respectively, indicating several types of carbon species. After staying at 500 °C for 40 min, all the residue of H$_2$O and CO$_2$ were totally removed, thus calcination at 500 °C for 40 min was the essential condition to burn out the surfactants into T4 CMC.

To study the effect of calcination time, T4-17-RT CMC was then calcined at 500 °C for 1 and 2 h respectively. It was observed that its surface area sharply decreased from 48.8 to 11.1 m^2/g after an additional period of 1 h. This was possibly due to the sintering caused by exposing at the high temperature for a long time, which was also observed in the regeneration process of T3 CMC. Thus, calcination at a rate of 1 °C min^{-1} to 500 °C and a dwell time of 1 h was enough to burn out all the organic compounds in as-synthesized CMC and keep the relative high surface area at the same time.
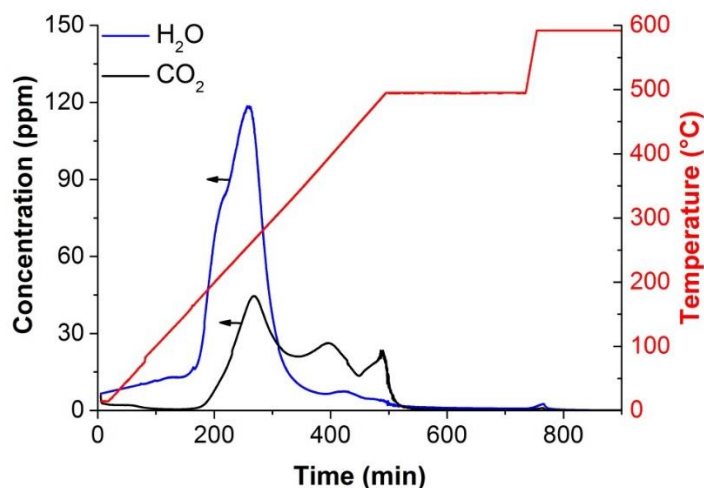
Figure 6.1 CO_2 and H_2O profiles of the as-synthesized T4-17-RT CMC in TPO

6.2.2 Characterization of physical properties

The elemental composition of T4 CMC was analysed by EDS. The detected elements and corresponding weight fraction are shown in Table 6.1. The existence of silicon indicated the successful coating of the silica on the magnetic core. Calculated from weight fraction of elements, the loadings of SiO_2 and TiO_2 in T4 CMC were 13 wt.% and 17 wt.% respectively, which was in good agreement with their nominal values of 11% and 14%. It can be deduced that there was no loss of the precursors during the synthesis. The material composition can be precisely controlled by this synthetic method.

Table 6.1 Elemental analysis of T4 CMC by EDS

	O	Fe	Ni	Ti	Si
T4-17-500 (wt.%)	39.1	34.0	10.8	10.0	6.0

The shape of T4-17-500 nanoparticles was studied with TEM (Figure 6.2). The average dimensions of $NiFe_2O_4$ cores remained around 50 nm, which was as the same as that in the initial $NiFe_2O_4$ particles, indicating there was no solid-state reaction between $NiFe_2O_4$ and silica during calcination steps. The thickness of the shell around the $NiFe_2O_4$ cores was about 20-30 nm.
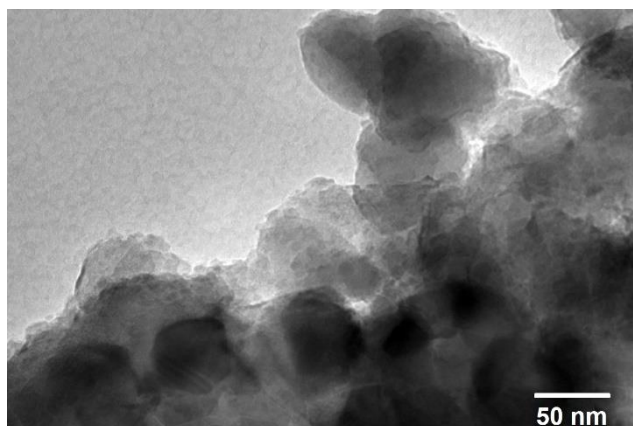
Figure 6.2 TEM image of T4-17-500 CMC

Analysis of crystal phases contained in T4-17-500 CMC was performed by XRD. A reference spectrum of T3 CMC with the same TiO_2 content is presented in Figure 6.3 for comparison. The peaks at 30.7, 36.0, 37.6, 43.8, 54.8, and 64.4 °2θ were assigned to $NiFe_2O_4$ and anatase phase showed peaks at 25.4 and 48.2 °2θ. The peaks representing α-Fe_2O_3 as the impurity appeared at 31.4 and 41.3 °2θ. The peaks of T4-17-500 CMC were exactly the same as those in the XRD pattern of T3 CMC and no peaks of silica were observed in the pattern. As silicon was detected by EDS, the absence of the peaks representing silica layer in the XRD spectrum demonstrates that the silica was amorphous in T4 CMC. The crystal size of $NiFe_2O_4$ nanoparticles in each sample was estimated from the (311) peak at 36.0 °2θ by the Scherrer equation (Eq. (3.5)). The crystal sizes of $NiFe_2O_4$ in the T4-17-500 and T3-17-500 CMCs were the same, demonstrating the good thermal stability of $NiFe_2O_4$ core (Table 6.2).
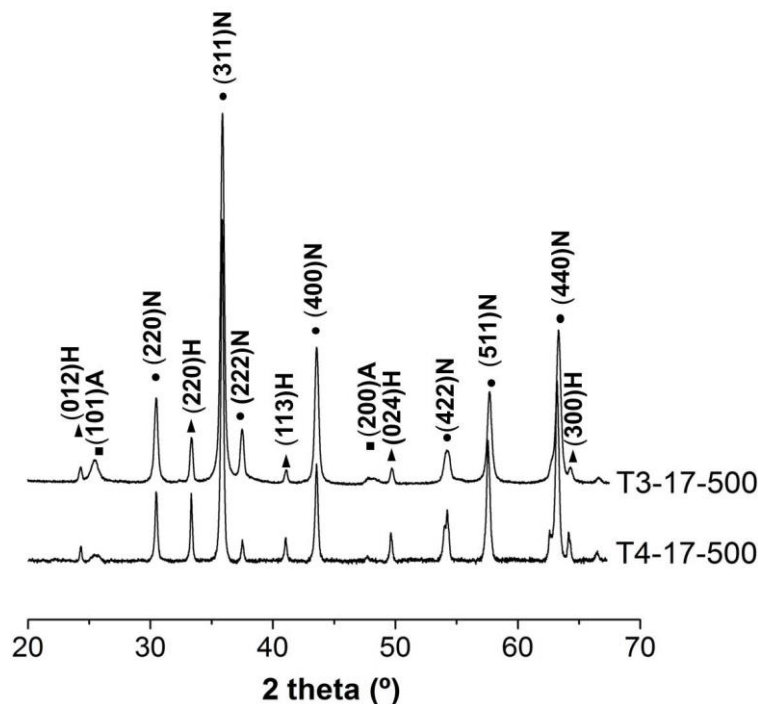
Figure 6.3 XRD patterns of T3-17-500 and T4-17-500 CMCs. The peaks are assigned to (N) $NiFe_2O_4$ (A) anatase titania (H) hematite Fe_2O_3

The hysteresis curve of T4-17-500 is presented in Figure 6.4 and that of T3-17-500 with the same TiO_2 content is also shown as the reference. As the heating property of CMC is related to the hysteresis area, it can be seen from Table 6.2 that the hysteresis area of T4-17-500 CMC was slightly higher than that of T3 CMC, indicating the heating ability increased even with the addition of SiO_2 layer. The increase of the heating property was due to the extra calcination step at 700 °C after the coating of the core with silica gel. The increase of the total calcination time enhancing the magnetism was also observed in other studies [205, 206]. The change of the heating property was verified by the SAR of each sample shown in the same table.

The surface area of T4-17-500 CMC was higher than that of T3-17-500 CMC due to the additional middle layer. The surface area of $NiFe_2O_4@SiO_2$ which was the material before coating of the TiO_2 gel was 33.1 m^2/g. The surface area of TiO_2 layer in the T3-17-500 CMC and T4-17-500 CMC could be calculated based on the surface area and weight fraction of each component (Eq. (4.1)). The obtained values were 136.3 and 125.9 m^2/g for T3-17-500 and T4-17-500 CMCs respectively. A small difference between these values

109

was due to the experimental error. It can be seen that the surface area of the catalytic layer in T3 and T4 CMCs was much higher than the value of TiO_2 in T2 CMC (made by ball mill), proving the superior properties of CMCs synthesized by sol-gel method.
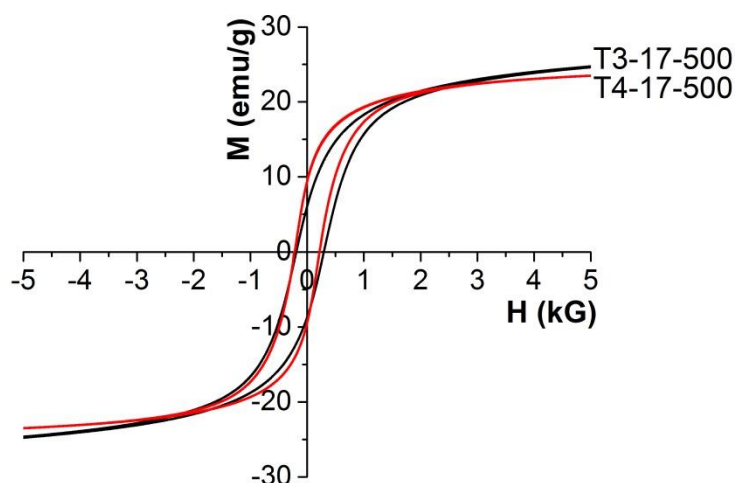
Figure 6.4 Hysteresis curves of T3-17-500 and T4-17-500 CMCs

Table 6.2 Physical properties of $NiFe_2O_4@SiO_2$ composite, T3-17-500 and T4-17-500 CMCs

	Surface area (m^2/g)	Surface area of TiO_2 layer (m^2/g)	Hysteresis loop area (J/g)	SAR (W/g)	Crystal size of $NiFe_2O_4$ (nm)
T3-17-500	25.0	136.3	0.43	1.1	52
T4-17-500	48.8	125.9	0.51	1.5	51
$NiFe_2O_4@SiO_2$	33.1	n.d	n.d	n.d	n.d

n.d – not determined

6.2.3   Catalytic activities

The catalytic activities of the T3-17-500 and T4-17-500 CMCs were measured in the reaction between 4-phenylbutyric acid and aniline in the RF-CR with a 5 mm catalytic bed. As SiO_2 might also contribute to the catalysis, a blank experiment with a $NiFe_2O_4@SiO_2$ sample was carried out to determine its catalytic activity. As it is shown in Table 6.3, the rate constant catalysed by T4-17-500 CMC was 1.9 times higher than that of T3-17-500 CMC. However without the TiO_2 layer, the catalytic activity of $NiFe_2O_4@SiO_2$

was nearly an order of magnitude below than that of titania-containing samples, indicating SiO_2 did not contribute to accelerate the reaction. To diminish the difference brought by the change of the surface area, the production rate was normalized by the surface area of the TiO_2 layer in T3 and T4 CMCs. The data represented in Table 6.3 showed that the specific production rate of T4-17-500 CMC of 16.0 µmol $(m-TiO_2)^{-2}$ s^{-1} was still 1.6 times higher than that of T3-17-500 CMC of 9.9 µmol $(m-TiO_2)^{-2}$ s^{-1}. The deactivation extent of the T4 CMC also slowed down, which might be due to the less contact area between magnetic core and bulk solution because of the double-shell protect. In conclusion, the negative effect of the direct contact between the nickel ferrite core and TiO_2 layer on catalytic activity was verified, and the addition of SiO_2 middle layer can eliminate this negative effect.
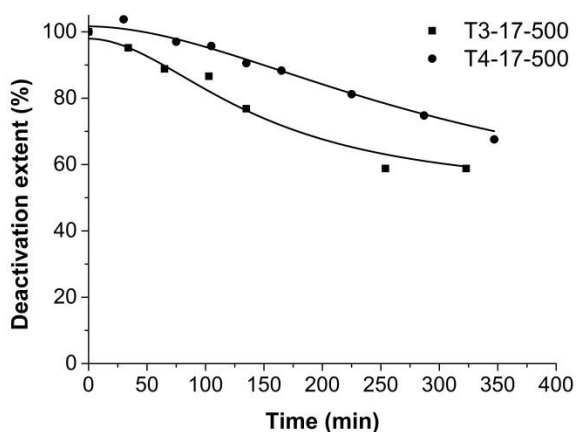
Figure 6.5 Deactivation extent of direct amide synthesis as a function of time over T3-17-500, T4-17-500 CMCs. Reaction conditions: 50 mmol/L 4-phenylbutyric acid and 50 mmol/L aniline, total flow rate 40 µL/min, 320 mg CMC, 150 °C, 7 bars

Table 6.3 Production rates and initial rate constants of direct amide synthesis over T3-17-500 and T4-17-500 CMCs and $NiFe_2O_4@SiO_2$ composite material in the RF-CR

	Initial rate constant $(L\ mol^{-1}s^{-1})$	Production rate (µmol g^{-1} s^{-1})	Specific production rate x 10^{-4} (µmol $(m^{-2}-TiO_2)\ s^{-1}$)
T3-17-500	0.040	0.023	9.9
T4-17-500	0.074	0.034	16.0
$NiFe_2O_4@SiO_2$	0.003	0.002	-

6.3   Sulfation of T3 and T4 CMCs

As sulfation was shown to increase the catalytic activity of TiO_2 catalysts in the direct amide synthesis, both T3 CMC having 32 wt.% TiO_2 as the optimal core-shell CMC and T4 CMC were sulfated using a similar approach to further improve their catalytic activities. Two different sulfation procedures were studied. In the first method, sulfation was done by mixing the calcined samples with sulfuric acid solution, followed by drying and calcination steps to strengthen the bond between sulfate ions and catalyst surface. As sintering of the catalytic layers was observed during the calcination, in the second approach, the sulfation was performed on the as-synthesized T3 and T4 CMCs to realize the burning out of the surfactants and strengthening the attachment of the sulfate groups in a single calcination step. The effect of these methods on physical properties and the catalytic activities of the obtained samples were studied.

6.3.1   Characterization

The surface area of the T3 and T4 CMCs sulfated by the first method was 42.9 and 33.8 m^2/g, which were lower than those in the initial T3-32-500 and T4-17-500 CMCs (51.9, 48.8 m^2/g respectively). It suggests the additional calcination step resulted in a noticeable decrease in surface area, which agreed with the results obtained in the regeneration study of T3 CMC and in the calcination study performed over T4 CMC. Thus to decrease the calcination step in the process from as-synthesized to sulfated CMC, calcination procedures aiming on removing the surfactants and strengthening the bond between sulfate group and Ti cations respectively was merged into one step.

Thus in the second sulfation approach, instead of using the prepared CMC, the as-synthesized CMC was treated with the sulfuric acid solution. Different from the results of the first approach, the surface area of both sulfated T3 and T4 CMCs increased significantly as compared to the unsulfated samples, which were 58.7 and 71.7 m^2/g respectively. The increase might be attributed to the leaching of surfactants when mixing with the sulfuric acid

solution. This hypothesis was speculated from the small bubbles appearing in the suspension and big shallow holes observed on the surface of bulk samples after calcination. The elemental analysis data demonstrated that both sulfation procedures led to the slight loss of shell material and the second route resulted in a relatively lower weight fraction of the shell material due to the partial dissolution of unaged gel into the aqueous solution.

All the SARs of CMCs sulfated by the second method were lower than the respective SARs of unsulfated CMCs, which was might due to the slight corrosion of magnetic core by sulfuric acid. The slow leaching of the $NiFe_2O_4$ material was previously observed in the acidic solution with a pH of 2 [207], while the pH of the sulfuric acid solution used in the present study was 1.7.

As one more calcination step involved in the first sulfation method and longer calcination procedure could result in the better heating property [54, 205], the SAR of T4a-16-500-S CMC increased compared to that in the initial CMC. The decreased SAR of T3a-26-500-S CMC might be explained by the weaker protection of the core by a single TiO_2 layer, thus the positive effect on heating property brought by the calcination was diminished by the leaching (Table 6.4).

Table 6.4 Physical properties and elemental analysis of sulfated T3 and T4 CMCs

	Surface area (m^2/g)	SAR (W/g)	TiO_2 (wt.%)	SiO_2 (wt.%)
T3a-26-500-S	42.9	0.56	26	0
T3b-25-500-S	58.7	0.84	25	0
T4a-16-500-S	33.8	1.94	16	12
T4b-14-500-S	71.7	1.08	14	9

6.3.2 Catalytic activities

Catalytic activities of sulfated T3 and T4 CMCs were tested in the reaction between 4-phenylbutyric acid and aniline in RF-CR with a 5 mm catalytic bed. Even though the TiO_2 content in each CMC decreased after sulfation

treatment, the catalytic activity of TiO_2 was enhanced by sulfation of T3 and T4 CMCs in both methods according to the specific production rate (Table 6.5). The rate constants over all sulfated catalysts showed an improvement compared to the value over unsulfated ones except T3a-26-500-S. The rate constant over T3a-26-500-S dropped slightly compared to the value over unsulfated one. The effect was less pronounced over T3a-26-500-S due to its decreased surface area as well as the decrease of TiO_2 loading.. The T3 and T4 CMCs sulfated by the second route demonstrated much better catalytic activity. The rate constants were improved by 33% and 116% over the sulfated T3 and T4 CMCs respectively. The difference was attributed to the smaller decreasing extent of surface area of T4 CMC after sulfation compared to that of T3 CMC.

Table 6.5 Specific production rates and rate constants of direct amide synthesis over unsulfated and sulfated T3 and T4 CMCs

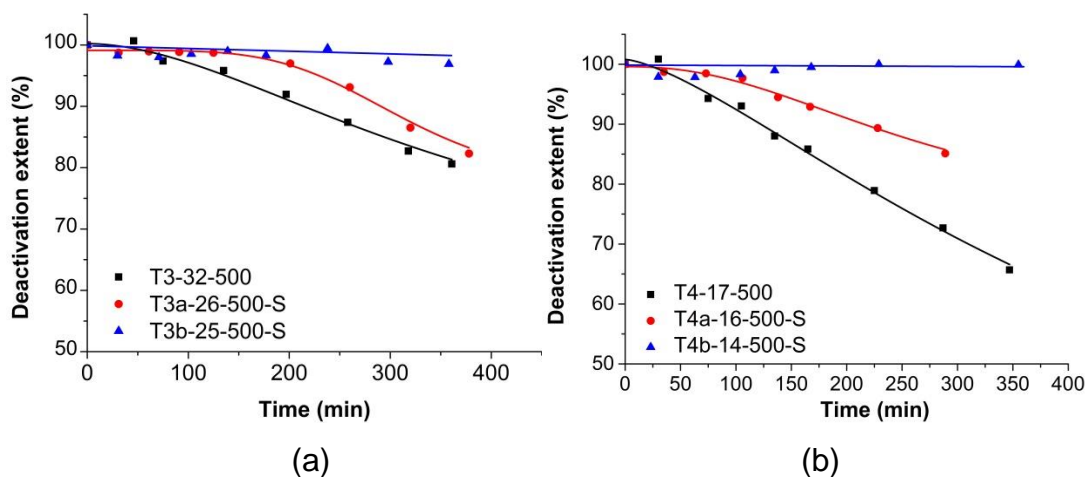|	Initial rate constant $(L \cdot mol^{-1} s^{-1})$	Specific production rate $(\mu mol\ (g\text{-}TiO_2)^{-1} s^{-1})$
T3-32-500	0.15	0.15
T3a-26-500-S	0.14	0.18
T3b-25-500-S	0.20	0.22
T4-17-500	0.074	0.21
T4a-16-500-S	0.12	0.28
T4b-14-500-S	0.16	0.37

(a)   (b)

Figure 6.6 Deactivation extent of direct amide synthesis over sulfated and unsulfated (a) T3 and (b) T4 CMCs. Reaction conditions: 50 mmol/L 4-phenylbutyric acid and aniline, total flow rate 40 μL/min, 320 mg CMC, 150 °C, 7 bars

The specific production rate based on TiO_2 weight for T3b-25-500-S CMC was 0.22 μmol $(g\text{-}TiO_2)^{-1}$ s^{-1}, which was lower than that of T4b-14-500-S CMC at 0.37 μmol $(g\text{-}TiO_2)^{-1}$ s^{-1}. This again verified the SiO_2 layer was necessary to avoid the interaction between magnetic and catalytic part. According to Figure 6.6, the deactivation with time became smaller for the sulfated catalysts. No deactivation of CMC was observed over both T3 and T4 CMCs obtained by the second sulfation method for a time on stream of 8 h. The improvement on the deactivation extent was possibly due to the change of the acid sites strength leading to the different bonding of reactants and water on the surface. In conclusion, by sulfation of the as-synthesized CMC with core-shell like structure, the catalytic activity was promoted on a large scale and no deactivation occurred on sulfated CMCs.

The comparison between the catalytic activity of the optimal sulfated titania P25-7.5S in the batch reactor and that of T4b-14-500-S can be verified by the value (k_m) of the initial rate constant (k) normalized by the catalyst concentration (C_{cat}) in the reactor. The catalyst concentration was the ratio of the mass of the titania to the liquid volume in the reactor.

$$k_m = k / C_{cat} \tag{6.1}$$

Under the same reaction temperature at 150 °C, the k_m of the reaction in the batch reactor over P25-7.5S catalyst was 1.6 x10^{-4} L^2 $mol^{-1}(g\text{-}TiO_2)^{-1}s^{-1}$,

while the value over T4b-14-500-S was 3.9 $\times 10^{-4}$ L^2 $mol^{-1}(g\text{-}TiO_2)^{-1}s^{-1}$. The value was doubled in the RF-CR packed with the optimal magnetic catalyst T4b-14-500-S due to the much higher surface area of the titania layer on the magnetic catalyst and the direct heat transfer to the active sites during RF heating.

6.3.3 In-situ regeneration of T4 CMC in the RF-heated continuous reactor

As TiO_2 contained in the T4b-14-500-S CMC had a better catalytic activity and no deactivation was observed for 8 h, its catalytic activity was further tested in longer experimental runs to study the deactivation kinetics. As it can be seen from Figure 6.7, the catalytic activity of T4b-14-500-S CMC reduced by 43% after 55 h. As T3 CMC could be totally recovered by mixing the spent CMC with 35 wt.% H_2O_2 in the batch reactor at 90 °C, to regenerate T4b-14-500-S, an in-situ regeneration procedure was developed in the RF-heated continuous reactor instead of using a separate procedure in a batch reactor.

The regeneration was performed with a flow of iso-propanol at 1 mL/min flow rate to flush the reactant residues substrates for 10 min. Then a 35 wt.% H_2O_2 solution was fed at a flow rate of 100 µL/min and temperature was maintained at 90 °C under RF heating. After 22 h, the reactor was fed with another 10 mL iso-propanol to wash over the residue H_2O_2 solution. Then, the inlet solution was changed to 0.05 M 4-phenylbutyric acid and aniline in p-xylene, and a new reaction cycle started.

The initial rate constants tested for first and second regenerated CMCs were 0.16 and 0.15L $mol^{-1}s^{-1}$, indicating the catalytic activity of the spent CMC could be totally recovered to the activity of the fresh one in the flow reactor. The deactivation extents over the fresh and regenerated catalysts are shown in Figure 6.7. The deactivation process started to accelerate after each regeneration process, which was also observed in the regeneration of ball milled CMCs (Section 4.5). The catalytic activity reduced by 54% after the first regeneration run and by 64% after the second regeneration run. It was due to the change of the catalyst pore size during the RF heating, which had

116

been verified by the N_2 adsorption/desorption isotherms study of regenerated T2 and T3 CMCs.
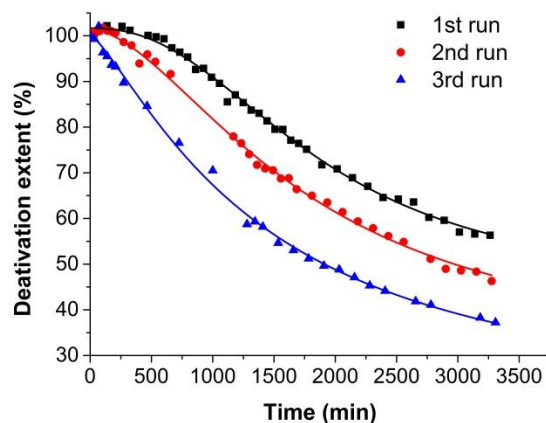

Figure 6.7 Deactivation extent of direct amide synthesis as a function of time over fresh and regenerated T4b-14-500-S CMCs. Reaction conditions: 50 mmol/L 4-phenylbutyric acid and 50 mmol/L aniline, total flow rate 40 µL/min, 320 mg CMC, 150 °C, 7 bars

This in-situ flow regeneration method has several advantages compared to the conventional regeneration of catalyst in the flow reactor. Normally, the spent catalysts in the flow reactor had to be taken out and treated in an external vessel before the next operation. During the external process, it is easy to cause the irreversible mechanical deactivation of the catalyst [208]. Also additional cost on equipment and labour was generated. In the flow regeneration protocol, the magnetic catalyst could be fully recovered in the flow reactor, avoiding the attrition and possible bed densification during and after the regeneration. This facile operation also brought convenience and saved cost for the regeneration step.

6.4 Comparison of magnetic catalysts with different morphologies

In summary, to apply the catalysts to the reactor under RF heating, there exist four routes to combine the magnetic particles with the active catalysts. The most facile way is a mechanical mixture of magnetic and catalytic particles. However, the independence of two types of the particles made the separation procedure hard to achieve by only magnet. The TiO_2 particles

needed to be recycled by the extra filtration or centrifugation, which would still increase the separation cost. To make uniform magnetic catalyst, ball mill is the simplest way and it is suitable for fast scale-up. The production rate of the ball milled T2 CMC was nearly the same as the mechanical mixture case T1 CMC, which again verified the catalytic activity was not affected by ball milling. However, deactivation behaviour of T2 CMC was not as good as those in the mechanical mixture. This was due to larger contacting area between $NiFe_2O_4$ nanoparticles and the active TiO_2 phase, resulting in the adsorbed reaction species on the surface overheated.

The CMC having a core-shell structure demonstrated a better catalytic activity under RF heating. This CMC had a good chemical resistance, uniform structure and much higher surface area. As a result, the production rate considerably increased as compared to that over the T1 and T2 CMCs. Also there was no deactivation in the initial period, which might be attributed to shorter reaction time on the surface once acid sites changed. A further improvement was made with a protective silica middle layer and a sulfated TiO_2 layer (T4 CMC). Compared to T3 CMC, this CMC demonstrated enhanced activity and stability. The ranking of different CMCs from different aspects is listed in Table 6.6.
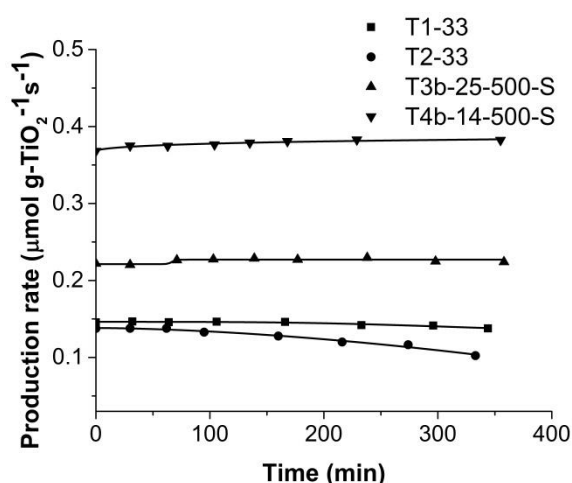

Figure 6.8 Production rates of direct amide synthesis as a function of time over CMCs with different structures. Reaction conditions: 50 mmol/L phenylbutyric acid and 50 mmol/L aniline, total flow rate 40 µL/min, 320 mg CMC, 150 °C, 7 bars

Table 6.6 Comparison of CMCs with different morphology

	T1 CMC	T2 CMC	T3 CMC	T4 CMC
Surface area	-	-	+	++
Heating rate	+++	++	+	++
uniformity	none	good	good	good
Recycling method	filtration & magnetic separation	magnetic separation	magnetic separation	magnetic separation
Chemical resistance	-	-	+	++
Catalytic activity	+	+	++	+++
Catalytic stability	+	-	++	+++
Scale-up	++	+	-	-

"-" = not good; "+" = good; "++" = better; "+++" = best

6.5 Conclusions

The core-shell-shell CMC was successfully synthesized. The calcination at 500 °C for 1h was needed to remove all the surfactants in the as synthesised CMC. The middle SiO_2 layer was amorphous and showed nearly no catalytic activity in the reaction between 4-phenylbutyric acid and aniline. Both the heating rate and surface area were increased resulting in a much higher catalytic activity of the T4 CMC as compared to that of T3 CMC having the same TiO_2 loading. More importantly, the production rate normalized by the amount of TiO_2 was enhanced, verifying the negative effect of magnetic core on catalytic layer.

The catalytic activity was further promoted by sulfation of T3 and T4 CMCs. The sulfation of as-synthesized T3 and T4 CMCs provided better catalytic activity as it reduces additional high temperature calcination step which prevents the shrinkage of surface area. No deactivation of both sulfated T3 and T4 CMCs was observed in the first 6 h on stream in a flow reactor under RF heating. An in-situ regeneration method was developed for the sulfated T4 CMC and the activity could be totally recovered. Different aspects of four

kinds of CMCs were compared and it was concluded that the T4 CMCs with core-shell-shell structure demonstrated the best performance among all studied catalysts. The deactivation rate of T4 CMC was an order of magnitude below than that over ball milled catalysts and the catalytic activity could be totally recovered using a specially developed flow regeneration protocol. However the deactivation rate was found out to be accelerated after each regeneration cycle.

Chapter 7

Design and operation of an RF-heated continuous reactor

7.1 Introduction

Even though a series of different CMCs were successfully synthesized for the application in the direct amide synthesis under RF heating, to realize the possibility of reactor scaling up and bench scale applications, a proper design methodology for the RF-heated continuous reactor is needed. As RF heating is a volumetric heat generation method, usually there exists a large temperature gradient along the reactor, making it difficult to maintain near isothermal conditions often required for applications in fine chemicals synthesis. A near isothermal condition of RF-CR could be achieved by application of a structured catalytic bed where catalyst zones are separated with additional heating zones of different lengths as shown in section 1.7.2. However this design is limited to a narrow range of flow rates and it lacks the flexibility and simplicity to be further adopted by the industry. Therefore, a further study devoted to an isothermal reactor design has been performed to simplify the packing procedure and extend the range of possible operating conditions.

In this chapter, a near isothermal RF-CR system with a 20 mm CMC packed bed will be discussed and two different operation methods to control the RF-CR will be presented. After near isothermal operation is achieved, the kinetic study of reaction between 4-phenylbutyric acid and aniline over CMCs containing sulfated TiO_2 in the RF-CR is presented as well. To study the effect of oscillating temperature, temperature modulation was conducted in the RF-CR with a 5 mm catalytic bed.

7.2   Design of an isothermal RF-heated continuous reactor

To realize the isothermal regime which can be easily achieved at any conditions, a reactor with separately controlled preheating and catalytic zones was developed. If the inlet stream is heated up to the desired temperature in a preheating zone, then the temperature will be kept at the same value once the heat generated in the catalytic zone is equal to the heat loss to the environment. In this approach, the temperature could be maintained in an acceptable range around the target temperature by adjusting the heat generation term. As the heat generated in both zones can be adjusted, the isothermal state can be achieved under different reaction conditions simply by adjusting the RF power.

The RF-CR with the reaction temperature controlled by a PID controller as described in section 2.6 was firstly developed. Once the target temperature was input, the controller could automatically adjust the RF power to stabilize the temperature at the desired value according to the real-time temperature feedback. To realize the near-isothermal state, the length of the preheating zone was adjusted so that the temperature of the liquid was close to the reaction temperature at the exit from the preheating zone. The temperature in the first 5 mm length of the catalytic bed was precisely controlled by the PID controller. In this approach, the length of preheating zone inside the magnetic field was the only parameter needed to be adjusted.

To study a possibility to run reactors with different lengths of catalytic bed at near isothermal conditions, three reactors with a catalytic bed length of 10, 15, 20 mm were assembled. The T2-50 CMC was placed in the catalytic bed and Fe_3O_4 pellets were packed in a 35 mm preheating section. The flow rate was changed with the amount of the catalyst in various catalytic beds to keep the same WHSV of 4.3 μL $g^{-1}s^{-1}$. Reaction conditions for each RF-CR are listed in Table 7.1.

Table 7.1 Reaction conditions for RH-CR with different catalytic bed lengths

Length of catalytic bed (mm)	Mass of T2-50 (mg)	Flow rate (µL/min)
10	549	142
15	805	200
20	1130	300

When the temperatures of the preheated stream and first 5 mm zone of the catalytic bed were kept at 150 °C, a drop of the temperature along the reactor length was observed in each experiment. The phenomenon indicated the heat loss via the structural zone packed with the glass beads contributed a substantial fraction of the overall heat loss, resulting in the increased heat loss along the reactor. As the rate of heat generation is the same in each section of the catalytic bed, the generated heat which was equal to the heat loss at the initial section could not compensate the heat loss at the end. As it can be seen in Figure 7.1, the temperature gradient in the 10 mm catalytic bed was 3 °C, which was acceptable and could be regarded as being isothermal. Nevertheless, the temperature gradient increased to 10 and 15 °C as the length of catalytic bed was extended to 15 and 20 mm respectively. In order to compensate the larger heat loss in the end section, a larger RF power should be provided. Since RF power was adjusted automatically by the PID controller in this system, it was hard to increase the RF power to the precise value needed, demonstrating the inflexibility of this PID assisted two-point controlled RF-CR. The temperature profile in a 20 mm catalytic bed in the RF-CR without preheating zone was also measured for comparison. The temperature gradient over the first 10 mm zone reached over 50 °C and then the temperature decreased because of the conduction heat loss via the structural zone. Even though isothermal conditions were not achieved by this PID assisted two-point controlled RF-CR with the catalytic bed longer than 10 mm, the temperature gradient was still significantly reduced compared to the reactor without the preheating zone.
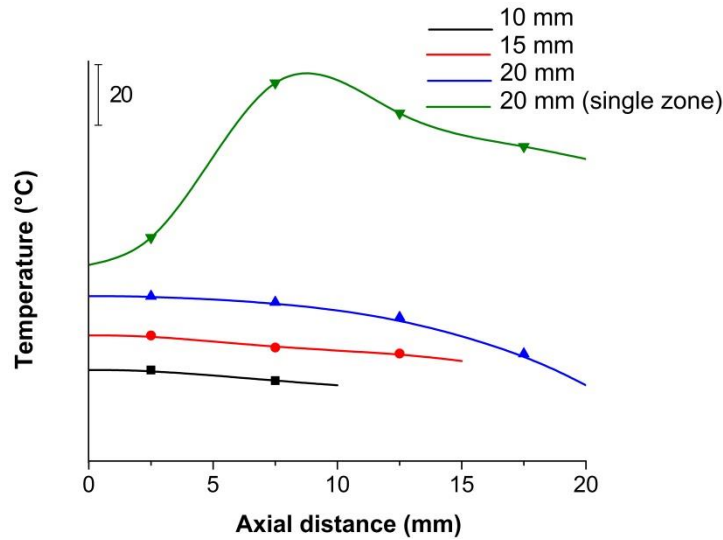
Figure 7.1 Temperature profiles in the 10, 15, 20 mm catalytic beds in the PID assisted two-point controlled RF-CR. Temperature profile of RF-CR with a single catalytic zone was presented as the reference. All the profiles started at 150°C and were shifted upwards for clarity.

In an attempt to precisely control the heat generation in the preheating and catalytic zones, both the length of preheating section inside the RF coil and current supplied should be controlled manually. The length of the preheating section could be determined from the temperature of the inlet flow while the ideal heating rate of the CMCs packed in the catalytic bed was hard to be determined due to the uneven heat loss along the reactor.
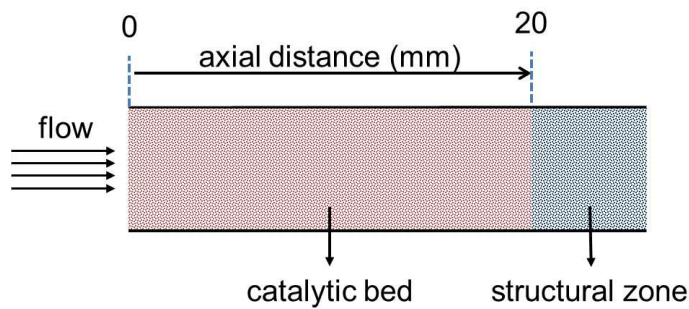

Figure 7.2 Schematic image of the reactor model

In order to study the temperature profiles under various RF powers supplied in the catalytic bed, a simplified model of the 20 mm heated catalytic bed with a 5 mm structural zone in RF-CR was simulated in the COMSOL Multiphysics (Figure 7.2). In this model, the fluid flow in the catalytic bed was modelled by the Brinkman equation (Eq. (7.1)) for the flow in porous media.

The heat transfer in the porous media with non-compressible flow was simulated using Eq. (7.2). The catalytic bed was set as the heating source and the volumetric heating rate (Q_h) was adjusted to study the variation of the temperature profiles. The temperature of the inlet stream was set at 150 °C. The parameters input in the COMSOL are listed in Table 7.2.

$$(\mu \kappa^{-1} + \beta_F |v| + \frac{\rho \nabla v}{\varepsilon_p^2})v = \nabla \cdot \left[-pI + \mu \frac{1}{\varepsilon_P}(\nabla v + (\nabla v)^T) \right] - \frac{\mu v}{\kappa} \qquad (7.1)$$

$$\rho C_p v \nabla T = \nabla(\lambda_{eff} \nabla T) + Q_h + U(T - T_0) \qquad (7.2)$$

Table 7.2 Physical properties of the reactor and the fluid phase

	Parameters	Symbol	Value
Configuration of the reactor	Catalytic bed length (mm)	L_c	20
	Structural zone length (mm)	L_s	5.0
	Inner radius (mm)	r_1	3.3
	Outer radius (mm)	r_2	5.5
	Thickness of the insulation (mm)	d_i	7
Calculated parameters	Porosity	ε_p	0.65
	Permeability (m^2)	κ	$5.3*10^{-10}$
	Overall heat transfer coefficient (W m^{-2} K^{-1})	U	10.9
	Superficial velocity (m/s)	v	0.0007
P-xylene (fluid) at 150 °C	Density (kg m^{-3})	ρ_f	741
	Heat capacity (J kg^{-1} K^{-1})	$C_{p,f}$	1710
	Thermal conductivity (W m^{-1} K^{-1})	λ_f	0.1
	Dynamic viscosity (Pa s)	μ_f	0.002
Nickel ferrite (catalytic bed)	Density (kg m^{-3})	ρ_n	5390
	Heat capacity (J kg^{-1} K^{-1})	$C_{p,n}$	620
	Thermal conductivity (W m^{-1} K^{-1})	λ_n	6.2
Glass bead (structural zone)	Density (kg m^{-3})	ρ_g	2200
	Heat capacity (J kg^{-1} K^{-1})	$C_{p,g}$	700
	Thermal conductivity (W m^{-1} K^{-1})	λ_g	1

Besides the parameters mentioned above, in the Brinkman equation, the β_F represents the Forchheimer drag option, which adds a viscous force proportional to the squared fluid velocity. I is referred to the stress invariant. The values of these parameters at each simulated point were automatically

calculated by COMSOL. The velocity of the flow was calculated based on the volumetric flow rate of 1.4 mL/min. The permeability of the bed (κ) which was packed with the spherical particles with homogeneous porosity was calculated from the average diameter of the CMC particles (d_p) of 187.5 µm and the measured bed porosity (ε_p) according to the Eq. (7.3) [209].

$$k = \frac{d_p^{\,2}\varepsilon_p^{\,3}}{150(1-\varepsilon_p)^2} \tag{7.3}$$

The overall heat transfer coefficient (U) was calculated by Eq. (7.4).

$$\frac{1}{Ur_1} = \frac{\ln(\frac{r_2}{r_1})}{\lambda_1} + \frac{\ln(\frac{r_3}{r_2})}{\lambda_2} + \frac{1}{h_3 r_3} \tag{7.4}$$

where r_1 and r_2 are the internal and outer diameters of the reactor respectively, r_3 is the diameter of the reactor with the insulation. The thermal conductivity of the reactor wall (λ_1) and the insulation material (λ_2) are 1.0 and 0.04 W m^{-1} K^{-1} respectively. The natural convection heat transfer coefficient (h_3) is 12.0 W m^{-1}K^{-1} estimated from the correlation for the natural convection around a vertical cylinder. λ_{eff} is the effective thermal conductivity and the value is the weighted arithmetic mean of the fluid conductivity and porous material.

With the change of the volumetric heating rates (Q_h), three typical types of predicted temperature profiles along the catalytic bed are shown in Figure 7.3. If the heat supplied was equal to the minimum heat loss in the first section of the catalytic bed, the temperature constantly decreased towards downstream position due to the additional conduction loss. With the increase of the volumetric heating rate to an optimal value, the temperature stayed nearly constant over the entire catalyst bed with a slight drop observed near the end. If the heating rate was increased further, a parabolic temperature profile was observed, demonstrating substantial conduction losses in the axial direction. Considering all the situations above, a near isothermal operation could be achieved at a specific RF heating rate in the 20 mm catalytic bed.
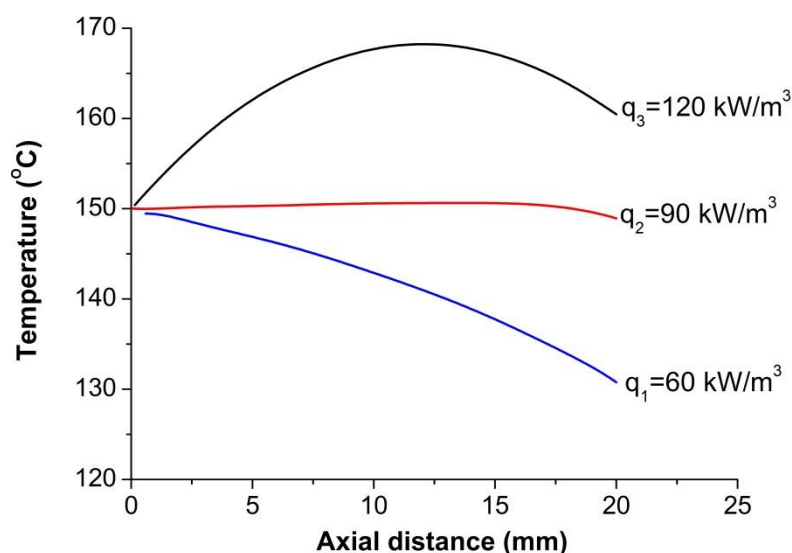
Figure 7.3 Predicted temperature profiles along the catalytic bed under different volumetric heating rates.

The numerical simulation results were further verified in the RF-CR with a 20 mm catalytic bed. In these experiments, the length of the preheating zone in the coil and the RF power (current) were constantly adjusted according to the temperatures along the catalytic bed until reaching the minimum temperature gradient. As it is shown in Figure 7.4, a near isothermal behaviour could be achieved in the temperature range of 120 – 160 °C under certain conditions (Table 7.3). The temperature difference less than 3 °C was also observed in the RF-CR in a wide range of flow rates from 500 to 2400 µL/min, demonstrating the near isothermal regime could be reached at various reaction conditions.

Table 7.3 Optimal parameters for the manually two-point controlled isothermal RF-CR at different temperatures

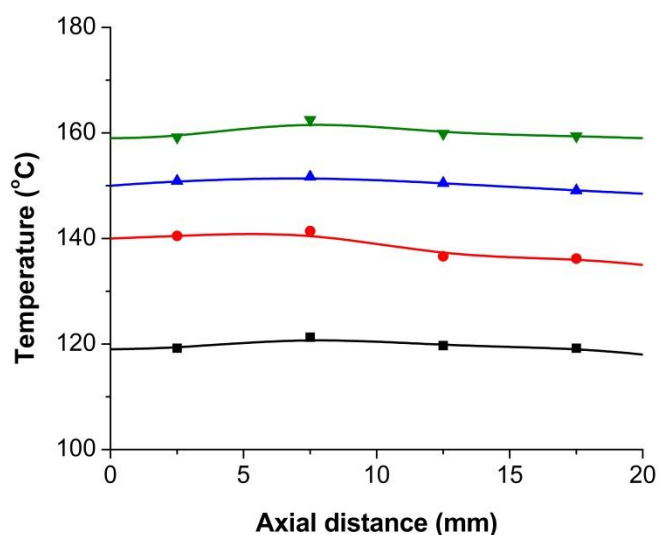| Temperature (°C)	Length of the preheating zone(mm)	Current (A)
120	24.5	84.8
140	30	84.8
150	28	86.4
160	26	92.8

Figure 7.4 Temperature profiles of the 20 mm catalytic bed in the manually two-point controlled RF-CR at different temperatures. Reaction conditions: 50 mmol/L 4-phenylbutyric acid and 50 mmol/L aniline, total flow rate at 1400 µL/min, 1.2 g T2-50 CMC, 7 bars

In short, the near isothermal continuous reactor was developed by manually control strategy with adjustment of the heat generation in the preheating and catalytic zones. The simple structure of the packed bed, facile operation, and flexibility of this method makes it suitable for applications at various conditions and for scaling up to a larger production.

7.3 Kinetics study in the isothermal RF-heated continuous reactor

The production rate of direct amide synthesis over T2-50 CMC was tested in the catalytic bed of 10, 15 and 20 mm at 150 °C. The WHSV was kept at 4.3 µL g^{-1} s^{-1} in all the reactors. The rate slightly increased from 0.10 to 0.14 µmol g^{-1} s^{-1} when the length of catalytic bed was doubled from 10 to 20 mm (Table 7.4), indicating the existence of external mass transfer limitations [210]. When the flow rate was increased from 300 to 500 µL/min, the production rate increased from 0.14 to 0.21 µmol g^{-1} s^{-1}. As the production rate depended on the flow rate, it can be concluded the presence of external mass transfer limitations in the reactor under current reaction conditions.

Table 7.4 Reaction conditions and rates of direct amide synthesis in the isothermal RF-CRs with different lengths of the catalytic bed. Reaction conditions: 50 mmol/L 4-phenylbutyric acid and 50 mmol/L aniline, 1.2 g T2-50 CMC, 150 °C, 7 bars

Length of catalytic bed (mm)	Flow rate (µL/min)	WHSV (µL g^{-1} s^{-1})	Amide yield (%)	Initial production rate (µmol g^{-1} s^{-1})
10	142	4.3	48	0.10
15	200	4.2	53	0.11
20	300	4.5	63	0.14
20	400	5.9	60	0.18
20	500	7.5	57	0.21

To explore the operation conditions where external mass transfer limitations could be presented, the effect of flow on production rate was studied. In these experiments, the flow rate was increased from 0.5 to 2.4 mL/min (Figure 7.5). The production rate increased with the flow rate up to 1.4 mL/min and then remained constant. Thus it can be concluded that the mass transfer limited regime existed below 1.4 mL/min and the reactor should be operated in the kinetic regime above 1.4 mL/min, corresponding to a WHSV of 21.0 µL g^{-1} s^{-1}.
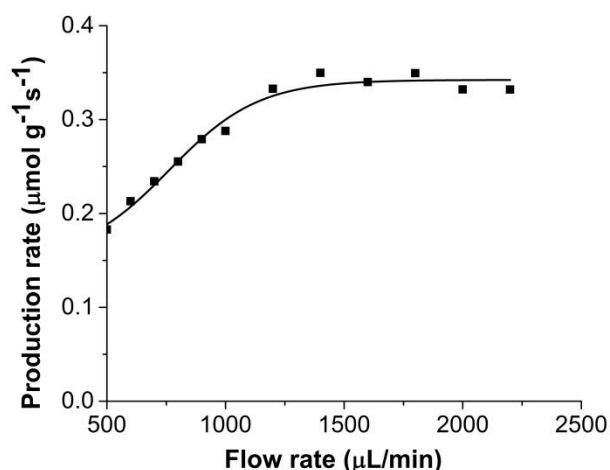

Figure 7.5 Production rates of direct amide synthesis as a function of the flow rate in isothermal RF-CR with 20 mm catalytic bed. Reaction conditions: 50 mmol/L 4-phenylbutyric acid and 50 mmol/L aniline, 1.2 g T2-50 CMC, 150 °C, 7 bars

The next series of experiments were performed with the flow rates in the kinetic regime. The temperature was ranged from 120 to 160 °C and the initial rate constant was calculated to estimate the activation energy by Arrhenius equation. The activation energy calculated from the slope of the curve (Figure 7.6) was 66 kJ/mol, which was the same value as obtained over the P25-7.5S catalyst in the batch reactor. It demonstrated that the intrinsic activity of sulfated TiO_2 remained the same after being deposited onto nickel ferrite nanoparticles by ball mill, which agreed well with the previous study on the catalytic activity of P25-7.5S in T2 CMCs having various titania loadings (section 4.3).
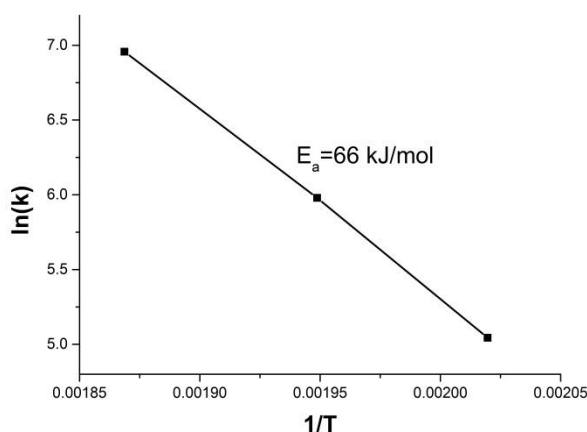

Figure 7.6 Arrhenius plot over T2-50 CMC in the isothermal RF-CR with a 20 mm catalytic bed. Reaction conditions: 50 mmol/L 4-phenylbutyric acid and 50 mmol/L aniline, 1.2 g T2-50 CMC, flow rate 1.4 mL/min , 7 bars

7.4   Transient operation in RF-heated continuous reactor

The theoretically positive effect of transient operation on temperature was put forward as early as 1966 by Lin et al [211]. Nevertheless, due to the thermal inertia caused by the limitation of the equipment, the effect was not experimentally proved until the development of microreactors. In such reactors, the reaction rate of CO oxidation was proved to be enhanced under oscillation temperature conditions [212, 213]. The enhancement mechanism was explained by the difference of the surface coverage of reactants in transient operations compared to the steady state. For conventionally heated reactor, the set-up to temperature modulation even in a microreactor was rather complex. In this way, RF heating could provide an elegant way to

explore this phenomenon experimentally. The highly efficient heat transfer from the magnetic core to the catalyst surface could make the heating time very short. Also very large surface to volume ratio in microreactors provide fast and efficient cooling.

To test the effect of transient operation on the reaction rate of direct amide synthesis, a forced temperature modulation was realized in the RF-CR having a 5 mm catalytic bed. The cooling rate of natural convection allowed a periodic operation. The resulted time-dependent temperature plot is presented in Figure 7.7. With the current in the coil of 140 A, the oscillation amplitude was 20 °C with the mean temperature of 150 °C and the whole period of oscillations was 50 s.
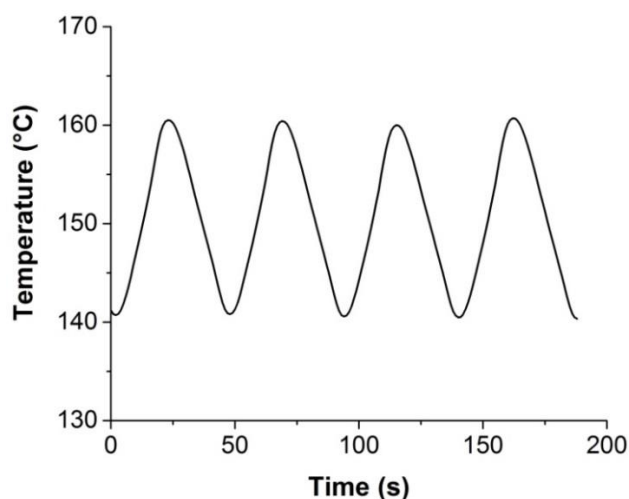

Figure 7.7 Temperature as a function of time in the RF-CR with a 5 mm catalytic bed

However, the apparent initial rate constant of direct amide synthesis under this condition was 0.094 $L \cdot mol^{-1}s^{-1}$, which was much lower than the value of 0.36 obtained under steady state. Also, the CMCs deactivated faster as compared to steady state operation (Figure 7.8). It was also observed that the outlet stream became dark brown, demonstrating the carbonization of organic compounds occurred. The faster deactivation was probably due to the local hot spots as a result of high heating rates to provide fast temperature transitions. The temperature at the surface of CMCs became higher than that at steady state operation, resulting in the decomposition of reactants and coke formation. The decreased rate constant could also be

131

explained by this phenomenon because the amount of the reactants to form the amide reduced under this condition. It can be concluded that transient operation under RF can cause the existence of hot spots and it is only suitable for the chemicals which can resist high temperature.
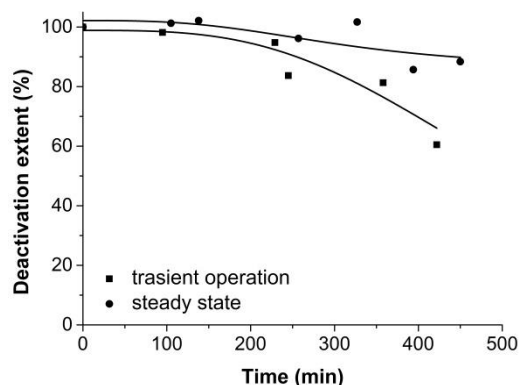

Figure 7.8 Deactivation extent of direct amide synthesis as a function of time in the RF-CR under transient and steady state operations. Reaction conditions: 50 mmol/L 4-phenylbutyric acid and 50 mmol/L aniline, 320 mg T2-50 CMC, flow rate 40 µL/min, 7 bars

7.5 Extension of other amides synthesis in isothermal RF-heated continuous reactor

Besides the reaction between 4-phenylbutyric acid and aniline, the sulfated TiO_2 catalyst was also proved to have good catalytic activities in the amidation of propionic and acetic acids with aniline (Section 3.7.1). Thus to study the production of various amides in this isothermal RF-CR, the production rates with these reactants were studied over T2-50 CMC in the isothermal RF-CR with a 20 mm catalytic bed. As it can be seen from Table 7.5, the production rates of both the acetic acid and propionic acids reacting with aniline were higher than that of 4-phenylbutyric acid in the flow reactor. As their pKa values were nearly the same, the faster production rates of the new reactions might be due to the smaller molecules of the reactants which led to the faster internal mass transfer and increased adsorption rate on the surface. In this way, it should be mentioned that 4-phenylbutyric acid was chosen as a model compound in this thesis as its reaction with aniline had quite high activation energy. If the catalyst demonstrates high catalytic

activity with 4-phenylbutyric acid, it can be deduced that the production rate of the reaction using the acid with smaller pKa values would be increased.

Table 7.5 Throughputs and production rates of various acids reacting with aniline

	pKa	Throughput in RF-CR (g /h)	Production rate ($\mu mol \ g\text{-}TiO_2^{-1} \ s^{-1}$)	
			in batch reactor	in RF-CR
4-phenylbutyric acid	4.76	0.27	0.50	0.62
Acetic acid	4.76	0.26	0.85	1.07
Propionic acid	4.86	0.28	0.74	1.03
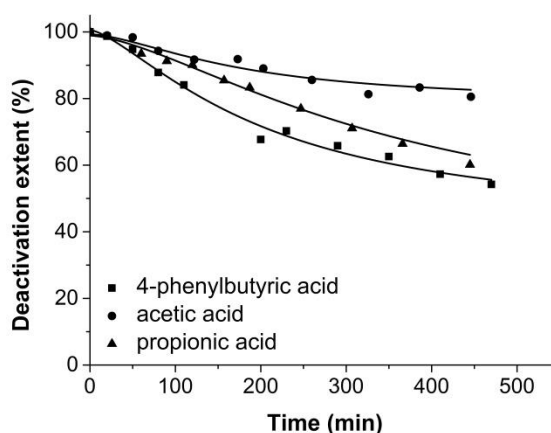
Figure 7.9 Deactivation extent of 4-phenylbutyric acid, acetic acid and propionic acid with aniline as a function of time. Reaction conditions: 50 mmol/L acids and 50 mmol/L aniline, 1.2 g T2-50 CMC, flow rate 1.4 mL/min, 150°C, 7 bars

The developed RF heated continuous reactor showed a higher efficiency compared to the batch reactor due to its good heat transfer and high catalyst loading. Under the same reaction condition, it took only the residence time of 19 s in the RF heated continuous reactor to reach the amide yield of 30% while 5 h was required in the batch reactor to achieve the same yield. To have a proper comparison of the catalytic activity of the titania component, the production rates were normalized by the mass of titania in the batch and continuous modes. The production rates over T2-50 CMC in the RF-CR were higher than the values in the batch reactor for all the reactions (Table 7.5). As the heat was transferred directly from magnetic particles to the acid sites

in the RF-CR, it had a lower temperature gradient than the batch reactor, resulting in an improved production rates. The total throughputs for the 4,N-diphenylbutyramide, N-phenylpropionamide, N-phenylacetamide were 0.27, 0.26, 0.28 g/h respectively, and they were higher than the same reactions conducted in the batch reactor as shown in section 1.2.3. The deactivation extent of T2-50 CMC in the reaction with acetic and propionic acids were observed to be smaller than that with 4-phenylbutyric acid (Figure 7.9). It is worth mentioning that the current throughputs were achieved in the RF-CR catalyzed by ball milled T2-50 magnetic catalyst. The throughput of the product can be further increased by loading the optimal sulfated core-shell CMC in the RF-CR according to the conclusion from Section 6.4.

7.6   Conclusions

A near isothermal operation has been achieved in a two-point controlled RF-CR which could adjust heating power in the preheating and catalytic zones separately. The temperature gradient along a 20 mm catalytic bed at various temperatures and flow rates could be limited to 3 °C, demonstrating the flexibility of this control approach. The production rate was severely limited by external mass transfer at low flow rates. A kinetic regime was observed at the flow rate above 1.4 mL/min in the RF-CR with a 20 mm catalytic bed. The activation energy of the reaction between 4-phenylbutyric acid and aniline over the T2-50 CMC observed in this RF-CR was 66 kJ/mol, which was the same as that over sulfated titania (P25-7.5S) in the batch reactor. It confirmed the constant catalytic activity of the sulfated titania after ball milling. The production rate over T2-50 CMC in the RF-CR was higher than the value in the batch reactor, verifying the efficient heat transfer to the catalytic centres in the RF-CR. The throughput of 4, N-diphenylbutyramide of 0.27 g-CMC/h was achieved in this isothermal RF-CR. The synthesis method was extended to other types of acids and two products were obtained with similar throughputs starting from acetic and propionic acids.

Chapter 8

Conclusions and recommendations

8.1   Conclusions

Direct amide synthesis from acid and amine is a green and one-step approach to produce the amide. Compared to other heterogeneous catalysts, TiO_2 showed the best catalytic activity in the chosen model reaction between 4-phenylbutyric acid and aniline. The catalytic activity of TiO_2 was further promoted by a treatment with sulfuric acid. By the developed sulfation approach, the sulfate groups were evenly distributed on the surface while the morphology and surface area of the titania remained unchanged. Strong Lewis acid sites were formed on the surface after the sulfation and no Brønsted acid was observed. The strength of the Lewis acid sites increased with the sulfate loadings. The catalytic activity of the sulfated TiO_2 increased with the sulfate content until the nominal SO_4^{2-}/TiO_2 ratio of 7.5 wt.%, and then it dropped gradually. A four-fold increase in production rate over the optimal sulfated TiO_2 catalyst was observed compared to that over the commercial P25 TiO_2 catalyst. The activation energy was 66 kJ/mol. A continuous process over the optimal sulfated TiO_2 was developed, however the production rate was much lower than the value obtained in the batch reactor due to the existence of large temperature gradient on the cross section of the conventionally heated continuous reactor. It was also found out that the deactivation kinetics accelerated at higher reaction temperatures. The direct amide synthesis from propionic and acetic acids with aniline showed higher production rates over the 7.5 wt.% SO_4^{2-} treated TiO_2 than the model reaction.

To apply the catalyst to RF-heated reactor, a series of composite magnetic catalysts (CMCs) were synthesized from nickel ferrite and sulfated TiO_2 by ball milling. This method is suitable for commercial production and the

synthesized CMCs have both good magnetism and catalytic activity. The surface area of CMCs increased while their specific absorption rate (SAR) dropped with the increase of sulfated TiO_2 loading in the CMC. The activity of the sulfated titania were constant in all the ball milled CMCs, indicating the catalytic activity was not affected by the ratio of $TiO_2/NiFe_2O_4$ weight fraction in CMCs. However, faster deactivation kinetics was observed for the CMCs containing higher $NiFe_2O_4$ content. Comparing two continuous reactors operated under the same residence time, it was found out that the measured production rate normalized by the weight of titania in the RF-heated reactor was higher than that in the conventionally heated reactor, verifying a better heat transfer rate under RF heating. The deactivation of ball milled CMC was mainly due to the coke formation and a slight sintering of the titania which merged the small pores into larger ones in spent CMCs. The catalytic activity was totally recovered by calcination process while the deactivation rate was increased after each regeneration step due to the irreversible change of the mean pore sizes.

Another type of CMC having core-shell structure was synthesized by the sol-gel method. The titania loading in the CMC was precisely controlled by adjusting the amount of titania precursor in the initial synthesis sol. No chemical reaction occurred between the magnetic core and catalytic titania shell below 500 °C. The optimisation of the calcination temperature demonstrated that the transition of amorphous titania into catalytically active anatase phase started at 450 °C, resulting in the best catalytic activity and higher SAR when calcined at 500 °C. The TiO_2 loading also influenced the physical properties of CMCs and their activity in the RF-heated reactor. The specific production rate normalized by the weight of titania was constant for the CMCs with the titania loading above 17 wt.%. The catalyst with a 9 wt.% titania loading showed the activity lower by 60% likely because of a significant contribution of electronic interaction between the magnetic core and the catalytic shell. The deactivation rate was slower in the RF-CR over the CMC having higher TiO_2 loading. Analogous to the ball milled CMCs, the deactivation of core-shell CMCs was also caused by the carbonization of the chemicals. The coke was fully removed by the calcination. However after the

calcination step, a large decrease of the surface area caused by the sintering was observed, resulting in the non-reversible loss of the catalytic activity. Another mild regeneration method was applied, which was treating spent CMC with a hydrogen peroxide solution at 90 °C. The initial catalytic activity was fully restored after this regeneration method.

To further improve the catalytic activity and chemical resistance of the CMCs, a series of core-shell- shell CMCs with a SiO_2 middle layer were synthesized to avoid the interaction between the magnetic core and TiO_2 shell. The obtained SiO_2 layer was proved to be amorphous and had nearly no catalytic activity in the direct amidation reaction. The resulted T4 CMC showed a better magnetic property compared to the T3 CMCs having the same TiO_2 content. Moreover, the production rate normalized by the surface area of the titania was higher than that over the T3 CMC, demonstrating the negative electronic interaction between $NiFe_2O_4$ and TiO_2 was diminished by the addition of the SiO_2 middle layer. The sulfation methods of core-shell and core-shell-shell CMCs were studied. In the first method, calcined CMCs were sulfated while as-synthesized CMCs were sulfated in the second method. The catalytic activity was promoted by both methods. Due to the reduced steps of calcination, the second method provided larger surface area and thus better catalytic activity. Also, the deactivation rate of sulfated CMCs decreased compared to other CMCs, which might be due to the change of the acid sites strength. The activity of CMCs was totally recovered by a novel in-situ regeneration method using a hydrogen peroxide solution. However the deactivation was observed to accelerate after each regeneration step.

The core-shell like structures can be verified from different aspects besides the TEM images. For the $NiFe_2O_4@TiO_2$ CMC, the CMC having 32 wt.% titania loading showed the similar pattern as pure TiO_2 while the CMCs having less titania loadings presented the peaks as similar as $NiFe_2O_4$ particles, indicating the $NiFe_2O_4$ cores were totally enclosed by the synthesized shell when titania loading reached to 32 wt.%. The existence of the shell also affected the specific production rate of CMCs having various titania loading. It was observed that the CMCs having the titania loading higher than 9 wt.% had four fold higher specific production rates than the

CMC with 9 wt.% titania. As there exists the negative interaction between $NiFe_2O_4$ and TiO_2, it indicates that even the titania loading was increased from 9 wt.%, the added titania did not have a direct contact with $NiFe_2O_4$ cores, resulting in a much improved catalytic activity. This phenomenon again verified the core-shell structure. On the aspect of the core-shell-shell structure, the activity of TiO_2 in $NiFe_2O_4@SiO_2@TiO_2$ was much higher than that in $NiFe_2O_4@TiO_2$, which also indicated that the existence of SiO_2 middle layer successfully separated $NiFe_2O_4$ and TiO_2 components. The advantage of double-shell structure could also be seen in the experiments of sulfation of the CMCs. After the sulfation of the calcined CMCs, the SAR of sulfated $NiFe_2O_4@SiO_2@TiO_2$ was even higher than the value of original CMC while the SAR decreased after sulfation of $NiFe_2O_4@TiO_2$. As the diluted sulfuric acid could still led to the leaching of the magnetic cores, this demonstrates that the core-shell-shell structure could gave a better protection to the magnetic cores than the core-shell structure, which represented the better chemical resistance.

As the problem of large temperature gradient existed in the developed RF-heated reactor with extended catalytic bed, a near isothermal RF-CR having both preheating and catalytic zone was developed to provide the uniform temperature in the whole reactor. The RF power supplied in each zone was adjusted by (i) the length of the preheating zone positioned inside the magnetic field and (ii) the electronic current in the induction coil. Two operation modes were studied in this RF-heated reactor. In the semi-automatically controlling operation, the current was adjusted by a PID controller. However the near isothermal state could only be reached in the RF-heated reactor with the catalytic bed below 10 mm. However, if both the current and the length of the preheating zone were controlled manually, the axial temperature gradient was limited to 3 °C in a 20 mm catalytic bed. This near isothermal operation was achieved in a wide range of temperatures from 120 to 160 °C and with the flow rates up to 2.4 mL/min, indicating the flexibility of the options of reaction condition. The kinetic study was performed over CMCs in the RF-heated reactor with a 20 mm catalytic bed. The external mass transfer was sufficient with the flow rate above 1.4

mL/min. The specific production rate normalized by the amount of TiO_2 in this isothermal RF-heated reactor was higher than that in the batch reactor, indicating the sufficient heat and mass transfer conditions in the RF-CR. The throughputs of 4,N-diphenylbutyramide as well as N-phenylpropionamide, N-phenylacetamide in the near isothermal RF-CR were all higher than the same reactions conducted in the batch mode. This can get to the conclusion that the developed method can be extended to a wide class of compounds which are relevant to the needs of modern industry. The limitation of the method is related to thermolabile substrates (such as chiral compounds) where much lower production rates are needed and the temperature should be reduced far below 150 ^{o}C. However the overall production rate can be kept similar by increasing the length of the reactor.

8.2 Recommendations

8.2.1 Modification of TiO_2

Even though sulfated TiO_2 was proved to have better catalytic activity than pure TiO_2 on direct amide synthesis, there is still possibility of enhancing the catalytic activity of TiO_2 by other functionalization methods like metal doping or attaching other ions on the surface. The effect of functionalization on the type, strength, amounts and distribution of the acid sites is also necessary to be further explored. It will give a full understanding of the mechanism and can be a guidance to synthesize the desired catalyst having the acids sites targeting for different organic reactions. Other novel heterogeneous catalysts such as ionogel [214] can also be tried and optimized for direct amide synthesis.

8.2.2 Optimization of core-shell-shell magnetic catalysts

The core-shell-shell CMC synthesized by sol-gel method has been proved to show the best performance in the RF-heated continuous reactor. Actually, parameters in sol-gel method can be easily optimized to synthesize the CMC with better characteristics. For instance, by changing the type or

concentration of the surfactants, CMC could have much larger surface area and thus better catalytic activity. The composition of the initial solution and the aging time can be further tuned to find the desired fraction of organic phase to modulate the reactivity of the precursors and to adjust preferential interactions at the organic/inorganic interface in subsequent self-assembly processes. The conditions during sol formation can be varied in order to obtain oligomers with desired degree of branching, e.g. by optimizing the rates of hydrolysis and polycondensation reactions. For the synthesis of sol-gel derived TiO_2, the precursors have to be partially hydrolyzed in a very controlled manner, such that subsequent polycondensation reactions yield a weakly branched polymeric metal oxide sol. A process can be transferred to a glove-box with controlled humidity to control the kinetics of sol-gel process. Also, the dispersity of the magnetic can be improved by modifying the procedure in sol-gel method. In this way, the obtained CMC can be synthesized into perfect independent spheres having clear three-layer structure, which have a better chemical resistance and lower aggregation extent.

8.2.3 Scaling up

The near isothermal RF-heated reactor developed has a great potential to be scaled up. For conventionally heated reactor, the reactor with larger volume always faced the problem of greater temperature gradient on the cross section when scaled up. As RF-heated reactor generates the heat from inside, under isothermal operation mentioned in section 7.2, the scaled up RF-heated reactor can still provide the uniform temperature on both parallel and cross section. On the aspect of equipment, high-frequency inductors are available in a large range of power and diameters. Small units in labs require a few kW with induction coils of a few centimetres in diameter. Inductors are however used industrially in large scale processes such as annealing, forging, graphitization in units which can use more than 1 MW power with coils of diameter larger than 1 meter. Depending on the scale of the amide production units, suitable RF generators can be readily available.

Since the RF-heated reactor is in the millimetre scale, it is also possible to use "numbering up principle" which is to use several identical microreactors to promote the productivity. Also, the current concentrations of reactants are limited by the solubility of products. To further increase the concentrations, the stream line can be warmed up to avoid crystallization or other solvents have higher solubility can be tried.

Reference

[1] T.K. Houlding, P. Gao, V. Degirmenci, K. Tchabanenko, E.V. Rebrov, Materials Science and Engineering: B, 193 (2015) 175-180.

[2] V.R. Pattabiraman, J.W. Bode, Nature, 480 (2011) 471-479.

[3] D.J. Constable, P.J. Dunn, J.D. Hayler, G.R. Humphrey, J.L. Leazer Jr, R.J. Linderman, K. Lorenz, J. Manley, B.A. Pearlman, A. Wells, Green Chemistry, 9 (2007) 411-420.

[4] E. Valeur, M. Bradley, Chemical Society Reviews, 38 (2009) 606-631.

[5] R. Singh, A. Godfrey, B. Gregertsen, F. Muller, K.V. Gernaey, R. Gani, J.M. Woodley, Computers & Chemical Engineering, 58 (2013) 344-368.

[6] S. Ceylan, L. Coutable, J. Wegner, A. Kirschning, Chemistry–A European Journal, 17 (2011) 1884-1893.

[7] C. Chen, S.H. Hong, Organic & biomolecular chemistry, 9 (2011) 20-26.

[8] O. Belafdal, M. Bergon, M. Calmon, J.P. Calmon, The Journal of Organic Chemistry, 54 (1989) 4193-4198.

[9] K. Arnold, B. Davies, R.L. Giles, C. Grosjean, G.E. Smith, A. Whiting, Advanced Synthesis & Catalysis, 348 (2006) 813-820.

[10] H. Charville, D. Jackson, G. Hodges, A. Whiting, Chemical Communications, 46 (2010) 1813-1823.

[11] H. Charville, D.A. Jackson, G. Hodges, A. Whiting, M.R. Wilson, European Journal of Organic Chemistry, 2011 (2011) 5981-5990.

[12] R.M. Lanigan, P. Starkov, T.D. Sheppard, The Journal of organic chemistry, 78 (2013) 4512-4523.

[13] R.S. Varma, K.P. Naicker, Tetrahedron letters, 40 (1999) 6177-6180.

[14] L. Perreux, A. Loupy, F. Volatron, Tetrahedron, 58 (2002) 2155-2162.

[15] T.K. Houlding, K. Tchabanenko, M.T. Rahman, E.V. Rebrov, Organic & biomolecular chemistry, 11 (2013) 4171-4177.

[16] H. Lundberg, F. Tinnis, H. Adolfsson, Chemistry-A European Journal, 18 (2012) 3822-3826.

[17] F. Tinnis, H. Lundberg, H. Adolfsson, Advanced Synthesis & Catalysis, 354 (2012) 2531-2536.

[18] R.M. Al‐Zoubi, O. Marion, D.G. Hall, Angewandte Chemie, 120 (2008) 2918-2921.

[19] D.J. Cole-Hamilton, Science, 299 (2003) 1702-1706.

[20] S.H. Siddiki, A.S. Touchy, M. Tamura, K.-i. Shimizu, RSC Advances, 4 (2014) 35803-35807.

[21] F. Arena, C. Deiana, A.F. Lombardo, P. Ivanchenko, Y. Sakhno, G. Trunfio, G. Martra, Catalysis Science & Technology, 5 (2015) 1911-1918.

[22] P.S. Chaudhari, S.D. Salim, R.V. Sawant, K.G. Akamanchi, Green Chemistry, 12 (2010) 1707-1710.

[23] K. Arnold, A.S. Batsanov, B. Davies, A. Whiting, Green Chemistry, 10 (2008) 124-134.

[24] J.W. Comerford, J.H. Clark, D.J. Macquarrie, S.W. Breeden, Chemical Communications, (2009) 2562-2564.

[25] M.A. Ali, S. Siddiki, W. Onodera, K. Kon, K.i. Shimizu, ChemCatChem, 7 (2015) 3555-3561.

[26] S. Nagarajan, P. Ran, P. Shanmugavelan, M. Sathishkumar, A. Ponnuswamy, K.S. Nahm, New Journal of Chemistry, 36 (2012) 1312-1319.

[27] G.C. Bond, (1987).

[28] Y.A. Chesalov, G.B. Chernobay, T.V. Andrushkevich, Journal of Molecular Catalysis A: Chemical, 373 (2013) 96-107.

[29] C. Deiana, Y. Sakhno, M. Fabbiani, M. Pazzi, M. Vincenti, G. Martra, ChemCatChem, 5 (2013) 2832-2834.

[30] M. Hosseini-Sarvari, E. Sodagar, Comptes Rendus Chimie, 16 (2013) 229-238.

[31] M. Hosseini-Sarvari, E. Safary, A. Jarrahpour, R. Heiran, Comptes Rendus Chimie, 15 (2012) 980-987.

[32] B. Krishnakumar, M. Swaminathan, Journal of Molecular Catalysis A: Chemical, 334 (2011) 98-102.

[33] S. Jothivel, R. Velmurugan, K. Selvam, B. Krishnakumar, M. Swaminathan, Separation and Purification Technology, 77 (2011) 245-250.

[34] X. Wang, C.Y. Jimmy, P. Liu, X. Wang, W. Su, X. Fu, Journal of Photochemistry and Photobiology A: Chemistry, 179 (2006) 339-347.

[35] A. Nakajima, A. Nakamura, N. Arimitsu, Y. Kameshima, K. Okada, Thin Solid Films, 516 (2008) 6392-6397.

[36] I. Ahmed, N.A. Khan, D.K. Mishra, J.S. Lee, J.-S. Hwang, S.H. Jhung, Chemical Engineering Science, 93 (2013) 91-95.

[37] R.M. de Almeida, L.K. Noda, N.S. Gonçalves, S.M. Meneghetti, M.R. Meneghetti, Applied Catalysis A: General, 347 (2008) 100-105.

[38] M. Hosseini-Sarvari, E. Sodagar, M.M. Doroodmand, The Journal of organic chemistry, 76 (2011) 2853-2859.

[39] K.J.A. Raj, B. Viswanathan, ACS applied materials & interfaces, 1 (2009) 2462-2469.

[40] C.-X. Tian, Y. Yang, H. Pu, Applied Surface Science, 257 (2011) 8391-8395.

[41] G.B. Chernobay, Y.A. Chesalov, V.P. Baltakhinov, G.Y. Popova, T.V. Andrushkevich, Catalysis Today, 164 (2011) 58-61.

[42] B. Krishnakumar, R. Velmurugan, S. Jothivel, M. Swaminathan, Catalysis Communications, 11 (2010) 997-1002.

[43] J. Ropero-Vega, A. Aldana-Pérez, R. Gómez, M. Niño-Gómez, Applied Catalysis A: General, 379 (2010) 24-29.

[44] G. Zenkovets, A. Volodin, A. Bedilo, E. Burgina, E. Al'kaeva, Kinetics and catalysis, 38 (1997) 669-672.

[45] B. Krishnakumar, R. Velmurugan, M. Swaminathan, Catalysis Communications, 12 (2011) 375-379.

[46] Y. Sakhno, (2014).

[47] M. Hosseini-Sarvari, S. Najafvand-Derikvandi, A. Jarrahpour, R. Heiran, Chemistry of Heterocyclic Compounds, 49 (2014) 1732-1739.

[48] Y. Wang, Y. Gan, R. Whiting, G. Lu, Journal of Solid State Chemistry, 182 (2009) 2530-2534.

[49] W. Shi, J. Li, Reaction Kinetics, Mechanisms and Catalysis, 111 (2014) 215-233.

[50] B. Krishnakumar, M. Swaminathan, Journal of Organometallic Chemistry, 695 (2010) 2572-2577.

[51] R.M. de Almeida, L.K. Noda, N.S. Gonçalves, S.M. Meneghetti, M.R. Meneghetti, Applied Catalysis A: General, 347 (2008) 100-105.

[52] B. Karmakar, A. Nayak, J. Banerji, Tetrahedron Letters, 53 (2012) 4343-4346.

[53] G. Bertotti, Hysteresis in magnetism: for physicists, materials scientists, and engineers, Academic press1998.

[54] P. Gao, X. Hua, V. Degirmenci, D. Rooney, M. Khraisheh, R. Pollard, R.M. Bowman, E.V. Rebrov, Journal of Magnetism and Magnetic Materials, 348 (2013) 44-50.

[55] X. Zhang, Y. Li, J.Q. Xiao, E. Wetzel, Journal of applied physics, 93 (2003) 7124-7126.

[56] X. Cui, M. Zhao, Q. Jiang, Thin Solid Films, 472 (2005) 328-333.

[57] A.H. Lu, E.e.L. Salabas, F. Schüth, Angewandte Chemie International Edition, 46 (2007) 1222-1244.

[58] S. Ceylan, C. Friese, C. Lammel, K. Mazac, A. Kirschning, Angewandte Chemie International Edition, 47 (2008) 8950-8953.

[59] A. El-Gendy, E. Ibrahim, V. Khavrus, Y. Krupskaya, S. Hampel, A. Leonhardt, B. Büchner, R. Klingeler, Carbon, 47 (2009) 2821-2828.

[60] S. Ziemniak, L.-L. Anovitz, R. Castelli, W.D. Porter, Journal of Physics and Chemistry of Solids, 4582 (2006).

[61] Y. Tan, Z. Zhuang, Q. Peng, Y. Li, Chemistry of Materials, 20 (2008) 5029-5034.

[62] Y. Ding, J.R. Morber, R.L. Snyder, Z.L. Wang, Advanced Functional Materials, 17 (2007) 1172-1178.

[63] I. Abu-Aljarayesh, A. Al-Bayrakdar, S. Mahmood, Journal of magnetism and magnetic materials, 123 (1993) 267-272.

[64] S. Rana, J. Rawat, R. Misra, Acta biomaterialia, 1 (2005) 691-703.

[65] I. Baker, Q. Zeng, W. Li, C.R. Sullivan, Journal of applied physics, 99 (2006) 08H106.

[66] M. Veverka, K. Závěta, O. Kaman, P. Veverka, K. Knížek, E. Pollert, M. Burian, P. Kašpar, Journal of Physics D: Applied Physics, 47 (2014) 065503.

[67] E.V. Rebrov, P. Gao, T.M. Verhoeven, J.C. Schouten, R. Kleismit, Z. Turgut, G. Kozlowski, Journal of Magnetism and Magnetic Materials, 323 (2011) 723-729.

[68] A. Faraz, A. Maqsood, Journal of superconductivity and novel magnetism, 25 (2012) 509-517.

[69] Z. Tang, C. Sorensen, K. Klabunde, G. Hadjipanayis, Physical review letters, 67 (1991) 3602.

[70] A. Franco, F. e Silva, Applied Physics Letters, 96 (2010) 2505.

[71] P. Pradhan, J. Giri, G. Samanta, H.D. Sarma, K.P. Mishra, J. Bellare, R. Banerjee, D. Bahadur, Journal of biomedical materials research Part B: Applied Biomaterials, 81 (2007) 12-22.

[72] I. Sharifi, H. Shokrollahi, S. Amiri, Journal of Magnetism and Magnetic Materials, 324 (2012) 903-915.

[73] P. Gao, X. Hua, V. Degirmenci, D. Rooney, M. Khraisheh, R. Pollard, R.M. Bowman, E.V. Rebrov, Journal of Magnetism and Magnetic Materials, 348 (2013) 44-50.

[74] S. Ziemniak, L. Anovitz, R. Castelli, W. Porter, Journal of Physics and Chemistry of Solids, 68 (2007) 10-21.

[75] X.-N. Zhao, H.-C. Hu, F.-J. Zhang, Z.-H. Zhang, Applied Catalysis A: General, 482 (2014) 258-265.

[76] E. Karaoğlu, A. Baykal, M. Şenel, H. Sözeri, M.S. Toprak, Materials Research Bulletin, 47 (2012) 2480-2486.

[77] A.K. Tucker‐Schwartz, R.L. Garrell, Chemistry‐A European Journal, 16 (2010) 12718-12726.

[78] J. Govan, Y.K. Gun'ko, Nanomaterials, 4 (2014) 222-241.

[79] P.H. Hoang, Chemical Engineering Journal, 262 (2015) 140-145.

[80] A.-J. Wang, Y.-F. Li, Z.-H. Li, J.-J. Feng, Y.-L. Sun, J.-R. Chen, Materials Science and Engineering: C, 32 (2012) 1640-1647.

[81] A. Ovenston, J. Walls, Chemical engineering research & design, 68 (1990) 530-536.

[82] S. Laurent, S. Dutz, U.O. Häfeli, M. Mahmoudi, Advances in colloid and interface science, 166 (2011) 8-23.

[83] R. Hergt, R. Hiergeist, I. Hilger, W. Kaiser, Y. Lapatnikov, S. Margel, U. Richter, Journal of Magnetism and Magnetic Materials, 270 (2004) 345-357.

[84] C. Alexiou, W. Arnold, R.J. Klein, F.G. Parak, P. Hulin, C. Bergemann, W. Erhardt, S. Wagenpfeil, A.S. Luebbe, Cancer research, 60 (2000) 6641-6648.

[85] Y. Tai, L. Wang, G. Yan, J.m. Gao, H. Yu, L. Zhang, Polymer International, 60 (2011) 976-994.

[86] A. Kirschning, L. Kupracz, J. Hartwig, Chemistry Letters, 41 (2012) 562-570.

[87] J. Hartwig, S. Ceylan, L. Kupracz, L. Coutable, A. Kirschning, Angewandte Chemie International Edition, 52 (2013) 9813-9817.

[88] J. Liu, S.Z. Qiao, Q.H. Hu, Small, 7 (2011) 425-443.

[89] P.S. Mueller, C.P. Parker, S.C. Larsen, Microporous and Mesoporous Materials, 204 (2015) 173-179.

[90] W. Pon-On, N. Charoenphandhu, I.-M. Tang, P. Jongwattanapisan, N. Krishnamra, R. Hoonsawat, Materials Chemistry and Physics, 131 (2011) 485-494.

[91] X. Li, J. Ding, X. Wang, K. Wei, J. Weng, J. Wang, Nanobiotechnology, IET, 8 (2014) 93-101.

[92] H. Sun, F. Ge, J. Zhao, Z. Cai, Materials Letters, 164 (2016) 152-155.

[93] H. Zheng, B. Zou, L. Chen, Y. Wang, X. Zhang, S. Zhou, CrystEngComm, 17 (2015) 6393-6398.

[94] H. Maleki, A. Simchi, M. Imani, B. Costa, Journal of Magnetism and Magnetic Materials, 324 (2012) 3997-4005.

[95] F. Neaţu, A. Kraynov, L. D'Souza, V.I. Pârvulescu, K. Kranjc, M. Kočevar, V. Kuncser, R. Richards, Applied Catalysis A: General, 346 (2008) 28-35.

[96] M. Ghader, M. Kassaee, Journal of the Iranian Chemical Society, 12 (2015) 979-985.

[97] N. Andhariya, B. Chudasama, R. Mehta, R. Upadhyay, Journal of Nanoparticle Research, 13 (2011) 3619-3631.

[98] S.-E. Kim, S.-W. Lee, Materials Research Bulletin, 47 (2012) 2969-2973.

[99] Q. Ding, L. Zhang, L. Yang, Materials Research Bulletin, 53 (2014) 205-210.

[100] F. Wang, J. Liu, X. Wang, J. Kong, S. Qiu, Ceramics International, 38 (2012) 6899-6902.

[101] M. Niyaifar, A. Hasanpour, H. Mohammadpour, J. Amighian, physica status solidi (a), 210 (2013) 1190-1194.

[102] H. Hamad, M.A. El-Latif, A.E.-H. Kashyout, W. Sadik, M. Feteha, New Journal of Chemistry, 39 (2015) 3116-3128.

[103] I. Jang, K.-E. You, Y.C. Kim, S.-G. Oh, Applied Surface Science, 316 (2014) 187-193.

[104] A. Wilson, S. Mishra, R. Gupta, K. Ghosh, Journal of Magnetism and Magnetic Materials, 324 (2012) 2597-2601.

[105] W. Yan, H. Fan, C. Yang, Materials Letters, 65 (2011) 1595-1597.

[106] J. Jaramillo, B.W. Boudouris, C.A. Barrero, F. Jaramillo, ACS applied materials & interfaces, 7 (2015) 25061-25068.

[107] Y. Yin, C. Liu, B. Wang, S. Yu, K. Chen, Dalton Transactions, 42 (2013) 7233-7240.

[108] Y. Wang, Z. Peng, W. Jiang, Journal of Materials Science: Materials in Electronics, 26 (2015) 4880-4887.

[109] B. Zhao, B. Fan, G. Shao, W. Zhao, R. Zhang, ACS applied materials & interfaces, 7 (2015) 18815-18823.

[110] W.-F. Ma, Y. Zhang, L.-L. Li, L.-J. You, P. Zhang, Y.-T. Zhang, J.-M. Li, M. Yu, J. Guo, H.-J. Lu, ACS nano, 6 (2012) 3179-3188.

[111] J. Liu, J. Cheng, R. Che, J. Xu, M. Liu, Z. Liu, The Journal of Physical Chemistry C, 117 (2012) 489-495.

[112] W. Wu, S. Zhang, F. Ren, X. Xiao, J. Zhou, C. Jiang, Nanoscale, 3 (2011) 4676-4684.

[113] H.-P. Peng, R.-P. Liang, J.-D. Qiu, Biosensors and Bioelectronics, 26 (2011) 3005-3011.

[114] H. Yang, D. Shi, S.-F. Ji, D.-N. Zhang, X.-F. Liu, Chinese Chemical Letters, 25 (2014) 1265-1270.

[115] E.-J. Kim, C.-S. Lee, Y.-Y. Chang, Y.-S. Chang, ACS applied materials & interfaces, 5 (2013) 9628-9634.

[116] J. An, L. Xu, J. He, D. Zhao, Z. Liu, Science China Physics, Mechanics and Astronomy, 56 (2013) 1508-1513.

[117] A. Ullrich, S. Hohenberger, A. Özden, S. Horn, Journal of Nanoparticle Research, 16 (2014) 1-10.
[118] W. Su, M. He, J. Xing, Y. Zhong, Z. Li, RSC Advances, 3 (2013) 25970-25975.
[119] L. Tong, J. Shi, D. Liu, Q. Li, X. Ren, H. Yang, The Journal of Physical Chemistry C, 116 (2012) 7153-7157.
[120] S. Bandyopadhyay, G. Singh, I. Sandvig, A. Sandvig, R. Mathieu, P.A. Kumar, W.R. Glomm, Applied Surface Science, 316 (2014) 171-178.
[121] A. Kumar, A. Singhal, Materials Chemistry and Physics, 131 (2011) 230-240.
[122] C. Okoli, M. Sanchez-Dominguez, M. Boutonnet, S. Järås, C. Civera, C. Solans, G.R. Kuttuva, Langmuir, 28 (2012) 8479-8485.
[123] L. Caruana, A. Costa, M. Cassani, E. Rampazzo, L. Prodi, N. Zaccheroni, Colloids and Surfaces A: Physicochemical and Engineering Aspects, 410 (2012) 111-118.
[124] C. Leostean, O. Pana, R. Turcu, M. Soran, S. Macavei, O. Chauvet, C. Payen, Journal of Nanoparticle Research, 13 (2011) 6181-6192.
[125] J. Rivas, Y.P. Redondo, E. Iglesias-Silva, J. Vilas-Vilela, L. León, M.A. López-Quintela, Journal of the Korean Physical Society, 62 (2013) 1376-1381.
[126] G. Bahmanrokh, M. Hashim, N. Soltani, I. Ismail, P. Vaziri, M. Navaseri, M. Erfani, S. Kanagesan, Materials Research Bulletin, 48 (2013) 4039-4047.
[127] J.G. Ovejero, C. Bran, E. Vilanova, J. Kosel, M.P. Morales, M. Vazquez, Journal of Magnetism and Magnetic Materials, 389 (2015) 144-147.
[128] I.T. Jeon, M.K. Cho, J.W. Cho, B.H. An, J.H. Wu, R. Kringel, D.S. Choi, Y.K. Kim, Journal of Materials Chemistry, 21 (2011) 12089-12095.
[129] D. Beydoun, R. Amal, G. Low, S. McEvoy, Journal of Molecular Catalysis A: Chemical, 180 (2002) 193-200.
[130] Q. Yuan, N. Li, W. Geng, Y. Chi, X. Li, Materials Research Bulletin, 47 (2012) 2396-2402.
[131] Y. Chi, Q. Yuan, Y. Li, L. Zhao, N. Li, X. Li, W. Yan, Journal of hazardous materials, 262 (2013) 404-411.
[132] A. Costa, B. Ballarin, A. Spegni, F. Casoli, D. Gardini, Journal of colloid and interface science, 388 (2012) 31-39.
[133] Y. Zhang, X. Yu, Y. Jia, Z. Jin, J. Liu, X. Huang, European Journal of Inorganic Chemistry, 2011 (2011) 5096-5104.
[134] N. Selvi, S. Sankar, K. Dinakaran, Journal of Materials Science: Materials in Electronics, 24 (2013) 4873-4880.
[135] V. Chawla, S. Prakash, B. Sidhu, Materials and Manufacturing processes, 22 (2007) 469-473.
[136] J. Benjamin, T. Volin, Metallurgical Transactions, 5 (1974) 1929-1934.
[137] C. Suryanarayana, Progress in materials science, 46 (2001) 1-184.
[138] K. Ralphs, C. Hardacre, S.L. James, Chemical Society Reviews, 42 (2013) 7701-7718.
[139] C.J. Jacobsen, J. Zhu, H. Lindeløv, J. Jiang, Journal of materials chemistry, 12 (2002) 3113-3116.
[140] Y.-R. Lee, M.-S. Jang, H.-Y. Cho, H.-J. Kwon, S. Kim, W.-S. Ahn, Chemical Engineering Journal, 271 (2015) 276-280.
[141] T.K. Houlding, E.V. Rebrov, Green Processing and Synthesis, 1 (2012) 19-31.
[142] N.G. Patil, E.V. Rebrov, K. Eranen, F. Benaskar, J. Meuldijk, J.-P. Mikkola, V. Hessel, L.A. Hulshof, D.Y. Murzin, J.C. Schouten, Journal of Microwave Power and Electromagnetic Energy, 46 (2012) 83-92.
[143] T.N. Glasnov, C.O. Kappe, Macromolecular rapid communications, 28 (2007) 395-410.
[144] J.D. Moseley, P. Lenden, M. Lockwood, K. Ruda, J.-P. Sherlock, A.D. Thomson, J.P. Gilday, Organic Process Research & Development, 12 (2007) 30-40.
[145] M.N. Pérez-Camacho, J. Abu-Dahrieh, D. Rooney, K. Sun, Catalysis Today, 242 (2015) 129-138.

[146] M. Beković, A. Hamler, Magnetics, IEEE Transactions on, 46 (2010) 552-555.

[147] M. Suto, Y. Hirota, H. Mamiya, A. Fujita, R. Kasuya, K. Tohji, B. Jeyadevan, Journal of Magnetism and Magnetic Materials, 321 (2009) 1493-1496.

[148] P. Kopčanský, N. Tomašovičová, M. Koneracká, V. Závišová, M. Timko, L. Tomčo, N. Éber, K. Fodor-Csorba, T. Tóth-Katona, A. Vajda, Physics Procedia, 9 (2010) 82-86.

[149] T.W.B. Riyadi, T. Zhang, D. Marchant, X. Zhu, Surface and Coatings Technology, 258 (2014) 154-159.

[150] D. Lupu, A. Biriş, A. Jianu, C. Bunescu, E. Burkel, E. Indrea, G. Mihăilescu, S. Pruneanu, L. Olenic, I. Mişan, Carbon, 42 (2004) 503-507.

[151] Z. Li, B. Zhao, P. Liu, B. Zhao, D. Chen, Y. Zhang, Physica E: Low-dimensional Systems and Nanostructures, 40 (2008) 452-456.

[152] L. Wang, Y. Peng, X. Hu, X. Xu, Ceramics International, 39 (2013) 6867-6875.

[153] W.M. Zhou, B. Yang, Z.X. Yang, F. Zhu, L.J. Yan, Y.F. Zhang, Applied surface science, 252 (2006) 5143-5148.

[154] J. Leclercq, F. Giraud, D. Bianchi, K. Fiaty, F. Gaillard, Applied Catalysis B: Environmental, 146 (2014) 131-137.

[155] K. Dilip, N.J. Vasa, K. Carsten, K. Ravindra, Applied Energy, 88 (2011) 938-946.

[156] S.R. Chaudhuri, J. Hartwig, L. Kupracz, T. Kodanek, J. Wegner, A. Kirschning, Advanced Synthesis & Catalysis, 356 (2014) 3530-3538.

[157] S. Mascia, P.L. Heider, H. Zhang, R. Lakerveld, B. Benyahia, P.I. Barton, R.D. Braatz, C.L. Cooney, J. Evans, T.F. Jamison, Angewandte Chemie International Edition, 52 (2013) 12359-12363.

[158] K.F. Jensen, Chemical Engineering Science, 56 (2001) 293-303.

[159] S.V. Ley, D.E. Fitzpatrick, R. Ingham, R.M. Myers, Angewandte Chemie International Edition, 54 (2015) 3449-3464.

[160] R. Porta, M. Benaglia, A. Puglisi, Organic Process Research & Development, (2015).

[161] V. Hessel, D. Kralisch, N. Kockmann, T. Noel, Q. Wang, ChemSusChem, 6 (2013) 746-789.

[162] T. Houlding, Application of radiofrequency heating in catalytic reaction engineering, Queen's University Belfast, 2014.

[163] S. Chatterjee, V. Degirmenci, F. Aiouache, E.V. Rebrov, Chemical Engineering Journal, 243 (2014) 225-233.

[164] X. Wang, H. Gu, Z. Yang, Journal of magnetism and magnetic materials, 293 (2005) 334-340.

[165] C. Morterra, G. Cerrato, F. Pinna, M. Signoretto, G. Strukul, Journal of Catalysis, 149 (1994) 181-188.

[166] R.A. Comelli, C.R. Vera, J.M. Parera, Journal of Catalysis, 151 (1995) 96-101.

[167] A.Y. Nosaka, J. Nishino, T. Fujiwara, T. Ikegami, H. Yagi, H. Akutsu, Y. Nosaka, The Journal of Physical Chemistry B, 110 (2006) 8380-8385.

[168] J.M. Pan, B. Maschhoff, U. Diebold, T. Madey, Journal of Vacuum Science & Technology A, 10 (1992) 2470-2476.

[169] A.P. Kulkarni, D.S. Muggli, Applied Catalysis A: General, 302 (2006) 274-282.

[170] Y. He, A. Tilocca, O. Dulub, A. Selloni, U. Diebold, Nature materials, 8 (2009) 585-589.

[171] Y. Niu, M. Xing, B. Tian, J. Zhang, Applied Catalysis B: Environmental, 115 (2012) 253-260.

[172] L.G. Devi, R. Kavitha, Materials Chemistry and Physics, 143 (2014) 1300-1308.

[173] P. Goswami, J.N. Ganguli, RSC Advances, 3 (2013) 8878-8888.

[174] J. Sun, K. Zhu, F. Gao, C. Wang, J. Liu, C.H. Peden, Y. Wang, Journal of the American Chemical Society, 133 (2011) 11096-11099.

[175] S. Yamazaki, K. Ichikawa, A. Saeki, T. Tanimura, K. Adachi, The Journal of Physical Chemistry A, 114 (2010) 5092-5098.

[176] A. Mantilla, F. Tzompantzi, G. Ferrat, A. López-Ortega, E. Romero, E. Ortiz-Islas, R. Gómez, M. Torres, Chemical communications, (2004) 1498-1499.

[177] C. Morterra, G. Cerrato, V. Bolis, Catalysis today, 17 (1993) 505-515.

[178] L. Matějová, K. Kočí, M. Reli, L. Čapek, V. Matějka, O. Šolcová, L. Obalová, Applied Surface Science, 285 (2013) 688-696.

[179] J. Lei, Y. Chen, F. Shen, L. Wang, Y. Liu, J. Zhang, Journal of Alloys and Compounds, (2015).

[180] M.M. Shirolkar, D. Phase, V. Sathe, J. Rodriguez-Carvajal, R.J. Choudhary, S.K. Kulkarni, Journal of Applied Physics, 109 (2011) 123512.

[181] Y. Wang, H. Wang, F. Yan, Surface and Interface Analysis, 41 (2009) 399-404.

[182] P. Sun, M. Zhu, R. Ma, K. Wang, J. Wei, D. Wu, T. Sasaki, H. Zhu, RSC Advances, 2 (2012) 10829-10835.

[183] L.J. Jallo, M. Schoenitz, E.L. Dreizin, R.N. Dave, C.E. Johnson, Powder technology, 204 (2010) 63-70.

[184] Y.W. Lim, J.-H. Kim, G. Seo, Korean Journal of Chemical Engineering, 30 (2013) 494-500.

[185] S. Pazokifard, S. Mirabedini, M. Esfandeh, M. Mohseni, Z. Ranjbar, Surface and interface analysis, 44 (2012) 41-47.

[186] F. Guo, Z.-G. Peng, J.-Y. Dai, Z.-L. Xiu, Fuel Processing Technology, 91 (2010) 322-328.

[187] A.B. Rajput, S.J. Rahaman, G. Sarkhel, M.K. Patra, S.R. Vadera, N.N. Ghosh, Polymer-Plastics Technology and Engineering, 52 (2013) 1097-1105.

[188] K. Priyanka, P. Sheena, N.A. Sabu, T. George, K. Balakrishna, T. Varghese, Indian Journal of Physics, 88 (2014) 657-663.

[189] G. Khade, M. Suwarnkar, N. Gavade, K. Garadkar, Journal of Materials Science: Materials in Electronics, 26 3309-3315.

[190] S. Bagheri, F. Chekin, S.B.A. Hamid, Russian Journal of Electrochemistry, 50 (2014) 947-952.

[191] K. Maaz, S. Karim, A. Mumtaz, S. Hasanain, J. Liu, J. Duan, Journal of Magnetism and Magnetic Materials, 321 (2009) 1838-1842.

[192] A. Paladino, Journal of the American Ceramic Society, 42 (1959) 168-175.

[193] X. Liang, R.L. Patel, Ceramics International, 40 (2014) 3097-3103.

[194] D.J. Kim, S.H. Hahn, S.H. Oh, E.J. Kim, Materials Letters, 57 (2002) 355-360.

[195] D.A. Hanaor, C.C. Sorrell, Journal of Materials science, 46 (2011) 855-874.

[196] H. Chen, K. Dai, T. Peng, H. Yang, D. Zhao, Materials chemistry and physics, 96 (2006) 176-181.

[197] S.-Y. Chen, L.-Y. Jang, S. Cheng, The Journal of Physical Chemistry B, 110 (2006) 11761-11771.

[198] C.H. Bartholomew, Applied Catalysis A: General, 212 (2001) 17-60.

[199] M. Kooti, A.N. Sedeh, Journal of Materials Science & Technology, 29 (2013) 34-38.

[200] P. Forzatti, L. Lietti, Catalysis today, 52 (1999) 165-181.

[201] C.A. Querini, Catalysis today, 62 (2000) 135-143.

[202] P. Qiu, W. Li, B. Thokchom, B. Park, M. Cui, D. Zhao, J. Khim, Journal of Materials Chemistry A, 3 (2015) 6492-6500.

[203] Y. Fan, C. Ma, W. Li, Y. Yin, Materials Science in Semiconductor Processing, 15 (2012) 582-585.

[204] Z. Peng, H. Tang, Y. Tang, K.F. Yao, H.H. Shao, International Journal of Photoenergy, 2014 (2014).

[205] R. Mohamed, M. Rashad, F. Haraz, W. Sigmund, Journal of Magnetism and Magnetic Materials, 322 (2010) 2058-2064.

[206] S. Janasi, M. Emura, F. Landgraf, D. Rodrigues, Journal of Magnetism and Magnetic Materials, 238 (2002) 168-172.

[207] K. Shih, T. White, J.O. Leckie, Environmental science & technology, 40 (2006) 5520-5526.

[208] J.A. Moulijn, A. Van Diepen, F. Kapteijn, Applied Catalysis A: General, 212 (2001) 3-16.

[209] J. Fernández, S. Chatterjee, V. Degirmenci, E.V. Rebrov, Green Processing and Synthesis, 4 (2015) 343-353.

[210] C. Perego, S. Peratello, Catalysis Today, 52 (1999) 133-145.

[211] R.-C. Lin, Periodic processes in chemical engineering, Rice University, 1966.

[212] M. Luther, J.J. Brandner, L. Kiwi-Minsker, A. Renken, K. Schubert, Chemical Engineering Science, 63 (2008) 4955-4961.

[213] S. Jensen, J.L. Olsen, S. Thorsteinsson, O. Hansen, U.J. Quaade, Catalysis Communications, 8 (2007) 1985-1990.

[214] Y.-M. Wang, V. Ulrich, G.F. Donnelly, F. Lorenzini, A.C. Marr, P.C. Marr, ACS Sustainable Chemistry & Engineering, 3 (2015) 792-796.

Appendices

Appendix A - PID controller
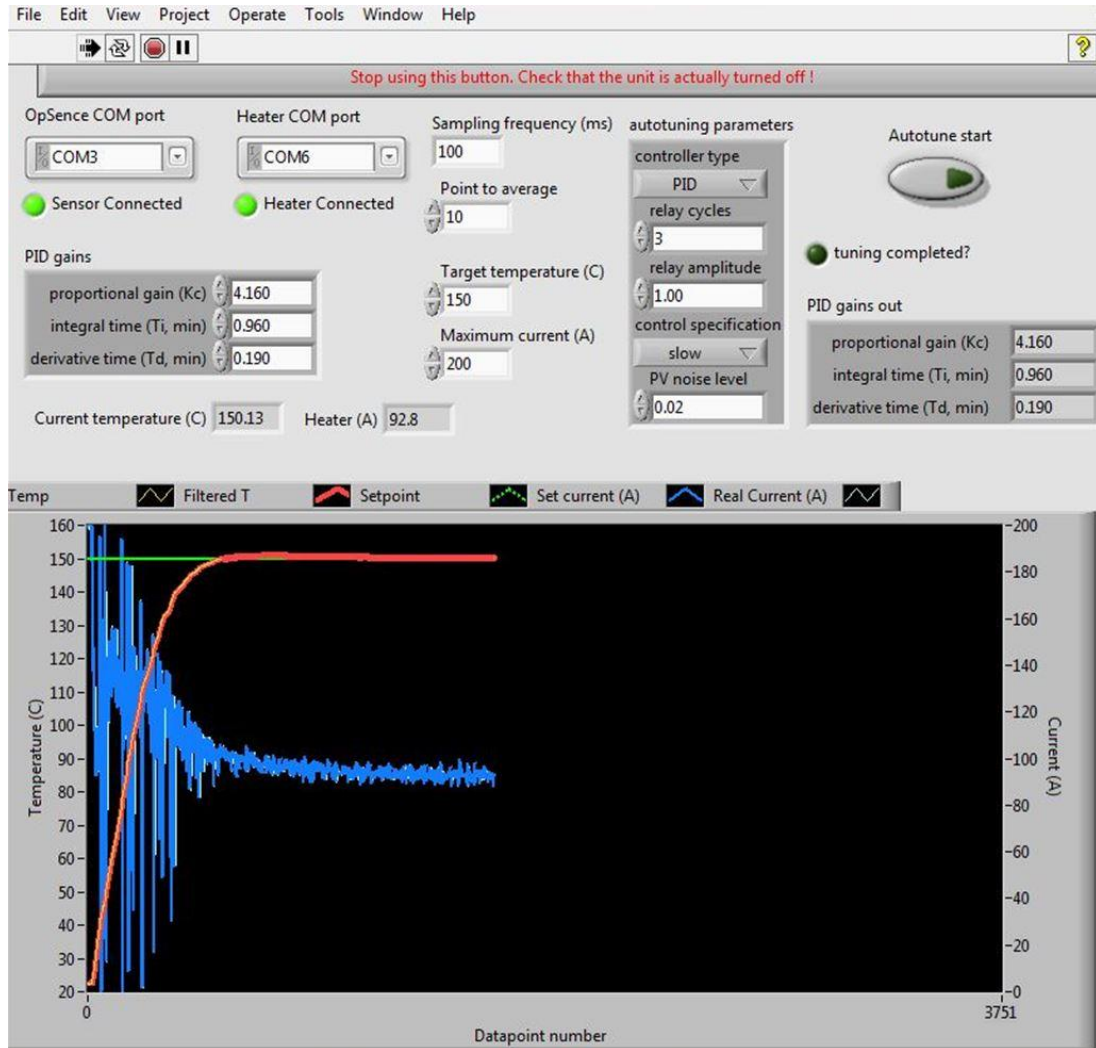
Figure A.1 The window of PID controller

The PID controller was developed by Dr Nikolay Cherkasov. The values of PID constants were determined by the trial and error during the initial usage. The reaction temperature was input in the column of "Target temperature" and the maximum current was adjusted in the column of "Maximum current". All other constants were kept at the same values in the course of using.

Appendix B - GC analysis

Appendix B.1- GC method for direct amidation from 4-phenylbutyric acid and aniline
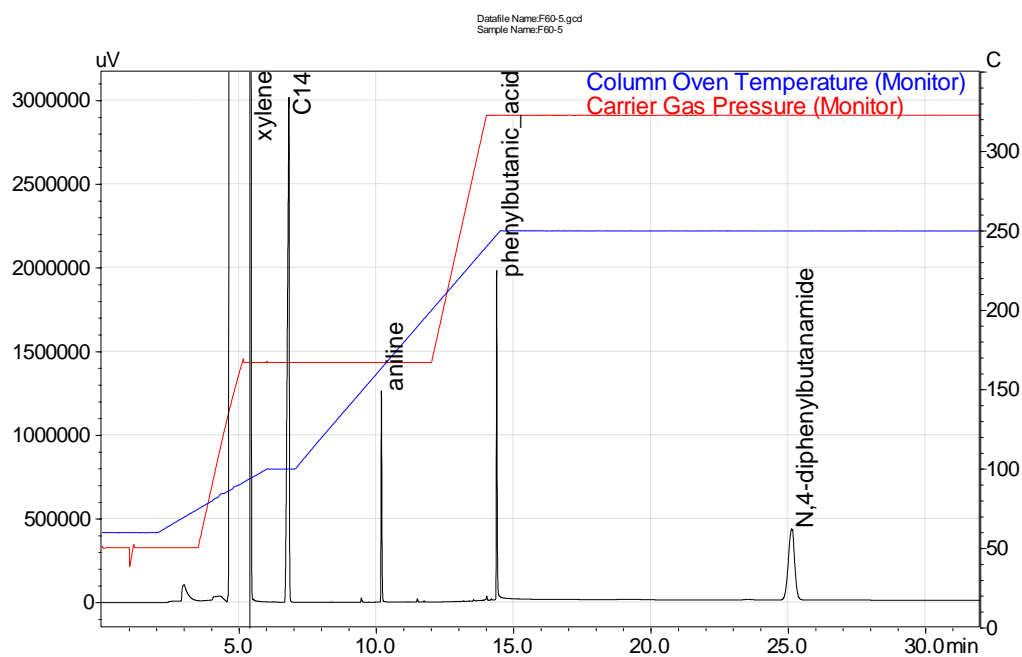
Figure B.1 Typical GC chromatogram for amidation between 4-phenylbutyric acid and aniline

Table B.1 GC Temperature program

Rate (°C/min)	Temperature (°C)	Hold time (min)
-	60.0	2.0
10.00	100.0	1.0
20.00	250.0	17.5
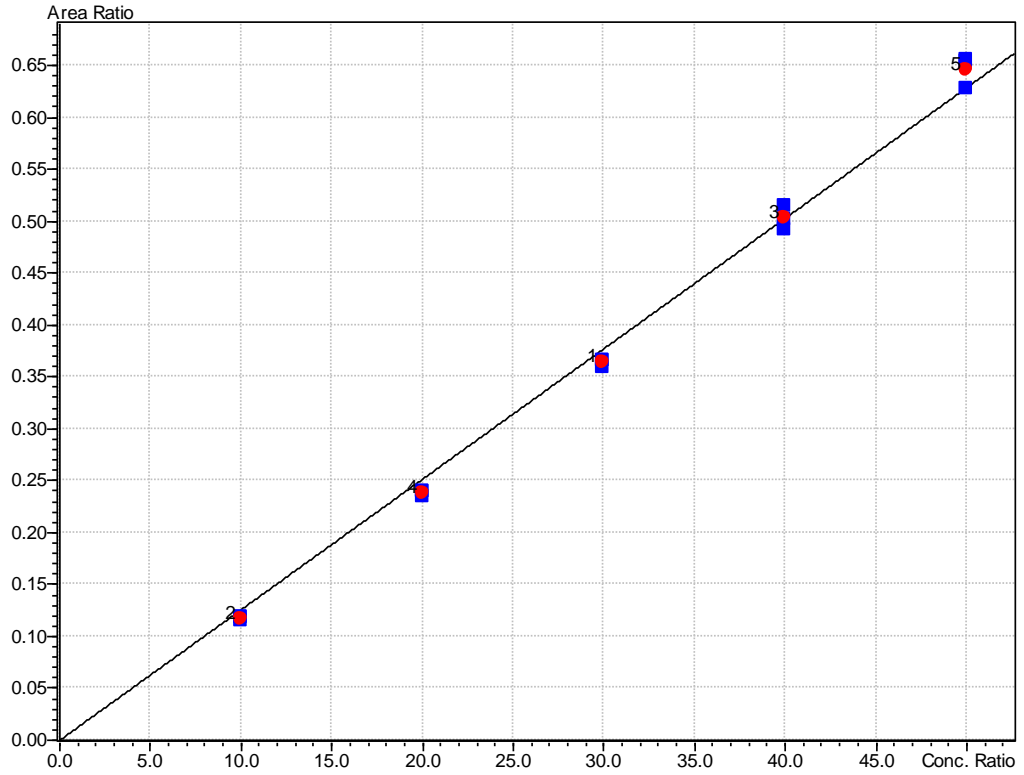
Figure B.2 GC calibration curve of 4-phenylbutyric acid
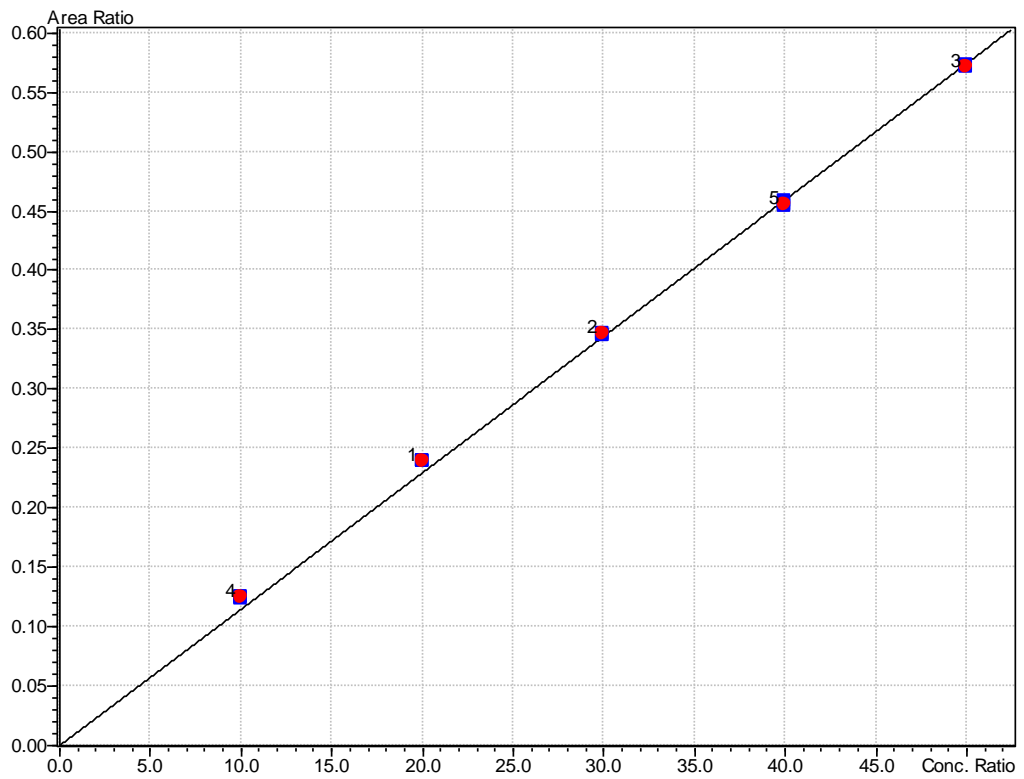
Figure B.3 GC calibration curve of aniline
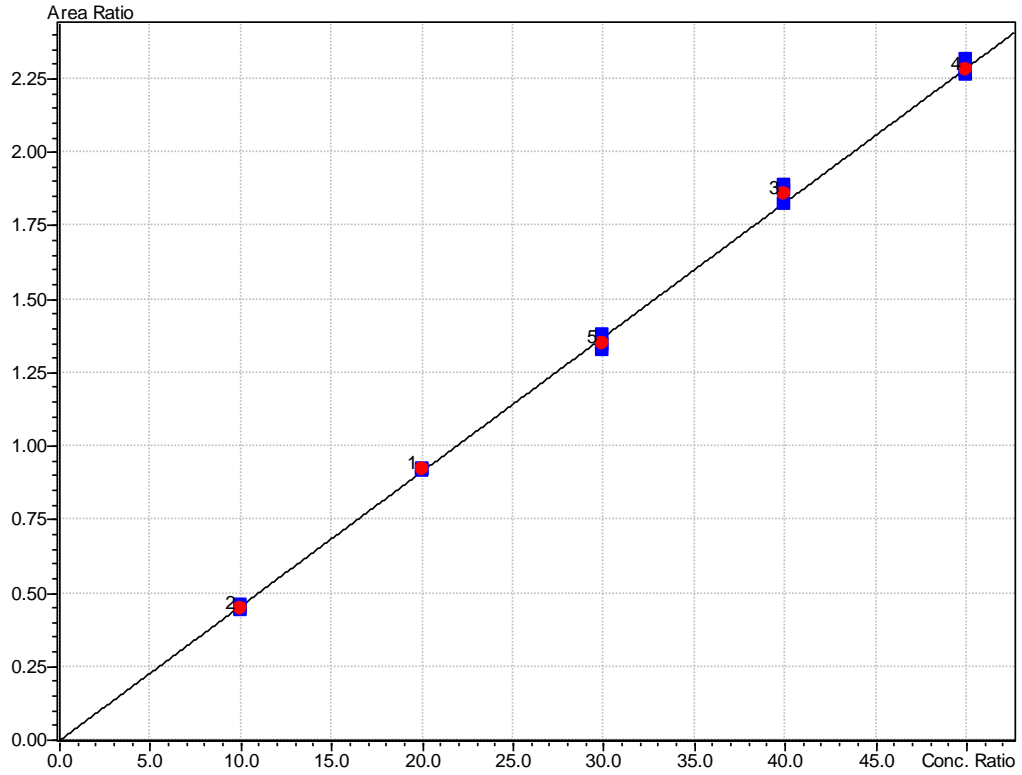
Figure B.4 GC calibration curve of 4, N-diphenylbutyramide

Appendix B.2- GC method for direct amidation between acetic acid and aniline
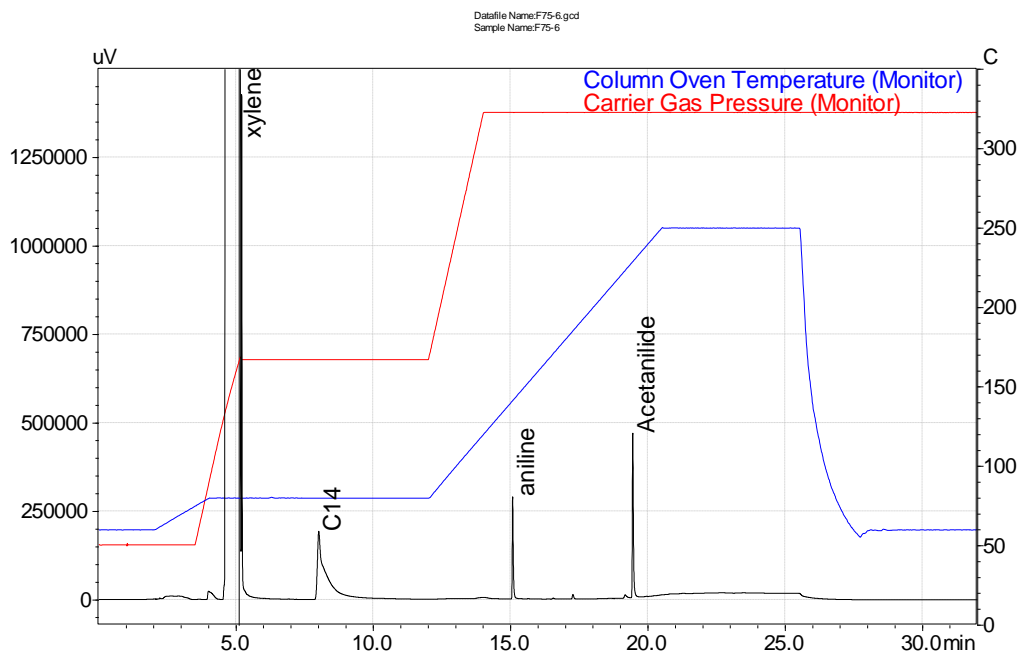
Figure B.5 Typical GC chromatogram for amidation between acetic acid and aniline

Table B.2 GC Temperature program

Rate (°C/min)	Temperature (°C)	Hold time (min)
-	60.0	2.0
10.00	80.0	8.0
20.00	250.0	5.00
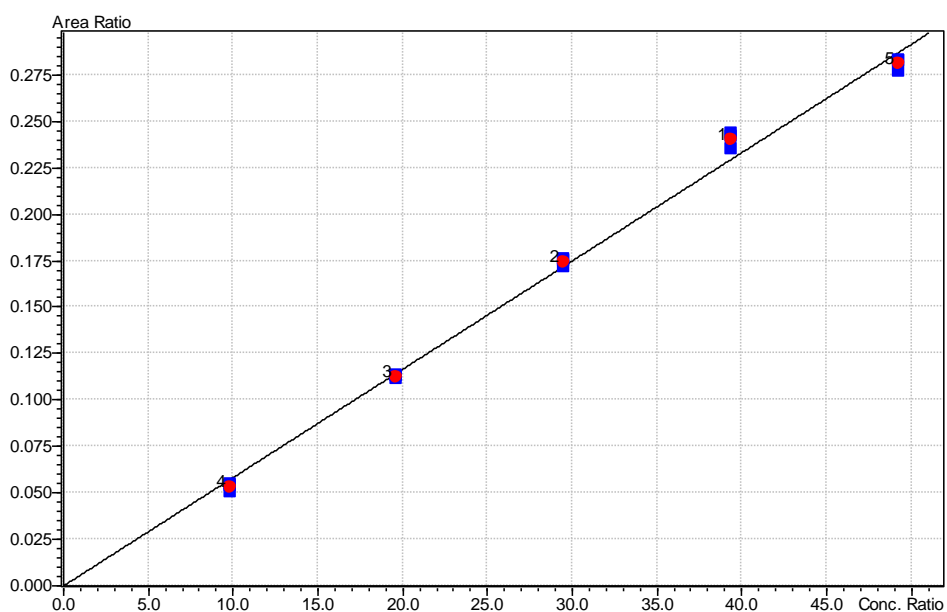
Figure B.6 GC calibration curve of aniline
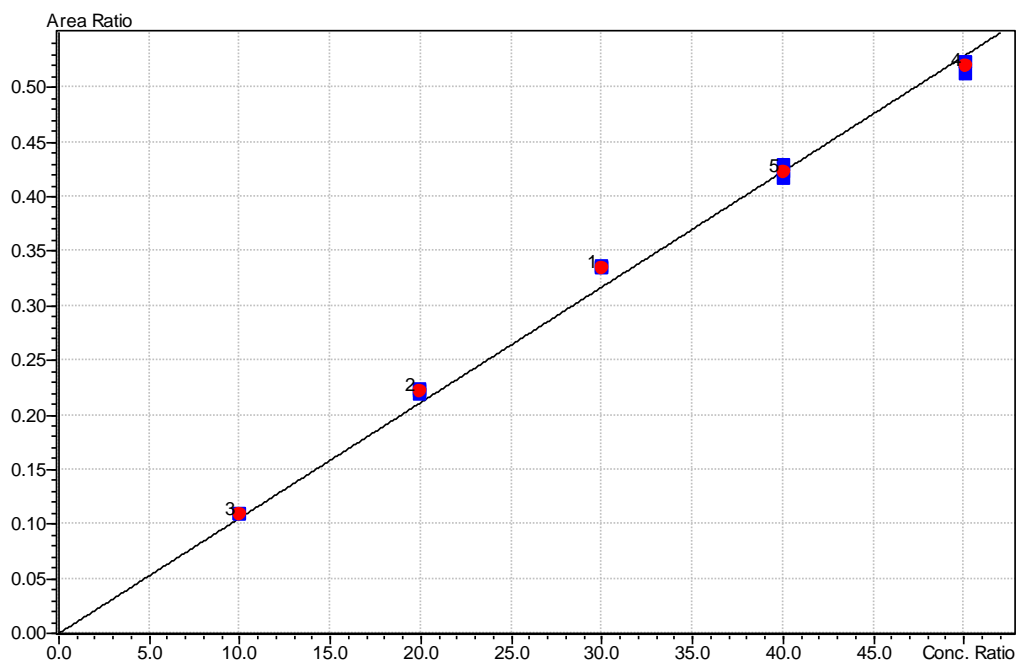
Figure B.7 GC calibration curve of acetanilide

Appendix B.3- GC method for direct amidation propionic acid and aniline
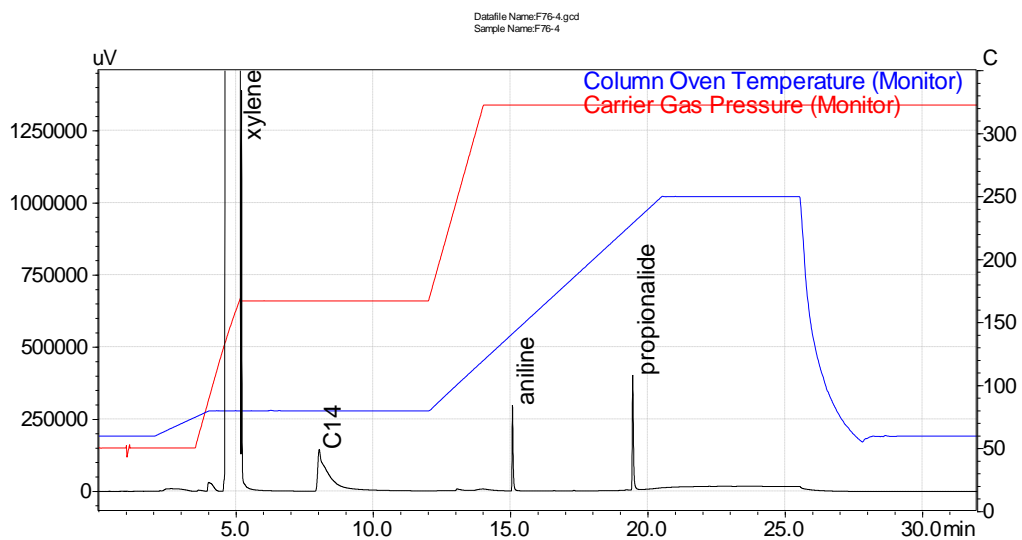
Figure B.8 Typical GC chromatogram for amidation between propionic acid and aniline

Table B.2 GC Temperature program

Rate (°C/min)	Temperature (°C)	Hold time (min)
-	60.0	2.00
10.00	80.0	8.00
20.00	250.0	5.00
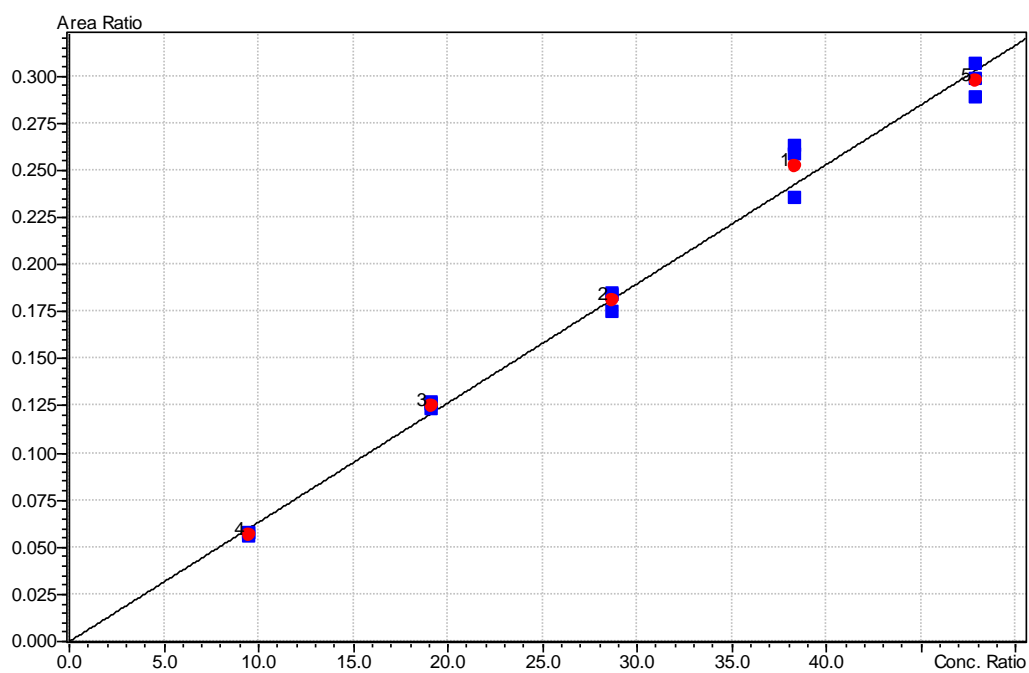
Figure B.9 GC calibration curve of aniline
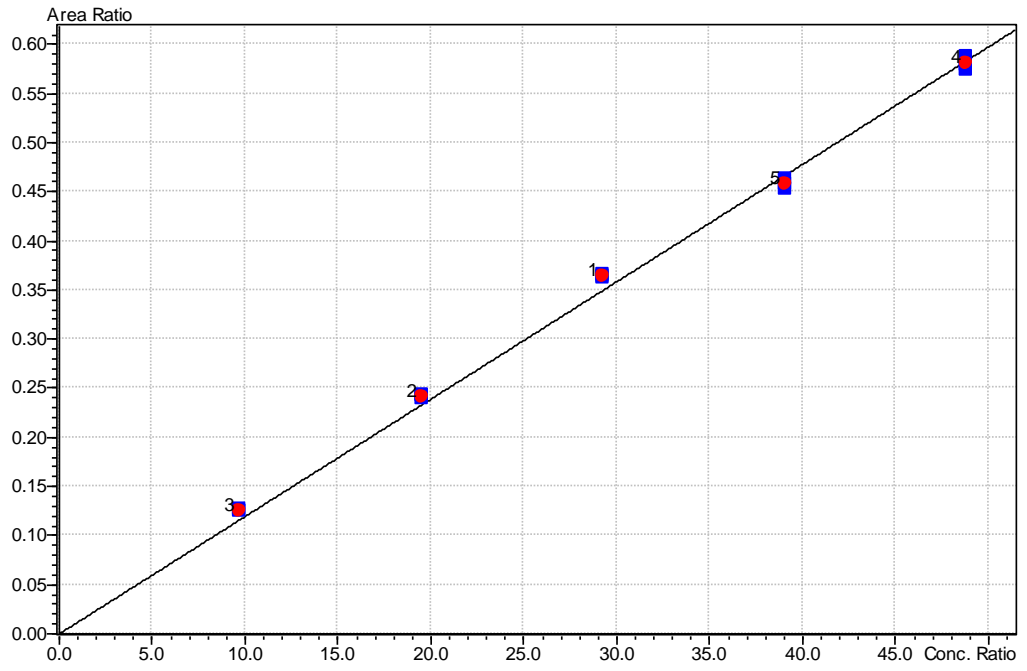
Figure B.10 GC calibration curve of propionalide

Appendix C – Concentration profiles in continuous reactors

The concentration profiles were simulated by Eq. (3.4) and the method stated in Section (3.3.2). Geometrical parameters of the flow rector are presented in the Table 7.2. The index of the kinetics parameters and corresponding reaction conditions in the continuous experiments are shown in Table C-1.

Table C-1. The index of the experiments and corresponding parameters

Figure code	Catalyst type	Heating method	Length of catalytic bed (mm)	Volumetric flow rate (μL/min)	Reaction temp. (°C)	Initial rate constant (L·mol^{-1}·s^{-1})
C-1	P25-7.5S	CH	10	228	130	0.18
C-2	P25-7.5S	CH	10	228	150	0.30
C-3	P25-7.5S	CH	10	228	170	0.43
C-4	T2-50	RF	10	142	150	0.34
C-5	T2-45	RF	11	142	150	0.30
C-6	T2-40	RF	12	142	150	0.28
C-7	T2-33	RF	14	142	150	0.22
C-8	T3-9-500	RF	5	40	150	0.006
C-9	T3-17-500	RF	5	40	150	0.04
C-10	T3-26-500	RF	5	40	150	0.059
C-11	T3-32-500	RF	5	40	150	0.15
C-12	T3-32-500	CH	5	40	150	0.065
C-13	WRT3-32-500	RF	5	40	150	0.059

Figure code	Catalyst type	Heating method	Length of catalytic bed (mm)	Volumetric flow rate (µL/min)	Reaction temp. (°C)	Initial rate constant (L·mol^{-1}·s^{-1})
C-14	TRT3-32-500	RF	5	40	150	0.13
C-15	T4-17-500	RF	5	40	150	0.074
C-16	NiFe$_2$O$_4$@SiO$_2$	RF	5	40	150	0.003
C-17	T3a-26-500-S	RF	5	40	150	0.14
C-18	T3b-25-500-S	RF	5	40	150	0.20
C-19	T4a-16-500-S	RF	5	40	150	0.12
C-20	T4b-14-500-S	RF	5	40	150	0.16
C-21	T2-50	RF	5	40	Oscillating from 140-160	0.094
C-22	T2-50	RF	5	40	150	0.36

The simulated concentration profiles are presented in the order of the corresponding section showing up in the main content. The initial concentrations of the reactants were kept at 0.05 mol/L in all the experiments conducted in the continuous experiments.
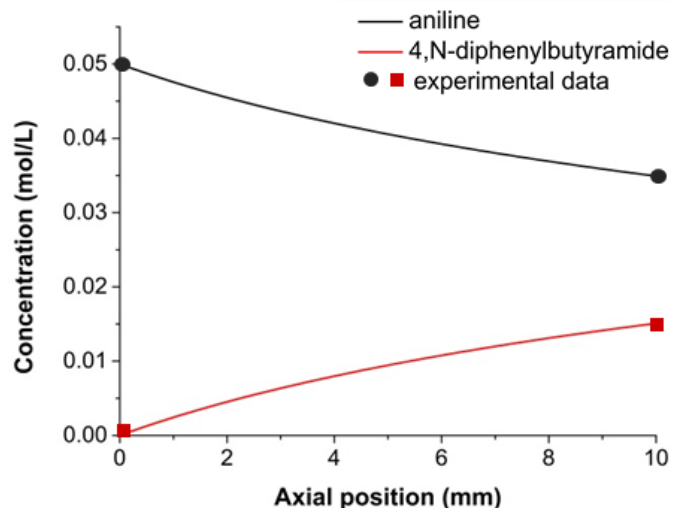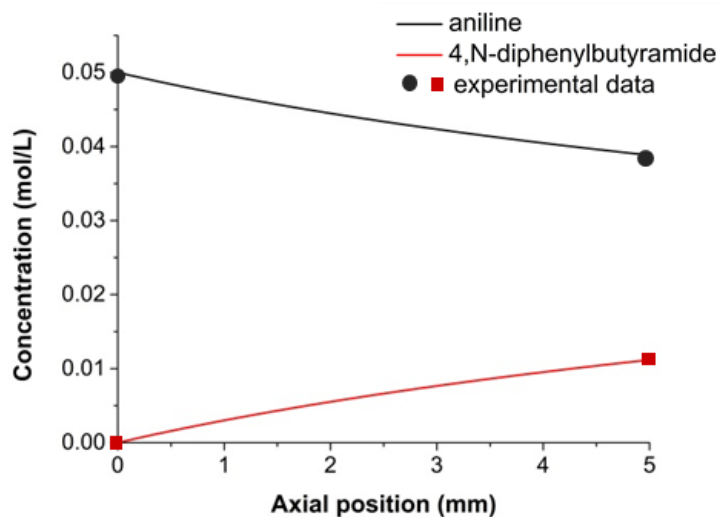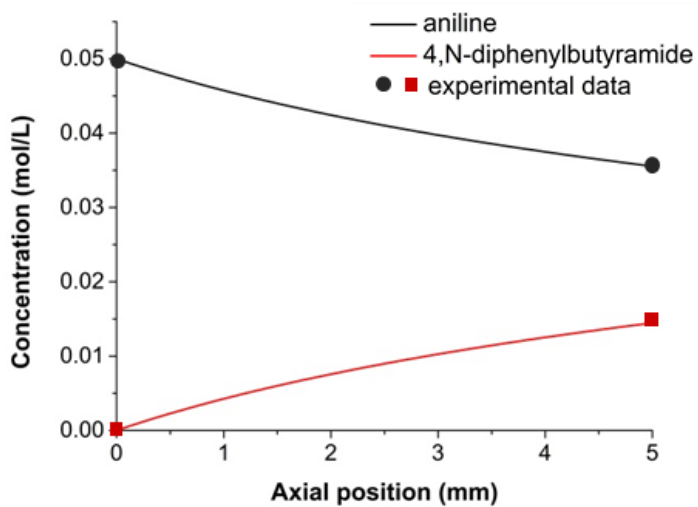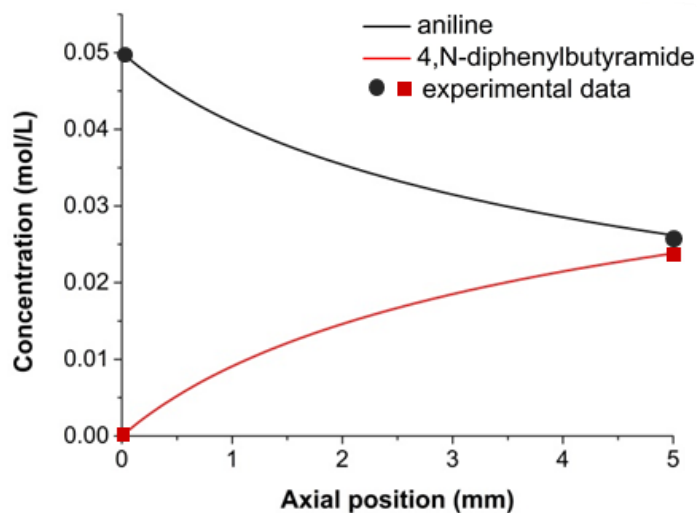
Figure C- 1 Concentration profiles along the axial position of the catalytic bed. Reaction conditions: 425 mg P25-7.5S catalyst (125-250 µm), 228 µL/min flow rate, 130 °C, 7 bars.
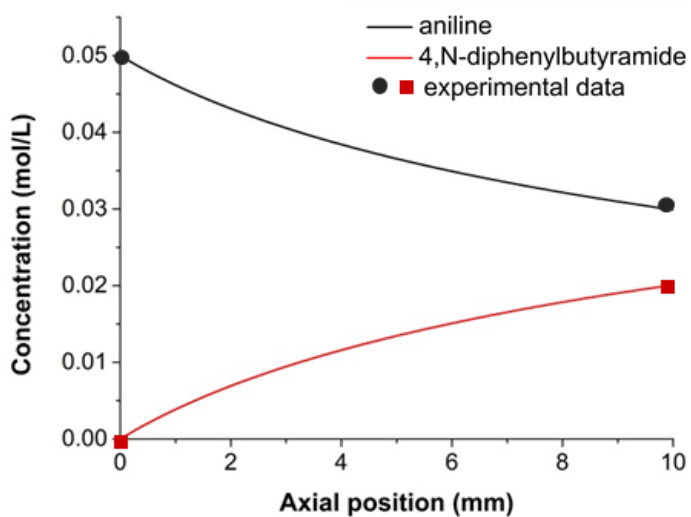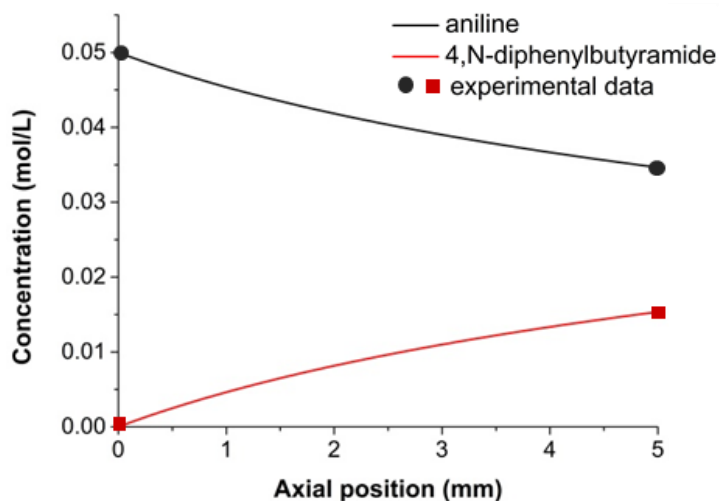

Figure C- 2 Concentration profiles along the axial position of the catalytic bed. Reaction conditions: 425 mg P25-7.5S catalyst (125-250 µm), 228 µL/min flow rate, 150 °C, 7 bars.
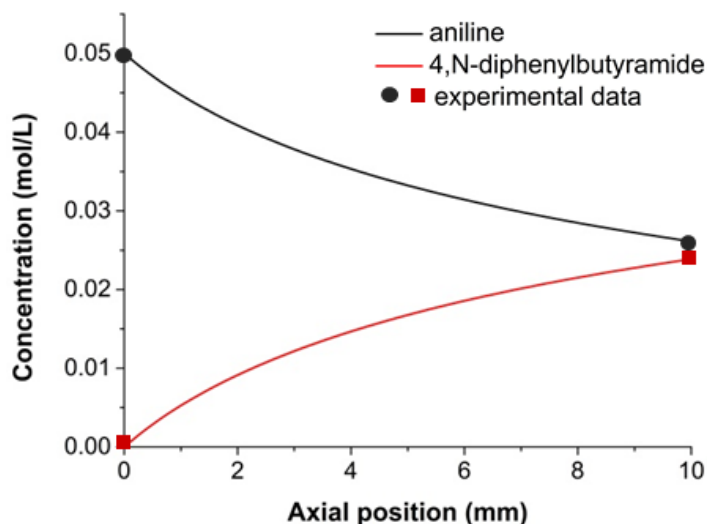
Figure C- 3 Concentration profiles along the axial position of the catalytic bed. Reaction conditions: 425 mg P25-7.5S catalyst (125-250 µm), 228 µL/min flow rate, 170 °C, 7 bars.
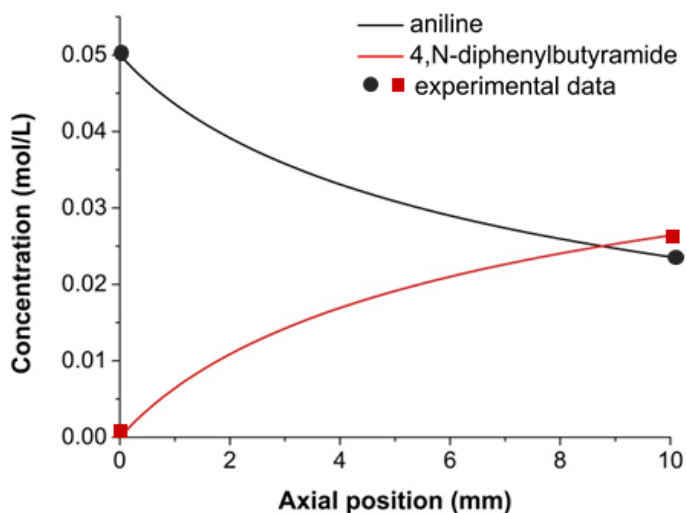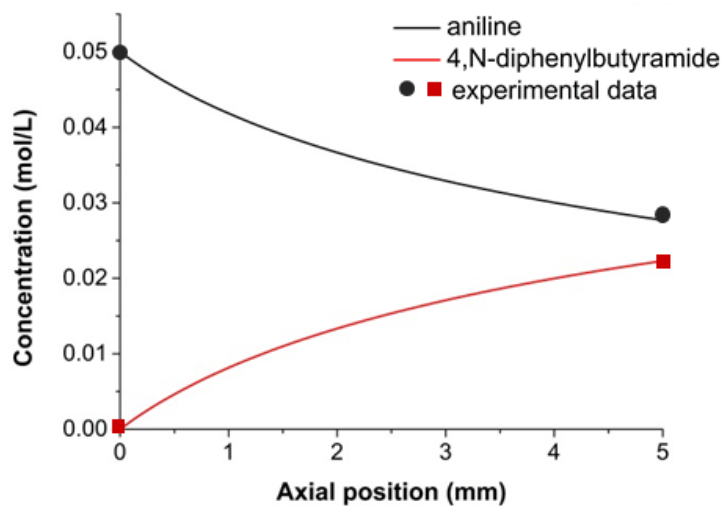

Figure C- 4 Concentration profiles along the axial position of the catalytic bed. Reaction conditions: 526 mg T2-50 catalyst (125-250 µm), 142 µL/min flow rate, 150 °C, 7 bars.
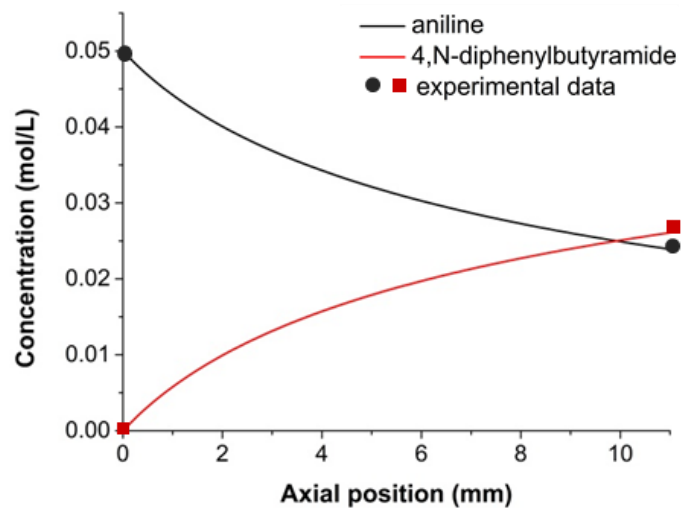
Figure C- 5 Concentration profiles along the axial position of the catalytic bed. Reaction conditions: 595 mg T2-45 catalyst (125-250 µm), 142 µL/min flow rate, 150 °C, 7 bars.
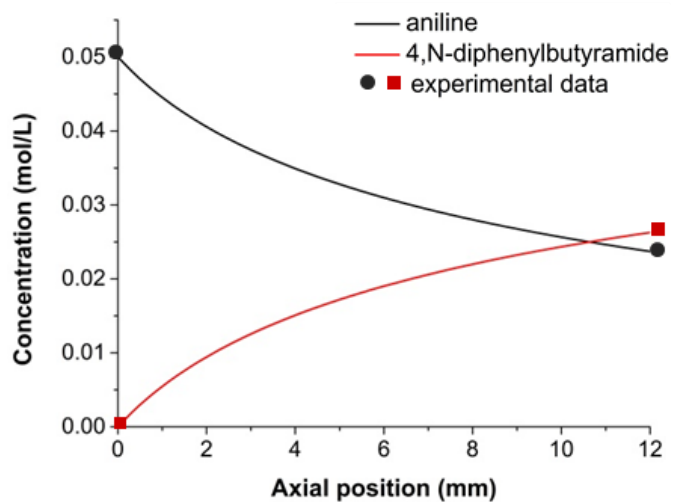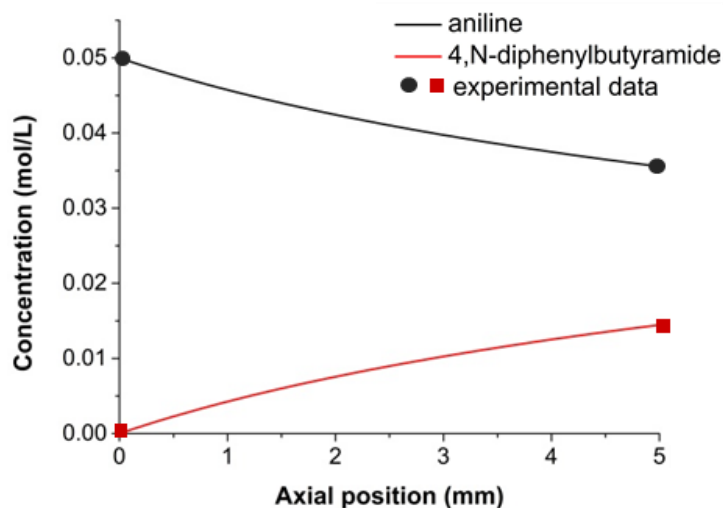

Figure C- 6 Concentration profiles along the axial position of the catalytic bed. Reaction conditions: 653 mg T2-40 catalyst (125-250 µm), 142 µL/min flow rate, 150 °C, 7 bars.
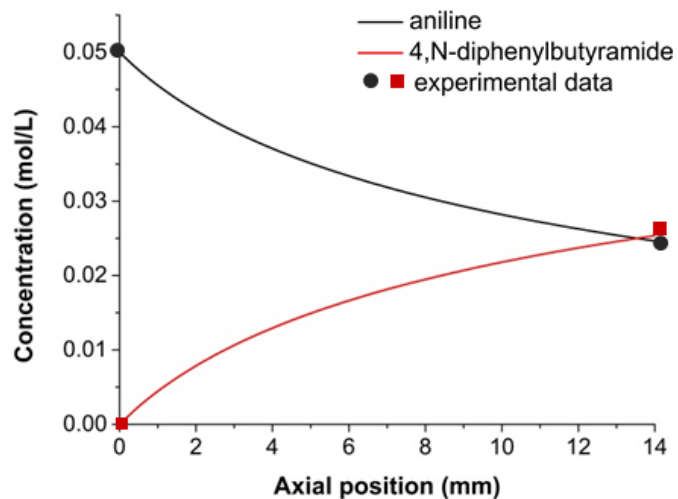
Figure C- 7 Concentration profiles along the axial position of the catalytic bed. Reaction conditions: 782 mg T2-33 catalyst (125-250 µm), 142 µL/min flow rate, 150 °C, 7 bars.
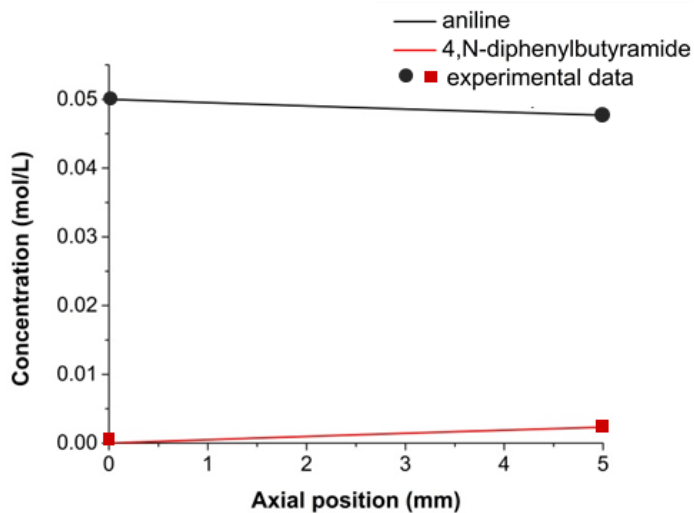
Figure C- 8 Concentration profiles along the axial position of the catalytic bed. Reaction conditions: 320 mg T3-9-500 catalyst (125-250 µm), 40 µL/min flow rate, 150 °C, 7 bars.
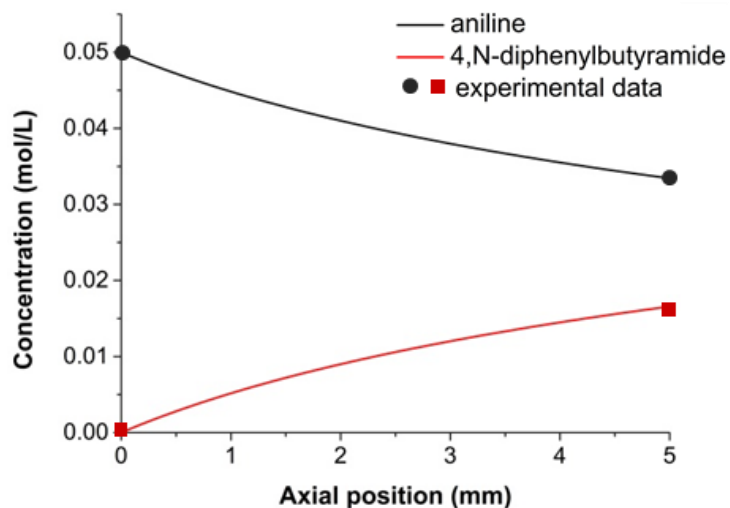
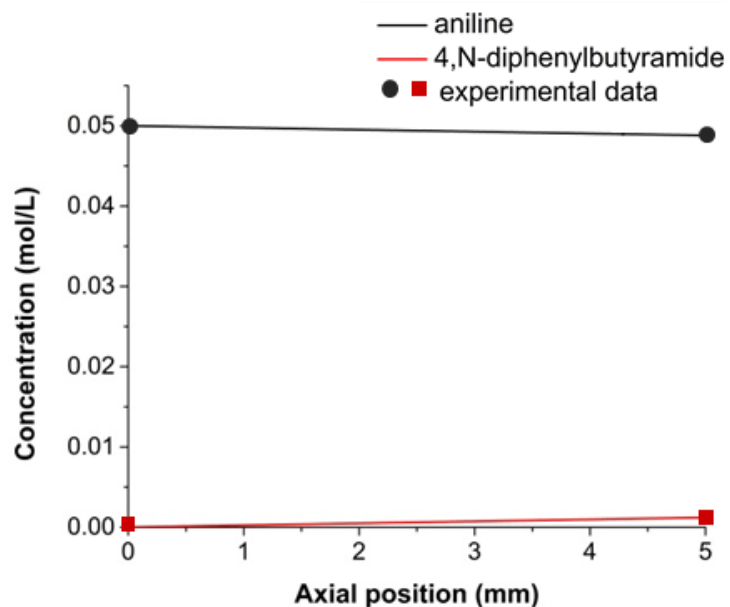Figure C- 9 Concentration profiles along the axial position of the catalytic bed. Reaction conditions: 320 mg T3-17-500 catalyst (125-250 μm), 40 μL/min flow rate, 150 °C, 7 bars.

Figure C- 10 Concentration profiles along the axial position of the catalytic bed. Reaction conditions: 320 mg T3-25-500 catalyst (125-250 μm), 40 μL/min flow rate, 150 °C, 7 bars.
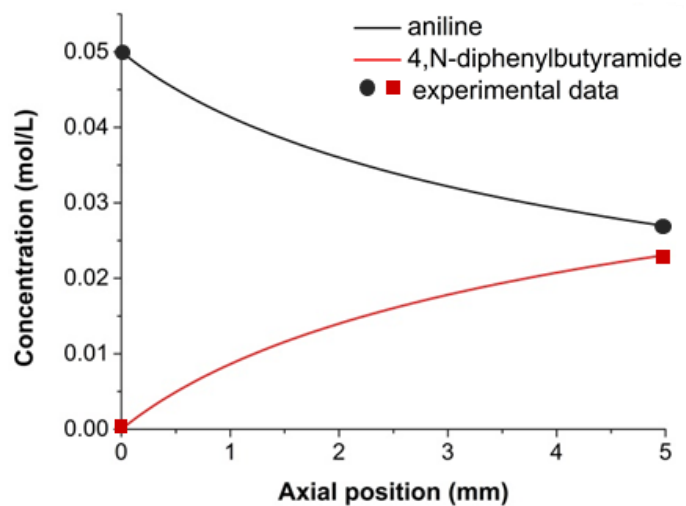
Figure C- 11 Concentration profiles along the axial position of the catalytic bed. Reaction conditions: 320 mg T3-32-500 catalyst (125-250 μm), 40 μL/min flow rate, 150 °C, 7 bars.

Figure C- 12 Concentration profiles along the axial position of the catalytic bed. Reaction conditions: 320 mg T3-32-500 catalyst (125-250 μm), 40 μL/min flow rate, 150 °C (conventional heating), 7 bars.

Figure C- 13 Concentration profiles along the axial position of the catalytic bed. Reaction conditions: 320 mg WRT3-32-500 catalyst (125-250 µm), 40 µL/min flow rate, 150 °C, 7 bars.
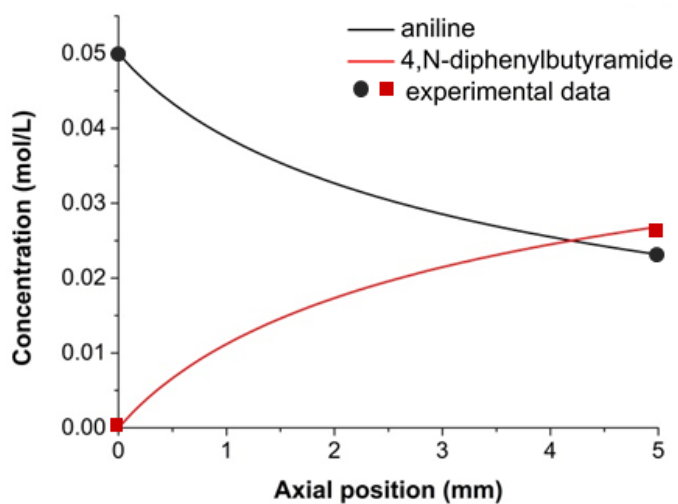

Figure C- 14 Concentration profiles along the axial position of the catalytic bed. Reaction conditions: 320 mg TRT3-32-500 catalyst (125-250 µm), 40 µL/min flow rate, 150 °C, 7 bars.
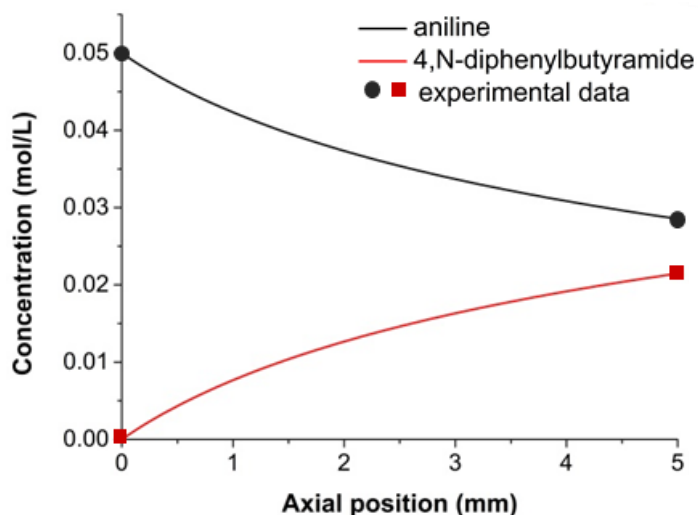
Figure C- 15 Concentration profiles along the axial position of the catalytic bed. Reaction conditions: 320 mg T4-17-500 catalyst (125-250 µm), 40 µL/min flow rate, 150 °C, 7 bars.

Figure C- 16 Concentration profiles along the axial position of the catalytic bed. Reaction conditions: 320 mg $NiFe_2O_4@SiO_2$ material (125-250 µm), 40 µL/min flow rate, 150 °C, 7 bars.

Figure C- 17 Concentration profiles along the axial position of the catalytic bed. Reaction conditions: 320 mg T3a-26-500-S catalyst (125-250 µm), 40 µL/min flow rate, 150 °C, 7 bars.

Figure C- 18 Concentration profiles along the axial position of the catalytic bed. Reaction conditions: 320 mg T3b-25-500-S catalyst (125-250 µm), 40 µL/min flow rate, 150 °C, 7 bars.

Figure C- 19 Concentration profiles along the axial position of the catalytic bed. Reaction conditions: 320 mg T4a-16-500-S catalyst (125-250 µm), 40 µL/min flow rate, 150 °C, 7 bars.
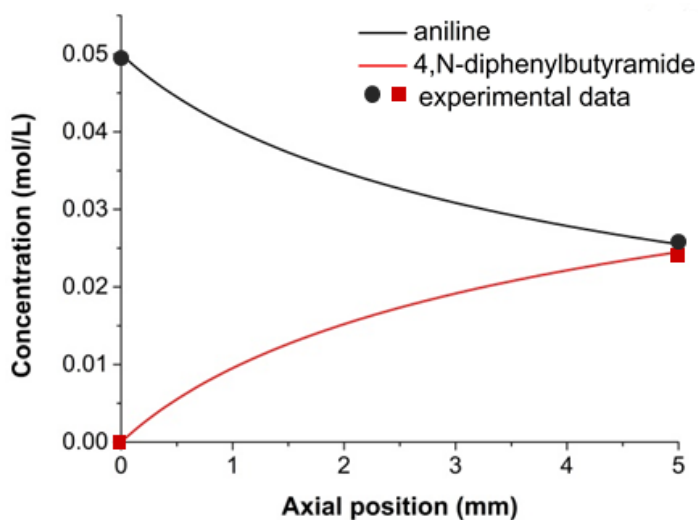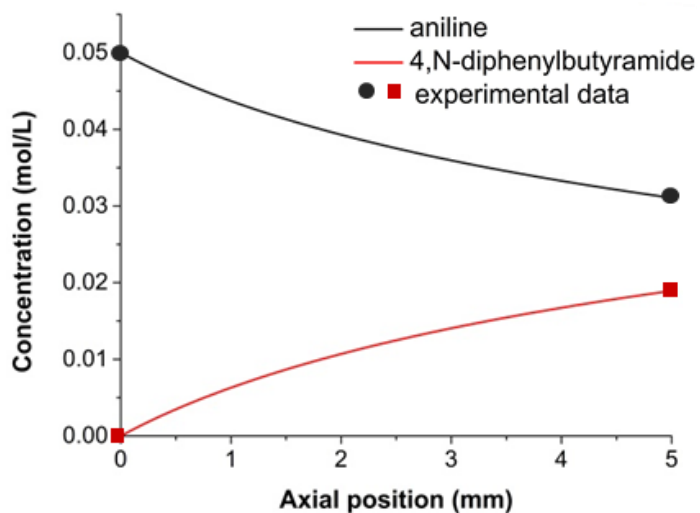

Figure C- 20 Concentration profiles along the axial position of the catalytic bed. Reaction conditions: 320 mg T4b-14-500-S catalyst (125-250 µm), 40 µL/min flow rate, 150 °C, 7 bars.
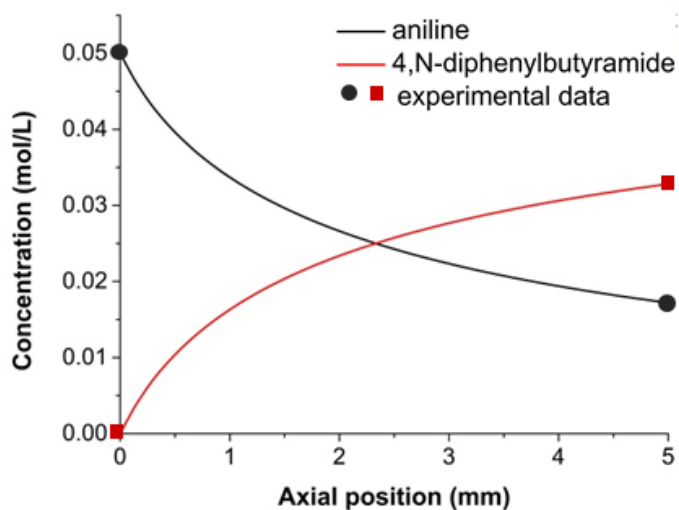
Figure C- 21 Concentration profiles along the axial position of the catalytic bed. Reaction conditions: 320 mg T2-50 catalyst (125-250 µm), 40 µL/min flow rate, oscillated temperature ranging in140-160 °C, 7 bars.

Figure C- 22 Concentration profiles along the axial position of the catalytic bed. Reaction conditions: 320 mg T2-50 catalyst (125-250 µm), 40 µL/min flow rate, 150 °C, 7 bars.